Electric Lift Augmentation of Scientific Balloons Using Gossamer Blades

by

Nicholas I. Kenny

B.S., University of Colorado Boulder, 2020

M.S., University of Colorado Boulder, 2021

A thesis submitted to the
Faculty of the Graduate School of the
University of Colorado in partial fulfillment
of the requirements for the degree of
Doctor of Philosophy
Department of Aerospace Engineering Sciences
2023

Committee Members:
Dale Lawrence, Chair
Prof. Brian Argrow
Prof. John Farnsworth
Prof. Zachary Sunberg
Prof. Aroh Barjatya

Kenny, Nicholas I. (PhD Candidate, Aerospace Engineering Sciences)

Electric Lift Augmentation of Scientific Balloons Using Gossamer Blades

Thesis directed by Prof. Dale Lawrence

Balloons have been used for studying the atmosphere for centuries, offering the unique benefit of enabling low cost observations in regions of the atmosphere that are otherwise difficult to access. Nonetheless, long-duration ballooning can still be prohibitively expensive, particularly for campaigns aiming to conduct routine flights across the globe. The application of gossamer propeller blades, made of string and fabric-like material and tensioned through centripetal forces, opens the door for inexpensive, long duration, targeted observations with hand-launched weather balloons, but also remains scalable to balloons of other sizes.

After achieving static stability of a gossamer blade in atmospheric conditions through a unique rigging method called the 4-bar link, manipulation of the blade geometry via string length adjustments can induce billow in the blades, producing lift by increasing their angle of attack and camber. This augments the lift of the balloon system aerodynamically rather than via changes in buoyancy. Scaled testing has been conducted verifying the stability of the 4-bar link and collecting preliminary lift and drag data from the gossamer blade using optical methods without direct force measurement.

Results from the scaled experiments have been applied to models exploring the design of a full scale lift augmentation system and the impacts such a system could have on various types of balloon missions. The 4-bar link enables stability in a gossamer structure without any traditional stiffening methods and establishes a baseline for future work on gossamer propellers and flexible wing structures.

Acknowledgements

My advisor, Dr. Dale Lawrence, has been instrumental in supporting me throughout my research, always providing thoughtful and insightful discussions and pushing me forward to better understand the problems at hand. Additionally, along with Dr. Brian Argrow, he has helped support my research financially through various research grants from the Air Force Office of Scientific Research.

Contents

Chapter

Appendix

List of Tables

Table

List of Figures

Figure

Chapter 1

Introduction

1.1 History of Ballooning

One of the oldest forms of crewed flight, balloons have been lifting off since at least the early 1700s. Deriving their lift initially from hot air, the work of Henry Cavendish and subsequent application by Jacques Charles, Anne-Jean Robert, and Nicolas-Louis Robert led to the first flight of a hydrogen-filled balloon in 1783 [22]. The first crewed flight of a hydrogen-filled balloon would follow later that year.

While crewed ballooning is still popular today, the use of lighter-than-air lifting gasses in crewed flight is rare. Even with the advent of satellites, balloons remain a popular tool for reconnaissance and signals intelligence operations by various governments worldwide, with an alleged Chinese reconnaissance balloon captivating American media outlets in early 2023 [24],[53]. Balloons are also frequently used for scientific endeavors, with one of the most notable continued uses of scientific ballooning being that of the National Weather Service, which began launching consistently in 1930. Now with up to four launches a day from 92 stations around the United States, these balloons fitted with radiosondes help inform weather predictions [88], reaching altitudes of up to 30 km.

With such frequent launches, these balloons need to be kept as inexpensive as possible, carrying only the balloon itself, a small parachute, and the required scientific and communications instruments as a payload. While this enables the high cadence of balloon launches, it also means that targeted observations of specific altitudes or regions of interest is impossible. The launch frequency also means that data is only telemetered on ascent, allowing back to back balloon launches on the same radio frequency at the expense of atmospheric data. This also rules out the possibility of flying other payloads that may require specific flight profiles or data on descent, such as the HYFLITS payloads that require a slow but controlled descent to measure atmospheric turbulence outside of the balloon wake [74]. For these kinds of missions, balloons with some form of control are required.

1.2 Historical Ballooning Missions

Many kinds of missions have either been conducted or proposed to be fulfilled by scientific balloons. While often smaller balloons are used for scientific measurements (such as the National Weather Services radiosonde program), balloons can also be used as tools to release other scientific payloads in conditions that would otherwise be unachievable. Finally, while often many other factors must be taken into consideration, balloons are not limited to simply operation on Earth. Numerous missions and studies of balloons on other planets and celestial bodies have been conducted.

1.2.1 Direct Balloon Measurements

With a renewed interest in hypersonic vehicles, numerous programs designed to study the upper atmosphere have been conducted, many taking advantage of the low cost and low operational burden of small scientific balloons to do so. Two such programs include HYFLITS, Hypersonic Flight In the Turbulent Stratosphere [74], [52], and LITOS, Leibniz-Institute Turbulence Observations in the Stratosphere [86]. While differing methods for measurement are used, both of these missions sought to measure turbulence in the lower Stratosphere at resolutions below a handful of meters, which is currently only achievable with in-situ techniques.

Particulate and aerosol measurements are also of renewed interest given their links to climate science. While ground and space-based LIDAR measurements are occasionally used, in addition to other space-based methods like solar and celestial occultation, balloons remain the primary method of gathering in-situ data in the upper Troposhphere and Stratosphere [45]. Missions such as ChArMEx, the Chemistry–Aerosol Mediterranean Experiment [17], and INDOEX, the Indian Ocean Experiment [55], sought to measure and study aerosols and particulate pollution using balloon-borne instruments. Small particle counters are also in development that can serve as inexpensive or secondary payloads, and such a payload was present on many HYFLITS balloon launches [74]. Examples include the OPC-N3 [31] and the LOAC [70] optical particle counters.

With atmospheric disturbances complicating ground-based telescopes, and enormous costs associated with designing and launching instruments to orbit, the concept of near-space balloon-borne astronomy has been explored numerous times. Stratoscope II, a 36” telescope that could image in the visible and near-infrared wavelengths, was such an instrument which flew in the late 1960’s. Images of Mars, Uranus, and other stellar objects were collected [14], [15], [60]. More recent experiments include SuperBIT, the Super-pressure Balloon-borne Imaging Telescope [73], and SPIDER instruments [10], measuring between near infrared to near ultraviolet and in the 100 GHz radio spectrum, respectively. While not nearly as ubiquitous as atmospheric science balloons, astronomy payloads for scientific balloons are becoming more popular with increasing capabilities of low cost consumer electronics. The same improvements however are making space-based telescopes more accessible as well, so further increases in balloon capabilities need to be made for astronomy payloads to remain viable.

1.2.2 Balloons as a Mission Tool

Apart from supporting scientific objectives directly, balloons are often used as “launch vehicles.” In the same way rockets launch satellites to space, balloons can loft other scientific payloads to near-space where they can then perform their objectives free of the balloon system. Numerous international agencies, including the European Space Agency (ESA), the National Aeronautics and Space Administration (NASA), the Japan Aerospace Exploration Agency (JAXA), and the China Aerospace Science and Technology Corporation (CASC) have conducted drop tests of re-entry capsules and parachute systems as recently as June 2023 [26], [34], [62], [39]. Such tests often loft the test article in excess of 30 km, where re-entry vehicles reach speeds of over Mach 1.

Another example of a balloon-dropped vehicle is the HORUS (High-altitude Operational Returning Uncrewed System) glider developed by NOAA [3]. After being lofted to over 30 km, the unmanned glider returns to the ground while collecting AirCore samples of trace gasses in the atmosphere. While the regulatory landscape of balloon-dropped autonomous systems remains gray, numerous other balloon-dropped UAS ideas have been proposed.

High-altitude balloons are also increasingly popular as low barrier-to-entry tools in STEM education and outreach programs. Both at the university and K-12 levels, high-altitude balloon experiments allow for low-cost undergraduate research and exciting engagement and outreach opportunities to local schools. Such programs have been successful around the United States, often supported by university Space Grant programs [40]. Startup costs often range around only $2,000 - $3,000, with future costs thereafter covering expendables like the cost of the lifting gas and student payloads [51]. The CU Boulder ASEN 1400 and ASTR 2500 classes offer students the opportunity to design their own small balloon payloads to be flown at the end of the semester, and the class often serves as an undergrad student's first glimpse into applied aerospace engineering [43].

1.2.3 Extraterrestrial Ballooning

Balloon missions on other planets and celestial bodies have been in the works for decades. Following the USSR's VEGA mission to Venus in 1985, which inflated two small scientific balloons as its lander capsules entered the atmosphere. Floating for over 46 hours around 53 km from Venus's surface, the mission represented the first scientific balloons flown on another planet [75]. Follow-on missions have been proposed by both NASA [50] and ESA [9].

In-situ atmospheric science missions on Mars have also been of interest, with proposals for Martian balloons being a popular topic at the NASA Jet Propulsion Lab since the early 2000s [69], [42], with NASA also awarding numerous SBIR/STTR grants as recently as 2013[1] . This niche was partially filled by the Mars Ingenuity helicopter, which flew aboard the Perseverance mission, though longer duration atmospheric studies of Mars's atmosphere with in-situ measurements are

---

[1] https://sbir.nasa.gov/content/planetary-balloons-and-aerobots

yet to be conducted.

Missions to other bodies such as Titan [59] are also being considered.

1.2.4 Limitations

Balloon missions are often limited by their uncontrollability, with a requirement for balloon control often contributing significant complexity and sometimes cost to operators. Further exploration into balloon control will be conducted in the following sections, with an eventual goal of finding a method for balloon control which can provide necessary controllability without penalty.

1.3 Considerations for Control

Controlled balloons can be loosely grouped into two categories: translational control and altitude control. Further examples and investigation of both types can be found later in Ch 2. Regardless of the type of control, balloons fitted with control devices are heavier, more complex, and more expensive than otherwise.

In addition to cost, four driving factors will be used to guide the design of a new type of balloon control device:

(1) The target altitude range of the balloon

(2) The overall mass of the system

(3) The desired operational lifetime of the payload

(4) Considerations specific to instruments that may be flown on a balloon, such as the HYFLITS turbulence instrument [74]

The altitude range and apogee of the balloon and payload are important because the ambient pressure and air density drop exponentially with altitude. Any control devices which rely on airflow will operate considerably differently when used at altitudes different than what they were designed for. The HYFLITS campaign requires measurements up to 35km [74], where the pressure can be as low as 600 Pa (less than 1% of that at sea level) [65]. System mass is also an important consideration, not only from a technical perspective (where larger payloads may require a larger balloon and more lifting gas), but also from a regulatory one. The FAA's Federal Aviation Regulations[2] specifies that balloons under 6 lbs (2.72 kg) for a single payload or under 12 lbs (5.44 kg) for multiple payloads are exempt from many of the restrictions in place for large balloons and airships. These restrictions include additional reporting requirements including pre-launch authorization, periodic position reports, apogee notifications, and other reports to the FAA. In addition, specialized payload hardware is required, including radar reflectors, redundant cutdown systems, and hazard lighting for nighttime operations. Remaining below this threshold is therefore desirable to reduce the operational and logistics challenges of such balloons. Operational lifetime is the final general consideration, with control options that can last indefinitely being desirable over those with a limited duration. One additional payload consideration will also be applied, which is that the HYFLITS balloons are measuring primarily turbulence and atmospheric particulate. This means that currently, data can only be collected during controlled descents, as the wake from the balloon produces its own turbulence corrupting the measurements and the balloon itself sheds particles. Therefore, control devices that do not interfere with or further enhance the scientific objectives of such an instrument will be prioritized.

1.4 Research Goals and Outline

Ultimately, the goals of this research are to conceptualize and analyze the design of a new method of balloon control that meets the above considerations called lift augmentation, which seeks to add additional lift to a balloon through means other than changes in buoyancy. It represents the first step towards this goal and provides first-order performance characteristics of such a device. Rather than analyzing a small facet of this problem in depth, this research aims to prove the viability and advantages of the concept by addressing a large breadth of challenges associated with lift augmentation. Three primary research questions will drive this work.

---

[2] https://www.ecfr.gov/current/title-14/chapter-I/subchapter-F/part-101

(1) What are some of the mission applications that could be achieved through lift augmentation?

  (a) What forms of balloon control already exist and what can be learned about them?

  Before embarking on a new design concept, we must first explore existing forms of balloon control and understand their limitations. Concepts from these traditional control methods will inform our design, which avoids many of the shortcomings of traditional control techniques.

  (b) What are the advantages of lift augmentation compared to traditional altitude control techniques in the context of these missions?

  A brief survey of possible mission types that can be conducted or enhanced by electric lift augmentation are explored and preliminarily simulated. While more work remains to fully validate the concept across the range of missions, this serves as a motivation for further pursuing the concept.

Looking at ways to improve the data efficiency of HYFLITS balloon flights, the idea of a propeller for a balloon came to mind quickly. If multiple up and down profiles could be made, a single balloon could collect multiple launches' worth of data with a single balloon. An obvious drawback of traditional propellers, particularly if they were to operate in the thin air of the stratosphere, is their size and weight. A rigid propeller large enough to operate at these altitudes would have to be extremely large or spin very fast. Instead, a concept for solar sail spacecraft called the heliogyro was considered, as the blades generally contain few to no rigid structural members and instead derive their stiffness from centripetal forces. Such structures would be considered *gossamer*, describing something that is "light, delicate, or tenuous"[3] . A gossamer structure has much lower mass than a comparably large rigid structure but doesn't have any inherent stiffness. Further details on these ideas will be presented in Ch. 2, but initial experimentation led to an important feasibility question regarding the stability of gossamer blades.

---

[3] https://www.merriam-webster.com/dictionary/gossamer

(2) In a gossamer blade with no rigid members, is it possible to achieve static stability with enough stiffness to control the blade's lift?

  (a) What would such a statically stable blade look like?

  With initial inspiration from heliogyros, the design of an atmosphere-based gossamer blade structure began. While appearing similar in concept, we find that the effects of aerodynamics are a major factor in the stability of the blade tip, and new relationships must be sought to describe this behavior. A method of rigging the blades is found that enables passive, natural stability, something which has not yet been demonstrated for gossamer structures.

  (b) How can the performance of a gossamer blade be measured?

  Measurement of lift and drag on the blades is an important facet of determining the performance of an electric lift augmentation device. Given the flexible blades, traditional measurement techniques proven in wind tunnels such as measuring forces and deflections directly are not viable, as such interaction with the blade surface would change its shape and affect the results. Instead, a force balance is derived between the strings of the gossamer blade rigging and the centripetal and gravity loads on the blade tip, allowing lift and drag to be measured remotely. Using either optical tip tracking or stereo depth measurements, the position of the blade is determined and the internal string tensions can be solved, resolving the lift and drag acting on the blade. This measurement technique is applicable to not just gossamer blades for balloons, but possibly for measuring performance characteristics of other forms of flexible aerodynamic surfaces.

(3) What are some of the flight regimes and balloon configurations where this concept could be applied?

  (a) How and why does the lift augmentation strategy work in these conditions?

While tests can be conducted on the ground at a small scale, it is hard to determine the effects of design changes on a full scale system. A scalability model is developed that allows for trade studies to be conducted to explore these effects. Specifically, the impacts of string length, rotor spin rate, balloon size, and flight regime are explored and their impacts on overall performance are identified.

(b) What design considerations might there be for different types of balloons and mission objectives?

The idea of an "optimal" design is discussed, and general trends from the scalability models can be used for future studies of optimal lift augmentation design.

This thesis is laid out in chapters first developing a conceptual understanding of how scientific balloons behave naturally, then how existing forms of control can be added to improve their capabilities. Chapter 2 also highlights the advantages and disadvantages of traditional balloon control. Finally, given this knowledge, a new method called lift augmentation, using gossamer blades, is devised. The advantages of this new method are studied in Chapter 3, and the numerous classes of missions that such a lift augmented balloon could be applied to are overviewed. Unlike many traditional forms of control, lift augmented balloons are able to operate in many different flight regimes and in many different mission roles. A scaled test article was devised and created, the iterations of which will be described in Chapter 4. Specifically, the lessons learned and stability characteristics of the gossamer blades, specifically the tips and blade surface, will be explored and the "4-bar link" rigging method will be proven to exhibit positive stability properties. Additionally, test data from the final version of this prototype will be analyzed and compared to a theoretical model of the device. This prototype will be extended to a full scale device in Chapter 5, where the impacts of design choices for the blades and balloon system will be explored. Finally, the Conclusion in Chapter 6 will recap the findings of the research, succinctly summarize the research contributions, and begin to question what future steps in lift augmentation may be needed to enable a full scale flight.

Chapter 2

Design Synthesis

2.1 Dynamics of Balloons

Before further investigation into control can occur, we must first understand the forces which act on balloons as they rise through the atmosphere. With this, we can develop a simulator that can help characterize possible design choices. With the motivation of using balloon ascent rates to estimate vertical air motion, [91] derived a model that balances the free lift of the balloon, F_L, (Eq. 2.1) with the drag force (Eq. 2.2).

$$F_L = V(\rho_{air} - \rho_{gas})g - (m_p + m_b)g \tag{2.1}$$

$$F_D = \frac{1}{2}C_D A \rho w^2 \tag{2.2}$$

In Eq. 2.1, V is the volume of the balloon envelope, ρ_{air} and ρ_{gas} are the air and lifting gas densities, respectively, g is the acceleration due to gravity, and m_p and m_b are the masses of the payload and balloon envelope. In Eq. 2.2, C_D is the drag coefficient of a spherical balloon, A is the sphere's cross-sectional area, and w is the relative wind velocity of the balloon. By setting F_L and F_D equal, and assuming the balloon rises in still air, the ascent rate W_a is then

$$w_a = \sqrt{\frac{2F_L}{C_D A \rho}} \tag{2.3}$$

[27] built on this model by relaxing the assumption requiring a spherical balloon, opting to capture departures from spherical shapes in a modified drag coefficient. The force balance from [27] is then given as:

$$w_a = \sqrt{\frac{8Rg}{3\tilde{C_D}}\left(1 - \frac{3(m_p + m_b + m_g)}{4\pi\rho R^3}\right)} \tag{2.4}$$

where now R is the balloon's equivalent spherical radius, m_g is the mass of the lifting gas, and $\tilde{C_D}$ is the modified drag coefficient. It should be noted that this result is the same as [91] if the drag coefficient of a perfect sphere is used. Another balloon ascent model assumes a value of 0.8 for the coefficient of drag [23], and a comprehensive study of this modified drag coefficient was conducted in [57], but is limited to a single aspect of ellipsoid. [27] opted to use flight datasets to derive an experimental C_D curve, the results of which can be seen in Fig. (2.1). This indicates that drag coefficients of real balloons deviate significantly from ideal spheres.

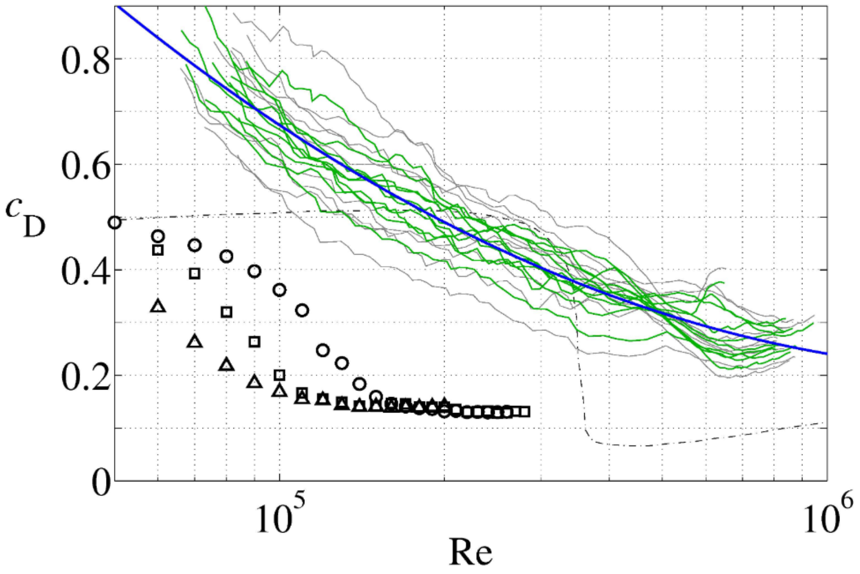

Figure 2.1: Figure from [27] showing experimental curve fit (blue) to balloon flights from the LUAMI campaign (green) compared to typical coefficients of drag for ideal spheres under different turbulence intensities (symbols) and negligible turbulence (dashed).

Ultimately, characterization of the drag coefficient of a rising balloon is lacking in literature but is not the focus of this thesis. Nevertheless, a balloon C_D of 0.8 will be selected for the remainder of this study, as it is consistent with assumptions from [23] and reasonably matches flight data from [27] despite our balloon's Reynolds number being much lower than those of the LUAMI campaign (on account of the smaller balloon diameter and much slower airspeed).

2.2 Traditional Balloon Control

As previously stated, balloon control comes in two forms: translational or altitude control (or a combination of both). While the HYFLITS campaign specifically requires altitude control of some form (see Consideration #4), research into translational control techniques can still be valuable.

StratoSail [1] was a concept proposed in 1999 that utilized a wing-like sail that hung from the balloon on a tether up to 15 km long. It had the benefit of being able to operate in a number of different configurations depending on the mission requirements, from a fully passive configuration with a fixed rudder angle to induce a bias flow (with prior knowledge of winds aloft) to a fully active system with a steered rudder. StratoSail aimed to take advantage of differing wind directions at different altitudes, with the wing structure acting somewhat like a kite pulling the balloon above it as seen in Fig. (2.2). Unlike other translational control options, StratoSail relied on wind sheer to operate, limiting its effectiveness to areas where wind sheer directions matched mission requirements.

Nonetheless, it offered the possibility of indefinite flight times (in its passive configuration, satisfying Consideration #3) and given its 15 km tether to the balloon, was designed to operate up to 35km (the sail would still be at 20 km, where the atmosphere is 10 times as dense, Consideration #1). However, despite the wing itself remaining relatively light, a 15 km tether could be as heavy as 7.5 kg on its own (assuming Kevlar thread[1] at 0.5g/m), well over the 12 lb (5.44 kg) limit from the FAA (Consideration #2). This is also considered a best case scenario, as a 100 lb line may not be strong enough to support the aerodynamic loads on the wing or even just the drag along the

---

[1] https://www.emmakites.com/products/100-500lb-braided-kevlar-line

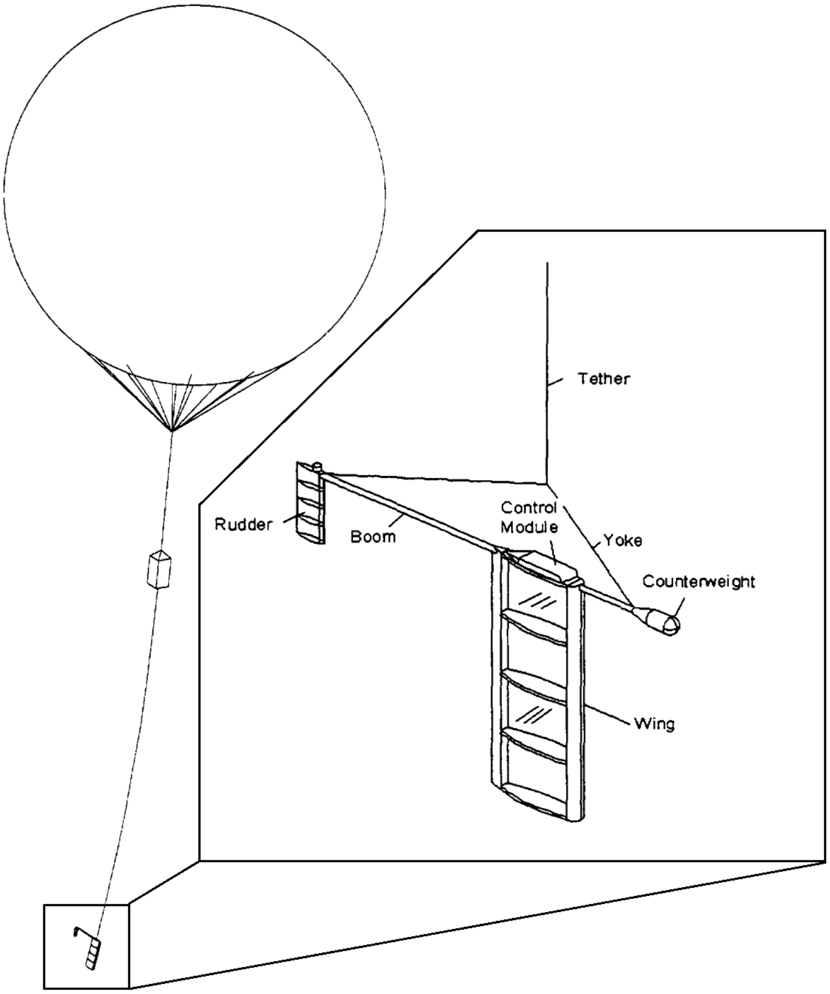

Figure 2.2: Schematic from [1] detailing the design of the StratoSail balloon trajectory control device concept.

15km tether. A stronger line could weigh significantly more. While the concept was proposed more than 20 years ago, and seemingly still under active development by Global Aerospace Corporation, it does not seem to have ever flown in a full scale configuration. Reference can only be found to the tethered airship scaled test discussed in [1].

An Advanced StratoSail was proposed that replaces the wing-like aerodynamic control surface with one more resembling a glider [2]. Such a device could be used to provide not only translation control, but also to control the altitude by pulling the balloon down or allowing it to float higher. While this does address most of the design considerations, the large, heavy tether means that it could not be used on small balloons.

Another alternative to translational control is using horizontal propellers, not unlike an airship or blimp, as described in [67] and [21]. Specifically, [67] proposes a gondola-based propeller shown in Fig. (2.3) that operates up to 36 km and with a power consumption of just under 500 W.

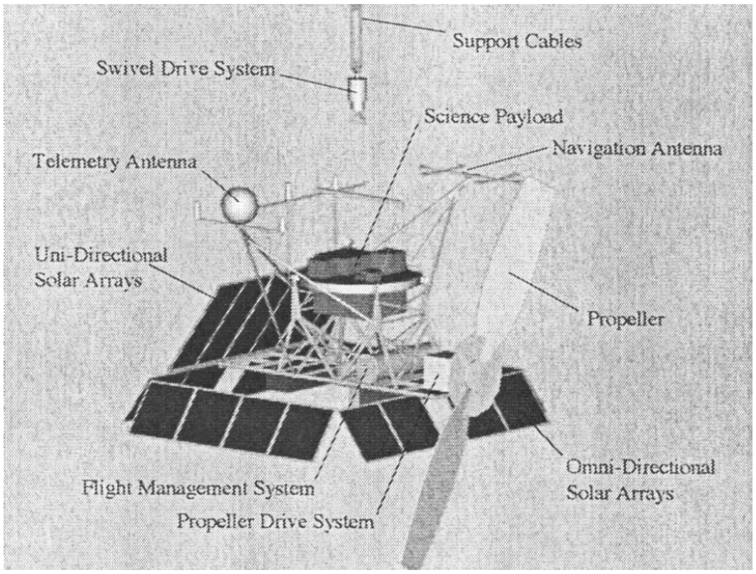

Figure 2.3: Design from [67] showing a gondola-based propeller concept to achieve translational control of an ultra long duration balloon.

This design would fit Considerations #1 and #3 well, with an operational altitude near that of the HYFLITS team and a flight duration of 3 months or more. However, the design relies on a large, expensive superpressure balloon. Additionally, the solid-structure 3.8 m propeller would add considerable mass (Consideration #2). Even just assuming a rigid foam construction[2] , the propeller could be upwards of 20 kg on its own. Further, being attached to the gondola, the propeller would corrupt turbulence measurements even more than the existing balloon wake (Consideration # 4). Technical limitations aside, a horizontal propeller closely resembles that of a traditional airship, which are regulated differently (and more strict) than balloons. Applying this concept to a small balloon could raise questions on how to regulate it, adding to operational complexity.

2.2.1 Altitude Control

In contrast with the relatively limited number of design options for translational control, there are a handful of unique ideas for altitude control of balloons. In some situations when wind shear layers meet mission requirements, altitude control can even enable some rudimentary translational control, provided the mission allows for changes in altitude to do so. This concept was analyzed in [18], where it was demonstrated via simulation that given sufficiently varied wind layers, a balloon could remain over a point on the ground within a 25 km radius for several days. This is highly dependent on wind profiles however, and Fig. (2.4) shows an instance where a launch over Boulder, CO could enable East-West station keeping, but the balloon would consistently drift to the South since there is no altitude where a southerly wind exists.

While altitude control of any kind will exhibit this property of rudimentary translational control, there are many different ways to directly control a balloon's altitude. A summary of these methods is shown in Table 2.1, and a more detailed discussion follows.

Venting is already being utilized on HYFLITS launches to enable a controlled descent from apogee through the measurement region of interest [74]. In conjunction with additional payload ballast, balloons can also be made to ascend [84]. Venting and ballast techniques offer one of the simplest, most lightweight solutions to balloon altitude control, but suffer from a major scalability problem. Control is inherently limited by how much lifting gas can be vented and how much ballast you can bring to drop. Additionally, when using latex balloons, the apogee is limited to a critical

---

[2] https://www.generalplastics.com/products/fr-4300

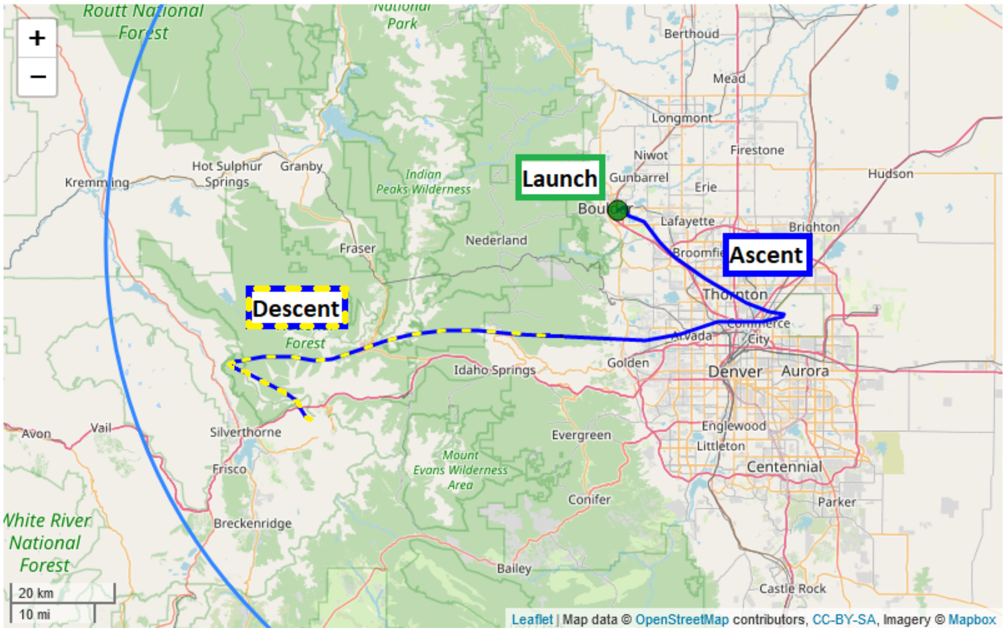

Figure 2.4: Predicted natural balloon trajectory with venting at apogee (33 km) on July 31st, 2022 demonstrating eastern and western winds with a small northerly component, making station keeping without significant southern drift impossible.

Table 2.1: Summary of altitude control techniques for balloons.

Control Method	**Referenced**	**Summary**
Air Ballast	[89]	Ballast gas is pumped into or out of a bladder inside a superpressure balloon, changing the density of the superpressure balloon to ascend or descend.
Differential Expansion	[89], [77], [18]	Air from a zero pressure balloon is pumped into or out of a superpressure envelope, resulting in a volume reduction of the zero pressure balloon and a change in buoyancy. The opposite of air ballast.
Venting and Ballast	[84], [74]	A zero pressure balloon is fitted with a vent valve and may carry additional ballast mass. When the vent is opened, lifting gas is released and the balloon descends. If ballast is released, the payload mass decreases and the balloon ascends.
Double Balloon	[47]	Two balloons are used on ascent. At apogee, one balloon is cut away and released. This results in a more controlled descent under the remaining “balloon parachute.”
Mechanical Compression	[89], [97]	A superpressure balloon is “pinched” to reduce its overall volume while the amount of gas remains the same. This results in a change in buoyancy, leading to ascents or descents.
Reversible/Phase-Changing Fluid	[69], [50]	Similar to differential expansion but uses a liquid fluid which undergoes a phase change to a gas as internal or atmospheric temperatures rise and fall, resulting in a volume change of the balloon and changes in buoyancy.
Lifting Orbiter	[8]	Similar to StratoSail but for altitude control. Uses a powered, tethered wing “orbiter” that generates lift against the balloon’s buoyancy, allowing for changes in altitude from a neutrally buoyant level.

strain where the balloon loses elasticity and can no longer expel lifting gas on its own [74]. The double balloon method is similar to venting except that an entirely contained pocket of gas is released all at once [47].

Air ballast is a popular control technique because of its relative simplicity, particularly on larger balloons. Requiring only an additional internal bladder inside an existing balloon and a pump to move this air in and out, air ballast systems have a low mass impact compared to other techniques and offer the possibility of operating indefinitely. As the ballast air only needs to be heavier than the lifting gas, often ambient air is used. A primary disadvantage however is that as the air density decreases with the ascending balloon, it becomes much harder to effectively pump. This limits the operational altitude of air ballast systems to under approximately 5km [89]. Another issue which limits its effective apogee is that of freezing air. Without conditioning the air being pumped, moisture in the air can freeze within the bladder, possibly causing ruptures [89].

Differential expansion is functionally the opposite of air ballast. Instead of pumping external air into a flexible bladder, lifting gas is pumped from a flexible, zero pressure balloon into a rigid superpressure bladder. Differential expansion exhibits many of the same benefits of air ballast systems in that it remains relatively simple and lightweight. It also suffers similar drawbacks in the difficulty of pumping low-density air, but not from the freezing issue (as the superpressure bladder can be made more tolerant to temperature fluctuations) [89]. Still, differential expansion is theorized to be effective only up to approximately 20 km [89], [18]. A final drawback of both air ballast and differential expansion is that due to the time required to pump, they are not effective at controlling balloons over short-durations, instead suited more for maintaining a specific altitude over diurnal cycles, as demonstrated in [77].

All of these methods take advantage of transporting air around the system in some way, often quite difficult to do at high altitudes and for a small amount of power. A solution which can operate on electricity is desired because this could allow a balloon to potentially operate indefinitely, using solar panels to power the control system. The balloon would also be operating above the clouds, so batteries would only need to be sized to operate through the night rather than having to account for unpredictable atmospheric obstructions. This would necessitate a low power consumption control scheme however, as solar panels could quickly start to contribute to a significant fraction of overall payload mass, reducing the available mass for scientific payloads.

Mechanical compression is one method that could operate electrically and doesn't require air transport from one reservoir to another. By pinching or compressing the outer balloon envelope, the balloon's volume decreases (with a corresponding increase in internal pressure). From Eq. 2.1, this results in a smaller balloon lift thereby causing a reduction in float altitude until the ambient air density increases to compensate [89]. This may also correspond to a change in balloon drag, the direction and magnitude of this change would be dependent on how the balloon was compressed [97]. The force required to compress the balloon tends to zero as the superpressure difference decreases, so control could be accomplished with extremely lightweight and low power actuators [89]. However, the altitude range that can be achieve depends on how much the balloon can be compressed, and without complicated structures and multiple compression actuators, volume change is only on the order of approximately 50%, resulting in only a handful of kms of control authority [97]. It also requires the use of superpressure balloons, which are more expensive and not being used by the HYFLITS team.

Another method utilizes a phase-changing fluid, which is a liquid at one temperature and pressure in the flight regime and a gas at another. This concept was tested at JPL in 1994 called the Balloon **AL**titude **C**ontrol **E**xperiment (ALICE) [69]. In the tests, refrigerant R114 was used, which transitions from a gas at sea level to a liquid above approximately 4-7 km. While this would not be very applicable to the HYFLITS team, the original ALICE testing was to validate the same concept for use on Venus. Similar concepts have been proposed using water as a lifting gas on Venus, which would target different altitudes [50]. While the concept is simple and lightweight, its sensitivity to specific atmospheric conditions makes it unsuitable for general balloon control.

The final method discussed is a design explored by a Senior Projects Team at CU Boulder called a High Altitude Lifting Orbiter (HALO)[8]. HALO uses a small wing on a 5 m tether to augment the lift of the balloon by using a built-in propeller to produce airflow and lift on an orbiting wing. The wing, made of lightweight foam and designed with similar constraints in mind to the HYFLITS team, weighs less than 1.5 kg. Further iteration on this concept could improve performance. This idea is fundamentally different from the others presented in that rather than modifying an existing variable in the free lift equation, it introduces an entirely new “augmented lift” term as seen in Eq. 2.5.

$$\tilde{F_L} = V(\rho_{air} - \rho_{gas})g - (m_p + m_b)g + L \tag{2.5}$$

With existing concepts understood, it is clear that none currently meet all design considerations. While propellers have the downside of being relatively heavy, they do offer the possibility of being powered electrically. Such a device could draw from existing research on propellers and low speed flows. Consideration would need to be given to sufficiently distance the concept from that of an actual airship, and the challenge of the extremely sparse atmosphere above 20 km and on other planets needs to be addressed.

2.3 Gossamer Structures

2.3.1 Overview

The term *gossamer* describes something that is “light, delicate, or tenuous”[3] . In an engineering setting, a gossamer structure is one which is designed to be ultra-low mass, or have much lower mass than comparably large rigid structures. Human-made gossamer structures are mostly confined to space, with a specific class of solar sail called the heliogyro notably similar to the idea of a propeller.

2.3.2 Heliogyros

Historically, solar sails have been designed as a square with membrane sheets structured with central masts. These sails range from as little as 3m in length for use on small spacecraft like the

---

[3] https://www.merriam-webster.com/dictionary/gossamer

NASA NanoSail-D mission [38], 10-20 m for ground-based tests of scaled deployments [38], [64], and up to 160 m or more in analysis of full scale sail systems [92]. While gossamer, these solar sail designs typically still use a rigid, expandable boom as the central masts, contributing to a significant mass fraction compered to the sail system overall (90% in the case of the HIPERSail concept [94]). A different kind of gossamer structure is desired, one which derives its stiffness from another source than rigid bars or beams and more closely mimics the jib sail from before in terms of structure.

One such gossamer structure being researched is called the Heliogyro, shown in Fig. 2.5. Rather than booms and masts, the sail area of the heliogyro is tensioned via centripetal forces resulting from a spinning spacecraft and weights positioned on the tips of each blade [95]. A NASA demonstration mission called HELIOS proposes a 6-blade design with blades 220m long, providing nearly 1000 m^2 of sail area compared to the HIPERSail's 500 m^2. Further, because the device's structure is derived from tensioned blades rather than booms, the deployment and blade structure make up only 60% of the sail system's mass [93].

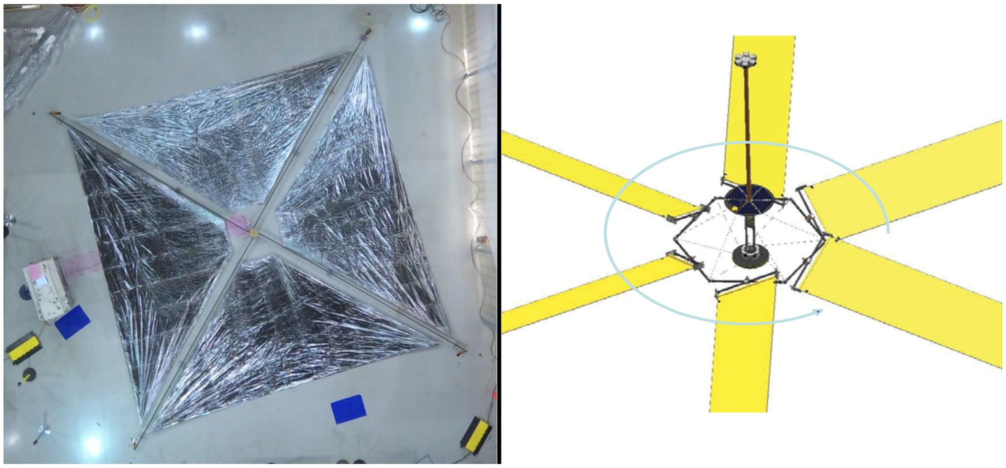

Figure 2.5: Scaled deployment test from [94] of a traditional square solar sail (left) compared to the HELIOS concept from [93] of a heliogyro (right).

Considerable effort recently has gone into characterizing the dynamics of the heliogyro blades [6], [12], and how to control them [6], [11]. A large part of this challenge comes down to the fact that the primary source of external forcing on the blades is from solar radiation pressure rather than from traditional aerodynamic forces like on helicopter blades and propellers. Such pressure does not produce a moment on the blades, which is produced in the generation of the aerodynamic lift that provides thrust to the balloon system. At 1.0 AU, this solar radiation pressure is on the order of micro-Pascals (10^{-6} Pa), imparting only milli-Newtons of force on a 1000 m^2 blade system. This is a fundamental difference between a heliogyro and a similar design that would operate in an atmosphere, which could generate a handful of Newtons of thrust. Further investigation will need to be done to understand the impacts of this difference.

2.4 Low Reynolds Number Aerodynamics

This motivates an investigation into airfoils and propeller technology that would be applicable at the high altitudes of the stratosphere, characterized by chord Reynolds numbers varying from 10^4 down to 10^2 depending on the blade geometry.

In general, lower Reynolds numbers result in lower lift:drag ratios, with conventional airfoils at Reynolds numbers above 10^7 being able to reach C_l/C_d ratios of over 100 [96]. A large lift:drag ratio is important in this application because increased drag requires more torque to spin the propellers, possibly requiring larger, heavier motors and consuming more power for the same amount of lift.

Different airfoils have been developed to compensate for this and to attempt to maintain performance even as the Reynolds number decreases. This is of particular interest recently with the growth of micro air vehicles (which typically operate in the Re range of 10^4 - 10^5). Below this, achieving L/D ratios of even 10 can be a challenge. Some research has suggested that reversing the airfoil (so that the traditional trailing edge becomes the leading edge) actually leads to better performance at Reynolds numbers below 10^4 [96]. Figure 2.6 shows a comparison from [96] that compares different airfoil configurations at 4 different Reynolds numbers.

It can be seen that even flat plates outperform traditional airfoils at low Reynolds numbers, with cambered or billowed flat plates performing even better still. The major technical drawback of translational propellers on balloons is their requirement to be very large (as in [67] and [21]). An alternative is to spin very quickly, as is the case of the Mars Ingenuity helicopter. Its carbon

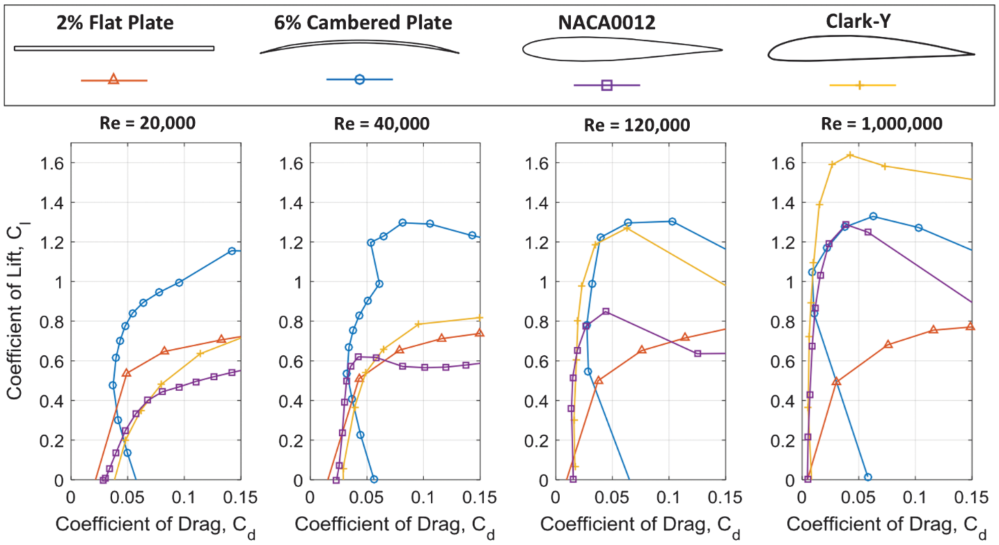

Figure 2.6: Results from [96] detailing the effects of Reynolds number on various airfoil drag polars.

fiber propeller spins at nearly 3000 rpm (compared to the rate of traditional helicopters in the 100s of rpm) and operates in the thin Martian atmosphere [4]. While the entire craft weighs only 1.8 kg, it requires up to 500 W of power and can only operate for as little as 90 seconds before needing to land and recharge [4]. However, literature on the helicopter design even suggests that the airfoil geometry is not necessary [4]. Further, a rigid propeller is not even necessary in the application of a balloon, opening the door for a flexible propeller whose structure is gossamer, allowing for a large propeller area while remaining extremely lightweight. This is supported by research and experiments on 2D membrane airfoils that take the shape of a cambered plate in steady flow conditions [16], [81].

Still, these studies do not provide concrete data down to the Re that a scientific balloon may want to operate at. Sunada et al. [83] performed water flume experiments of various airfoils down to $\mathrm{Re} = 4 \times 10^3$, well within the region of operation for a propeller operating in the stratosphere. Their findings supported prior work that conventional airfoils were outperformed by flat and cambered plates, and suggest that max L/D ratios of between 5.5 and 8.6 could not only be achieved, but could be achieved at angles of attack up to 14 degrees (in the case of the most cambered airfoil tested). This work was later reviewed in [76], which also compared other papers related to low Reynolds number airfoil aerodynamics, and found that the results from Sunada et al. were consistent with other more recent studies, if not a little optimistic.

If a low Reynolds number aerodynamic surface can produce enough lift without too much drag, then a propeller could be powered by an electric motor, retaining the benefit of indefinite flight times. Furthermore, a long propeller could position instruments on its tips, displacing them from the wake of the balloon on ascent. How would such a large propeller remain structurally stable?

2.5 Flexible Airfoils

Recent research suggests that for low Reynolds numbers, flexible airfoils inspired by nature may outperform rigid equivalents [33], [29], [82]. A gossamer blade is by definition flexible, so further survey into this area of aerodynamics is needed.

2.5.1 Present Focus: Insects and Birds

Flexible wings are extremely prevalent in nature, quite the contrast to human-made flying contraptions which are dominated by rigid wing sections. With their lightweight construction, ability to change shape to adapt to uncertain conditions, and the fact that many species of birds and insects can tuck away their wings to protect them when not flying, flexible wings have a multitude of advantages. Such flexible wings require new tools to predict simulate and analyze, as the elastic behavior of the wing surface can greatly affect their performance. The field of Aeroelastics focuses on this study, with the Weber number We seen in Eq. (2.6) often being used to describe the relationships between a materials stiffness and its aerodynamic loading [29]. In Eq. (2.6), C_N is the chord-normal force coefficient, ρ is the fluid density, U is the freestream airspeed, c is the flexible blade chord length, E is the membrane's Young's modulus, and h is the membrane's thickness.

$$\mathrm{We} = C_N \frac{\frac{1}{2}\rho U^2 c}{Eh} \tag{2.6}$$

While the research in [29] and in [46] both focus on flapping membrane airfoils, insights from flexible membrane theory can still be useful even if our propeller is not designed to flap. In particular, it was confirmed experimentally that membrane flexibility typically expresses as an increase in camber of the aerodynamic surface, improving L/D performance, especially at high angles of attack. Additionally, the Webber number fully characterizes the membrane's maximum camber as long as the natural tension in the membrane is known and assuming that the lift distribution across the membrane is uniform [82].

In addition to increases in L/D performance, [85] studied the effects of flexible airfoils at extremely low Reynolds numbers ($9000 > \mathrm{Re} > 100$) and found that flexible airfoils exhibit a natural pitching frequency as a result of aerodynamic loading. While in rigid airfoils this would amplify the apparent angle of attack, in flexible airfoils, it acts to smooth out fluctuations in lift.

Nevertheless, these studies all focus on flexible membranes that both deform and stretch. In its simplest form, a gossamer blade could be made of materials which deform easily but are otherwise inextensible. In this case, a detailed analysis of the aeroelastics of the blade itself is not necessary, as it does not exhibit elastic material properties. Instead, the blade exhibits aeroelastic dynamics due to restoring forces (stiffnesses) resulting from a change in string/blade tension due to changes in string geometry. Thus conventional material stiffness plays no role, rather geometrical stiffness becomes an issue in gossamer structures.

2.5.2 Aerodynamics of Sails and Inextensible Airfoils

Despite their use since at least 6000 BCE [30], it was not until the 1960s that theoretical work on the aerodynamics of sails began. Much like with airfoils, work on sails began studying 2D sails, with [87] first work on the subject following standardized linear airfoil theory with an additional equation constraining the location of each sail element. While the paper serves as a stepping stone for further investigation into 3D sails, Thwaites goes so far as to speculate that analytical solutions to the behavior of sails will never be found, instead settling on a numerical approximation. Generally, it was discovered that the lift coefficient of a sail exceeds that of a flat plate, following the relation in Eq. (2.7), where c is the sail's chord length (called the distance between the luff and leech in sailing) and l is the linear length of material between the luff and leech.

$$C_{L,sail} = C_{L,plate} 1.636\sqrt{l/c} \tag{2.7}$$

Following this relationship, it could be inferred that a billowed blade with a chord length of 0.2 m and an excess length of 1 cm (so l is 0.21 m) could have a lift coefficient of 1.838, assuming the flat plate follows a 2π lift curve slope and both airfoils are at 10^o angle of attack. This is higher than what was measured in [83], but the low Reynolds number of that experiment may complicate the simplified relationship.

Additional work in [66], surveyed more recent studies of 3D sails, and [58] presents a comprehensive study of sail shapes against their performance. Still, Thwaites remains correct in his statement of an analytical solution remaining unsolved.

2.6 Conceptual Design Summary

Through this literature survey, existing balloon control techniques were studied and analyzed for their applicability given the unique design considerations being applied outlined in Ch. 1. A system which controls the altitude of the balloon is required which can be powered and controlled electrically. Such a device would enable the possibility of indefinite flight times. Further, a design that took advantage of the simplicity and thorough understanding of propellers led to an investigation into the performance of flexible airfoils and airfoils at low Reynolds numbers. In the balloon's operating altitude of 20-35 km, Reynolds numbers are expected to be in the range of 10^4 to 10^2. It was found that at these extremely low Reynolds numbers, the precise shape of the airfoil was of little importance, and instead that flexible, sail-like structures performed just as well if not better than most airfoils. While some preliminary work on these kinds of airfoils was found, detailed aerodynamic analysis and performance figures are not a priority of this research. For now, analysis will assume that L/D ratios of 7 can be achieved, which strikes a middle ground between the findings from [83]. Even with a flexible construction keeping the blades lightweight, some structure is required which led to an investigation of lightweight gossamer structures. While boom and mast structures like those used on maritime and solar sails present a good option, the centripetally tensioned blades of heliogyros allow for even lower weight. Additionally, the blades can be made extremely long, enabling lower propeller rotation speeds at altitude for the same lift compared to smaller propellers. Finally, as these heliogyro-like blades would need some form of tip weight, the possibility of positioning instruments on the tips would enable turbulence instruments to remain outside of the balloon wake, enabling measurements on both ascent and descent. Such a design positively addresses all of the considerations laid out in Ch. 1 by adding the lift augmentation term, L as in Eq. 2.5 (and reproduced below), to the balloon free lift in Eq. 2.1.

$$\tilde{F_L} = V(\rho_{air} - \rho_{gas})g - (m_p + m_b)g + L$$

Chapter 3

Applications

Unlike many other forms of balloon control, lift augmentation can be applied to numerous different kinds of missions with very little hardware modification. In addition, the test apparatuses and procedures developed as part of this thesis are applicable beyond testing gossamer propellers for scientific balloons, and can be used as a baseline for future tests of flexible or other low Reynolds number aerodynamic tests where performance must be measured remotely rather than directly.

This chapter focuses just on the possible mission classes that a lift augmented balloon could fulfil, with discussion regarding the test rig reserved for Ch. 4 and 6.

3.1 HYFLITS: Profiling

The HYFLITS campaigns focused on collecting turbulence data in the lower-mid stratosphere and conducted over 100 launches of small latex balloons over an approximately 5-year period. Figure (3.1) depicts a timeline of launches from all collaborators of the HYFLITS MURI (Multi-University Research Initiative), with half-height bars indicating launches with *either* turbulence or particulate instruments only, and full height bars representing flights with both instrument packages.

Ideally, HYFLITS balloons could conduct multiple up and down profiles of the atmospheric region of interest, though due to the complexities of doing so, instead were designed to reach a target apogee and then descend at a constant rate through the measurement region by utilizing a venting system. Due to the wake of the balloon causing turbulence on ascent, any turbulence data collected prior to apogee is corrupted, so only descent data is useful. While the balloon's

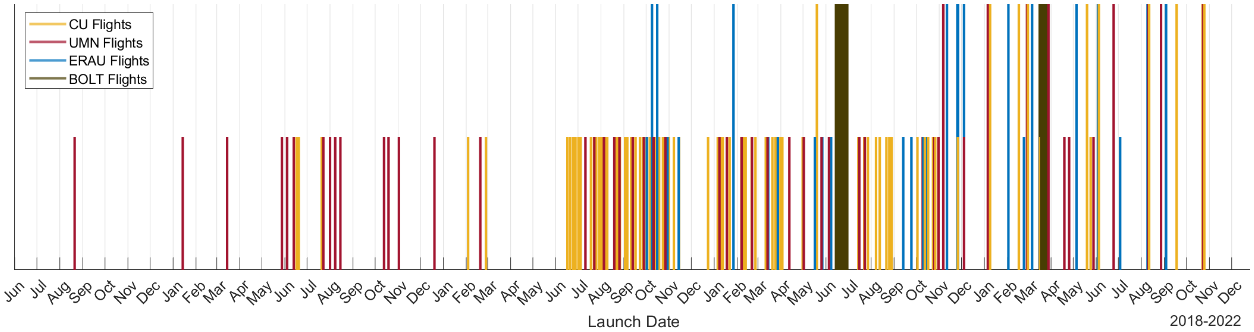

Figure 3.1: Timeline of HYFLITS launches from 2018 - 2022.

wake doesn't affect the particle measurements, particulate shedding off of the balloon's surface is hypothesized to bias the particle count data obtained on ascent as well.

A lift augmentation payload as part of the HYFLITS payload string could enable measurements throughout the flight, as instruments could be positioned on the blade tips well outside of the wake of the balloon. Additionally, multiple up and down profiles could be made, greatly improving the already high cost-to-data efficiency of HYFLITS balloons.

A lift augmented balloon, when properly equipped with sufficient solar and battery power, is only limited by the balloon material's lifetime and leakage of lifting gas. Even inexpensive latex balloons, which degrade in the sun after as little as 3 days [84], would still enable at least 24 profiles if well sealed (48 total sets of turbulence data since it can be taken both on ascent and descent). Even if ground stations are only available to cover half of these, that still gives 24 balloon's worth of data for a single launch.

3.2 Area Targeting

Targeting of a specific area is of great interest to communication and observation ballooning missions. Normally reserved for large balloons with heavy and expensive control systems, lift augmentation offers a method for targeting wind layers and targeting areas of interest in a small and inexpensive package. The guidance method from [18] was integrated into a simplified balloon trajectory simulator which contained an idealized wind field as described in Fig. (3.2) and the full balloon dynamics models from [27].

According to [18], the balloon guidance controller is programmed to approach a target location above the ground within a specified distance by maximizing the overlap of the wind vector at a given altitude with a vector pointing to the target. Whatever altitude this maximum occurs at becomes the target altitude of the balloon, and an augmented lift of ±1 N (approx. 1 m/s translation speed) is applied.

Over the simulation time of over 18 hours, the balloon launches from Boulder, CO, and traverses across the Midwest to loiter West of Minneapolis. This is seen in Fig. (3.3). Figure (3.4) shows the altitude profile of the balloon, which ascends and descends multiple times in order to remain at the target altitude.

Future improvements could integrate the lift augmentation controller into the full MATLAB or Python Balloon Trajectory Simulator which samples wind profiles from the Global Forecasting System (GFS). Such a model would give a much better picture of the capabilities of lift augmentation under non-ideal and non-steady winds. In contrast, the wind model integrated here was carefully crafted to provide winds in all directions within the operating envelope of the lift augmented balloon, ensuring that all regions would be reachable, which is often not the case in reality. Nevertheless, it does demonstrate that translational control is achievable via lift augmentation, which nominally only provides direct control over altitude.

One of the limitations of lift augmentation for balloons is that the achievable translation rates are slow compared to the speed at which the winds can change. The current guidance controller has no way of looking into the future and accounting for future wind conditions. Another improvement then is to incorporate reinforcement or machine learning techniques into the guidance algorithm. One simple version of this could use Value Iteration, though this would not account for changing or uncertain wind fields over time. Multiple policies generated from a value iteration approach could be mixed together to attempt to account for this, though the computational burden of running value iteration with a reasonably small spacial resolution across the large areas balloons often cover is non-trivial. Some way of restricting the domain to just regions of immediate interest could improve

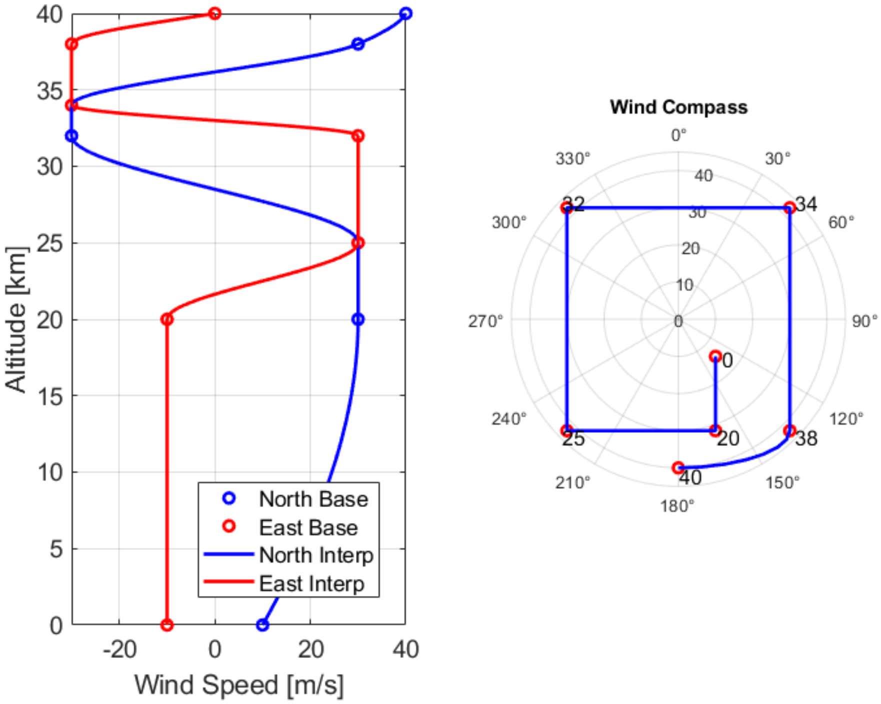

Figure 3.2: Simple wind field for balloon targeting. Ensures winds in all directions within the flight regime.

Figure 3.3: Groundtrack of a simulated lift augmented balloon.

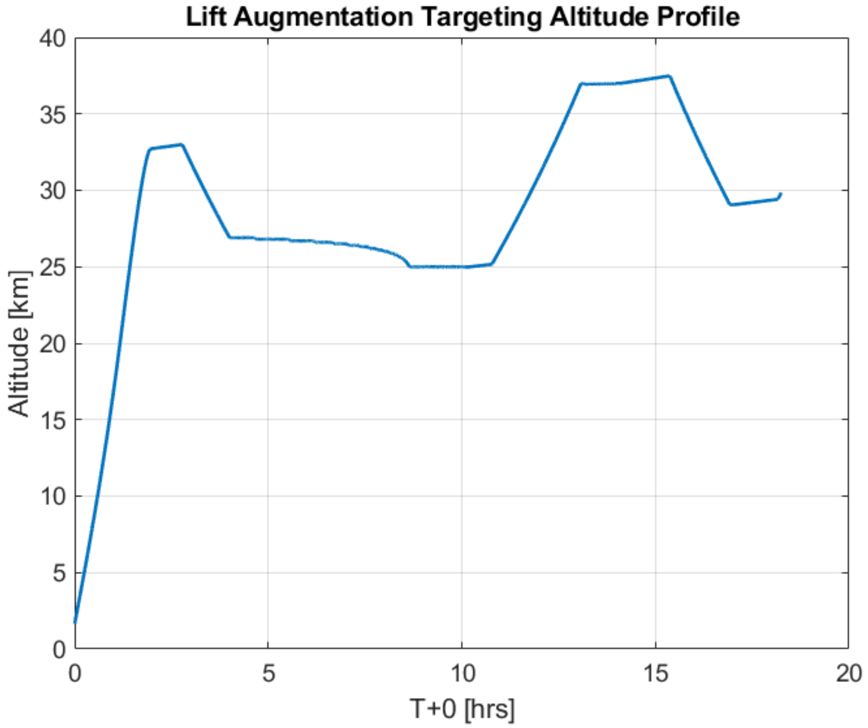

Figure 3.4: Altitude profile of a simulated lift augmented balloon over the course of 18 hours.

this.

3.3 Long Duration Ballooning

Another mission area usually constrained to larger balloons, longer duration missions typically require some way to harvest and store energy for later use (especially when attempting to operate at night). While a lack of balloon control, lift augmentation or otherwise, does not preclude smaller balloons from carrying their own solar panels and operating for longer durations, their inability to stationkeep restricts them from missions which require stable altitudes, particularly astronomy missions. Lift augmentation control enables long duration altitude stability, potentially indefinitely, on balloons of any size.

Further investigation into power consumption will be conducted in Ch. 5, however as a baseline, a medium-sized lift augmentation device can draw as little as 20-30 W of power during a 1 m/s traverse. High-performance commercial solar cells, when panelized, can achieve this level of instantaneous power output relatively simply. Maxeon Gen III cells[1] provide up to 3.54 W per cell, the downside being they generate very low voltages of only 0.6 V. Rocket Lab's SolAero cells[2] , when panelized to the same dimensions as the Maxeon cell, output 6.3 W at peak power and also address the voltage shortcoming, generating 3.5 V with a single cell. Both options, shown in Fig. (3.5), are also extremely lightweight, contributing on the order of 10s of grams depending on the panel size.

Data from the RACOON flight experiments [48], which was designed to take advantage of diurnal cycles to profile the atmosphere over long durations, experienced swings of up to 20 km over a full 24-hour day-night cycle. Data for the rates of this altitude change or the thermal time constant of the lifting gas are not provided, and building a separate thermal model is not in the scope of this research. However, assuming these altitude variations occur over the course of half a night, 6 hours, a translation rate of 0.92 m/s would be achieved. This would be the rate at which

---

[1] https://us.sunpower.com/sites/default/files/sp-gen3-solar-cell-ds-en-a4-160-507816f_0.pdf

[2] https://www.rocketlabusa.com/assets/Uploads/RL-SolAero-Data-Sheet-Z4J.pdf

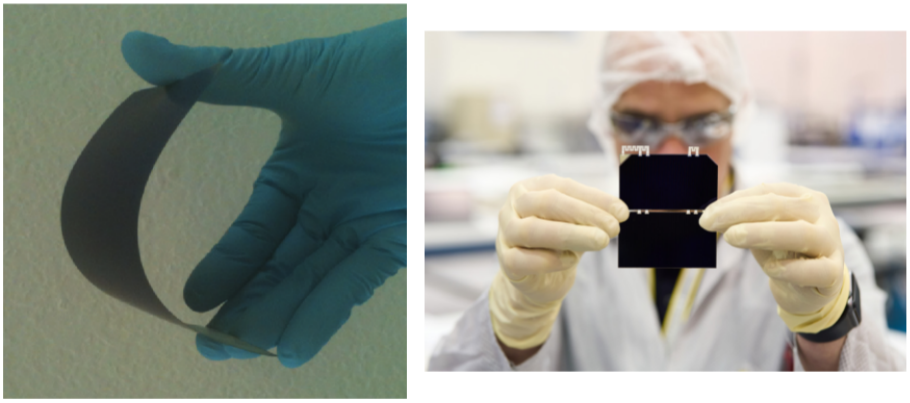

Figure 3.5: Maxeon (left) and SolAero (right) solar cells, both of which could be panelized to meet the power requirements of a lift augmentation device.

a lift augmentation system would need to offset in order to counter the loss of balloon lift as the lifting gas cools, representing an approximate 10% loss of balloon free lift [84]. Over the full 12 hour night, this adds up to 360 Whrs of energy capacity (1,296 kJ) that needs to be stored to operate continuously without solar power (representing a 2x FoS on the modeling that will be discussed in Ch. 5). Using modest LiIon cells[3] at 3.6 V with a capacity of 3350 mAh, approximately 30 cells would be needed. Taking into account cell efficiency and losses, an additional 20% margin brings this total to 36 cells. At only 49.5 g per cell, the batteries to operate continuously at night contribute only 1.76 kg of mass, which remains well below the FAA threshold and provides margin for both the lift augmentation system and scientific payload.

3.4 Extraterrestrial Ballooning

Another mission class where lift augmentation could excel is that of scientific ballooning on other planets. Any of the mission concepts above would be applicable and needed, but given the rarity of atmospheric science missions to other worlds and the competitiveness of payload allocations, scientific and engineering hardware included on space missions face an even higher barrier to efficiency than in terrestrial applications.

Much like in the HYFLITS profiling case, being able to multiply in-situ data collection opportunities with the same balloon hardware would be vital to any balloons flying on other planets. This is one of the reasons it was so important for the Mars Ingenuity Helicopter to be able to land and recharge. If it could only conduct a single flight, its usefulness would be extremely limited.

Other control techniques already exist which could enable long duration missions on other planets, but lift augmentation incorporates at least two vital improvements over alternatives: its design does not rely on known or consistent atmospheric conditions and it can be made extremely small and lightweight (at least compared to alternative control strategies). Control systems utilizing mechanical compression or phase changing fluids require complex and expensive hardware and/or

---

[3] https://industrial.panasonic.com/ww/products/pt/lithium-ion/models/NCR18650GA

a known atmospheric composition that does not vary much.

Instead, the aerodynamic nature of lift augmentation allows the device to produce as little or as much lift as is required (within an upper physical limit) to meet mission needs. Additionally, the gossamer blades and propulsion system can be scaled across a range of balloon sizes. Much like the VEGA missions in 1985 [75], multiple smaller balloons can be sent, reducing risk and resulting in more data returned for a single launch.

3.5 Impacts of Lift Augmentation on Traditional Ballooning Missions

Unlike many other forms of balloon control, lift augmentation can be directly applied to perform a wide variety of balloon maneuvers in many different types of missions. Specifically, lift augmentation can be used as a "data multiplier" in campaigns where multiple launches occur or the capability to launch is severely limited.

With lift augmentation, a single balloon could perform multiple ascents and descents, enabling campaigns like HYFLITS to convert their 100 launches from 100 turbulence datasets to over 2400 by collecting data over a dozen profiles on both ascent and descent. Astronomy missions which require precise altitude stability could operate indefinitely, not limited based on lifting gas and ballast. On future extraterrestrial missions, these impacts are multiplied further by the rarity of such flight opportunities and the value of any data collected. By taking a lift augmented balloon to another planet, longer duration science missions could be conducted and more balloon experiments could be included.

This survey of missions, while aspirational and speculative, motivate continued work in lift augmentation, as it is clear that it could impact a large part of the current scientific ballooning landscape.

Chapter 4

Blade Stability and Performance

4.1 Heliogyros and a Terrestrial Equivalent

The heliogyro represents the most similar concept to our gossamer blade for lift augmentation, following the same principle of spinning a long blade without any inherent stiffness to provide rigidity. Traditional heliogyros suffer a dynamic instability problem, which shows up as out-of-plane vibrations and a twisting motion along the blade span, a phenomenon which has been well studied on the HELIOS concept of heliogyro [93]. For rotations of 1 RPM, it was found that these instabilities were excited for solar radiation pressures above 41×10^{-6} Pa.

While aerodynamic forces are orders of magnitude larger than this, it was initially believed that much smaller blades (on the order of a couple of meters compared to HELIOS's 220 m blades) and much faster spin rates would still result in blade stability provided the initial spin-up period could be passed. An initial prototype which closely mimicked the blades of the heliogyro was conceived and tested.

4.1.1 V1: Passive Tip Weights

The blades of a gossamer propeller derive their structure from the tension within strings and cables as they spin, creating a centripetal force pulling a mass on the ends of the strings up and out. This system is easily simplified and modelled, and such simplifications can help answer basic questions to determine feasibility. First and foremost, it can help determine if the required spin rate is simply too large to achieve with limited power and weight constraints. A free body diagram of the simplified tip-weight system is shown in Fig. 4.1. In a static condition, the centripetal component, F_c, of the tension force, F_t, must equal the angular acceleration of the tip weight. Gravity, F_g, and the vertical component of the tension, F_r, must cancel each other out. This leads to a simple force balance, Eq. 4.1, and a relation through Newton's second law, Eq. 4.2:

$$F_r = F_g = mg = F_c \tan\theta \tag{4.1}$$

$$F_c = m\omega^2 l \cos\theta \tag{4.2}$$

Substituting 4.2 into 4.1, a relationship between the angular velocity, ω, and the coning angle, θ, can be derived as seen in Eq. 4.3 where g is the acceleration due to gravity and l is the string length. While the blade surface is not shown in Fig. 4.1 because the blade is approximated as a string, the balloon's augmented lift is derived from the lift of the blade itself, so reduction of the coning angle is critical. If the blade is tilted, the lift component in line with the balloon's buoyancy will be reduced.

$$\omega = \sqrt{\frac{g}{l \cos\theta \tan\theta}} \tag{4.3}$$

Initial testing of the tip weight concept began in April 2021. Consisting of a modified off the shelf ceiling fan and strips of lightweight tarp, the approximately 2m long blades were fitted with metal tubes to act as tip weight. The simplified model would suggest that to achieve a coning angle, θ, of 45^o, the fan would need to spin at approximately 0.6 rotations per sec (RPS). The speed of the fan was controlled with a VariAC variable transformer and tests were conducted in the ASPEN Lab. Figure 4.2 shows the results of the test at three time instances.

As soon as any appreciable rotation speed is applied, the blades immediately orient themselves normal to the flow. This causes an increase in drag which dominates centripetal forces and the blade tips lag the root. Eventually, this causes the blades to tangle up entirely, as can be seen in the figure. With much shorter blades, centripetal forces were able to overcome this drag and it was

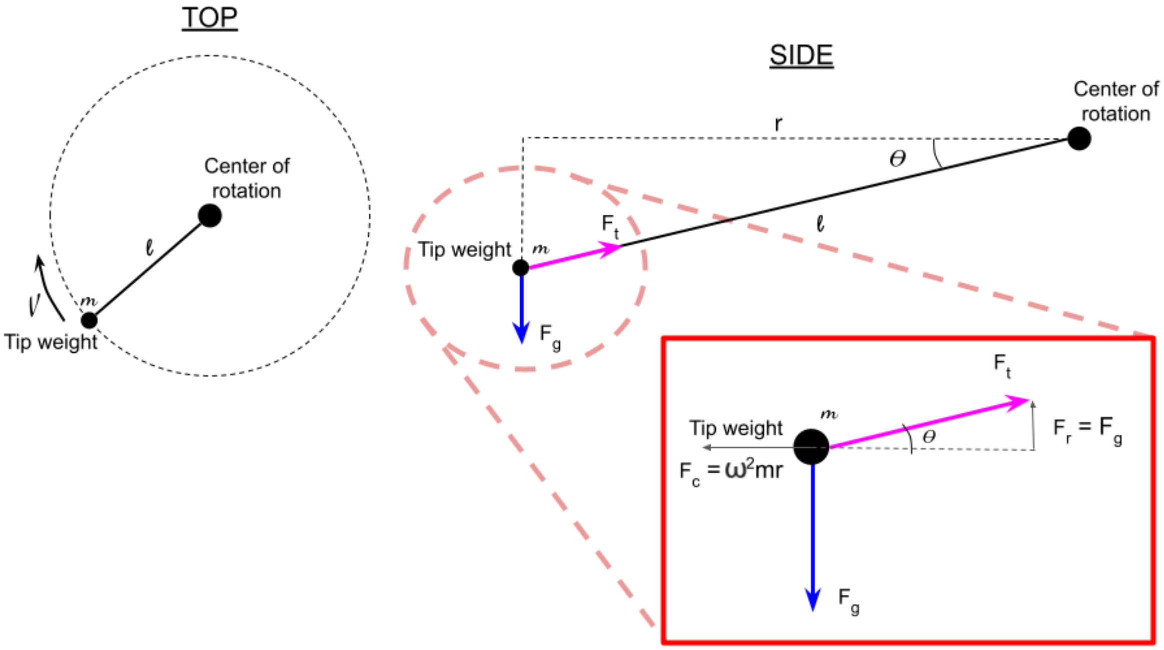

Figure 4.1: Free body diagram of a simplified lift augmentation system considering just a spinning weight on the end of a tether.

Figure 4.2: Bottom and side views of the first lift augmentation prototype as it speeds up.

found that the tips settled into a natural pitch oscillation, resulting in the angle of attack of the blades varying wildly between $\pm 90^o$, resulting in no appreciable or consistent lift.

At this point, it was thought that in order to stabilize the blade and generate consistent lift, some form of active control of the blade tips would need to be implemented to dampen this pitch oscillation. Pitch damping was indeed a requirement for heliogyro blades. Through further experimentation, it was discovered that pulling on the leading and trailing edges of the tips would result in changes in the tip angle of attack. A new prototype was developed to implement and test this theory.

4.2 Active Stability

4.2.1 V2: Active Tip Control

In February 2022, test of the second version of the prototype test rig began. This was the first ground-up redesign of the lift augmentation system, which now incorporated onboard inertial sensing from a gyroscope to detect oscillations and a closed loop control system to drive these oscillations to zero. Figure 4.3 and 4.4 show the tip control prototype.

The onboard controller was designed to damp oscillations in pitch and roll above 2 Hz by utilizing a high-pass filter and a simple proportional control loop. This was effective in damping out perturbations from natural drafts within the testing lab and from test conductors physically knocking individual blades off course. The string arrangement utilized pairs of low-elasticity kite string, one pair on top and one on the bottom, both meeting on the tip at the leading and trailing edges. The bottom strings were directed to the center of rotation of the fan, while the top pairs met at a point where the fan blades would normally attach. Figure 4.5 shows this arrangement during a test with one of the blade's strings highlighted.

These tests continued with further refinement of the rigging and control system, leading to increased rotation speed (0.4 RPS initially up to 0.63 RPS) and a reduction of the coning angle (approximately 70^o to 50^o). While this was effective at stabilizing the oscillations from the initial

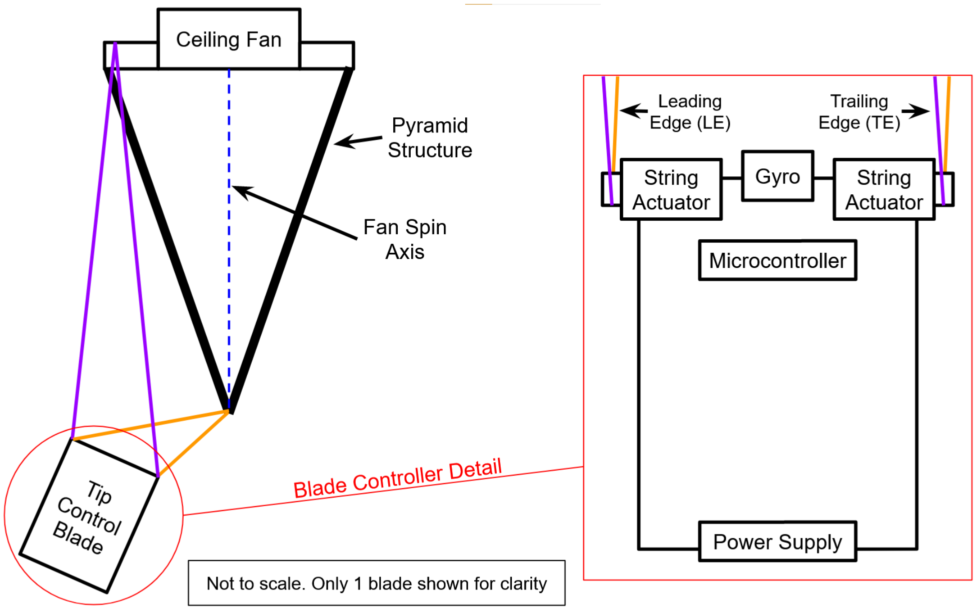

Figure 4.3: Schematic showing the major components in the V2 blade controller prototype and test rig.

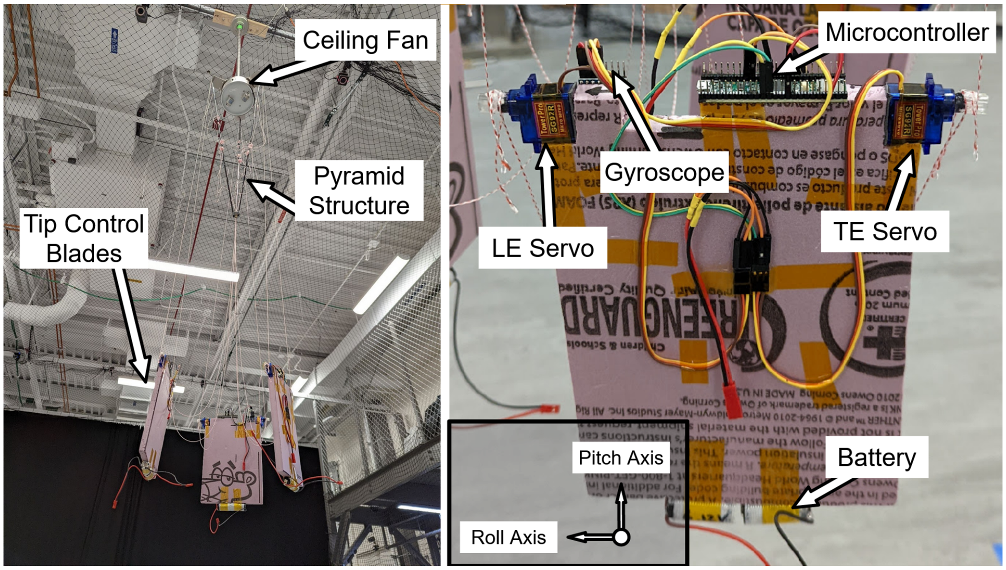

Figure 4.4: Full lift augmentation V2 prototype (without blade membrane) and detail view of a single tip control blade.

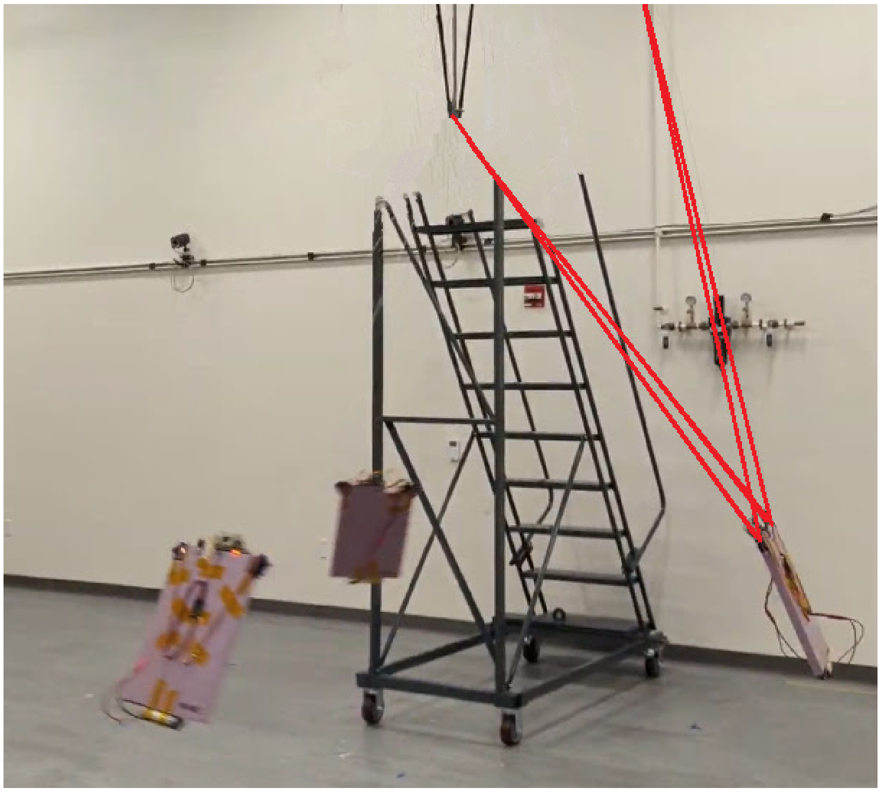

Figure 4.5: Image of stable blade rotation with rigging lines highlighted. Note that a portion of this picture was edited to make the rigging connection to the prototype more clear.

tests two new questions arose:

(1) Now that the blade tips can be stabilized, how can the blade tip angle of attack, which influences the angle of attack of the entire blade, be set?

(2) How would such a device be deployed without tangling?

Blade control was implemented by tying the top and bottom strings together around the servos such that when the top string was unspooled, the bottom was spooled up. This results in the top string getting longer and the bottom shorter. This could be done separately on the leading and trailing edges (LE and TE), so a collective-differential control scheme arose. If both servos spooled out the top string, this was a collective input and would tend to roll the blade about the servo axis. If the LE spooled out the top string and the TE did the opposite, this was a differential input and would pitch the blade about its center. However, due to the small spool diameter, the angular resolution of the servos, and the sensitivity of the blade angle to the string length in this rigging configuration, this was not an effective means of targeting a prescribed blade angle of attack. It is still unclear how this tip angle impacts the true angle of attack of the blade surface. While the tip angle closely matches the blade angle right where the two meet, this angle washes out as the rigging lines move up the blade, eventually approaching zero. Any variations in the blade shape further complicate this relationship, and a translating balloon would modify this even more as the relative wind changes. Unrelated to the blade angle, it was still difficult to get the device started without tangling, making further testing tedious and ineffective. Finally, this testing was conducted without a blade attached to the strings. When a blade was added, the system behaved similarly to previous tests. The aerodynamic moments on the blade were simply overpowering the centripetal forces and dominating the blade's behavior.

4.2.2 Stability Properties

The fundamental assumption that an atmospheric gossamer blade could be designed to mimic a heliogyro blade proved to be incorrect. More than a dynamic stability problem, with blades attached, the comparatively massive aerodynamic forces and the moments they generate lead to issues of static stability. A new approach would be needed in order to achieve stable blades which could be useful for generating lift.

4.3 Impacts of Rigging Geometry

In the first two prototypes, the rigging arrangement led to an inherently unstable system. While the tip weights would swing out, any disturbance in the blade would cause the tip to lag the root. This would cause the blade to twist, angling itself into the flow. In doing so, the drag on the blade skyrockets, causing it to lag even more. This relationship can be seen in Fig. (4.6).

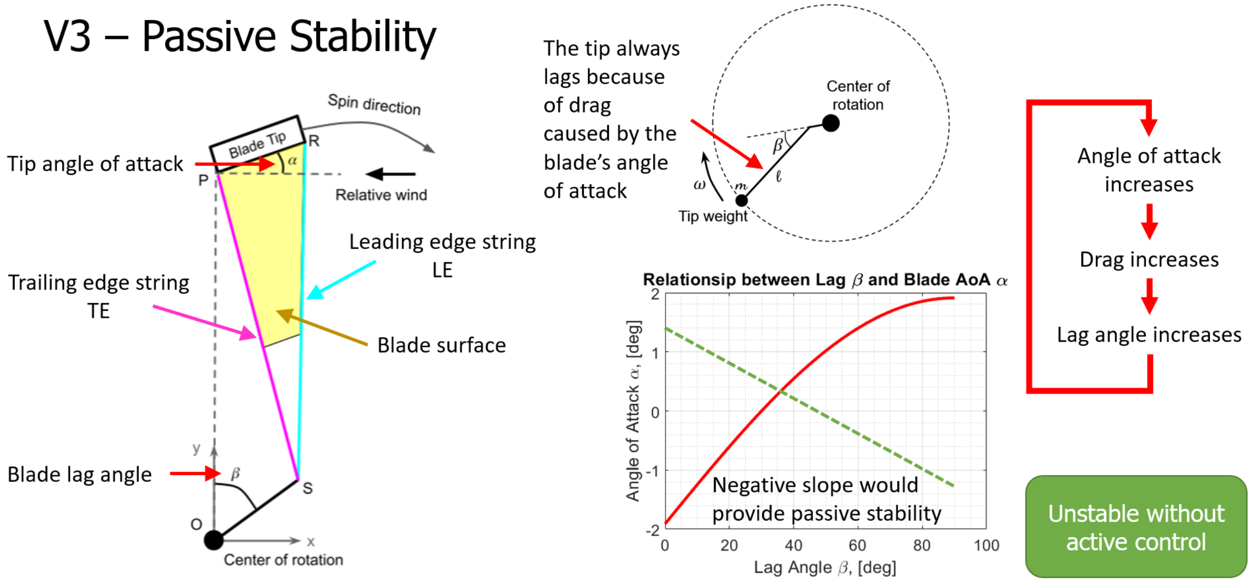

Figure 4.6: Top view schematic of the V2 rigging arrangement and its impact on the natural stability of the system. The relationship between lag angle β and tip angle of attack α is unstable.

4.3.1 4-Bar Linkage Concept and Stability Properties

While the tip controllers did work to damp this instability, a “4-bar linkage” concept was theorized to provide natural static stability from rigging geometry, eliminating the requirement for active control of the tips to maintain a constant angle of attack. This difference in rigging can be seen in Fig. (4.7), showing top views of simplified blades rigged in the previous triangular configuration vs a 4-bar link.

Seeking a relationship between the rigging geometry and the blade tip angle α, a series of "virtual triangles" are constructed interior to the 4-bar link for further analysis. Figure 4.8 shows the schematic and the three supporting virtual triangles.

From the first supporting triangle, we obtain length $\bar{OP}$ using Eq. (4.4):

$$\begin{aligned} OP &= \sqrt{\epsilon^2 + L_T^2 - 2\epsilon L_T \cos(180 - \beta - \delta)} \\ &= \sqrt{\epsilon^2 + L_T^2 + 2\epsilon L_T \cos(\beta + \delta)} \end{aligned} \tag{4.4}$$

From the second:

$$\begin{aligned} PQ &= \sqrt{d^2 + (OP)^2 - 2d(OP)\cos(\beta)} \\ d^2 &= (OP)^2 + (PQ)^2 - 2(OP)(PQ)\cos(\eta) \\ \cos(\eta) &= \frac{-d^2 + (OP)^2 + (PQ)^2}{2(OP)(PQ)} \end{aligned} \tag{4.5}$$

And from the third supporting triangle:

$$\begin{aligned} L_L^2 &= (PQ)^2 + c^2 - 2(PQ)c\cos(90 - \eta + \alpha) \\ &= (PQ)^2 + c^2 - 2(PQ)c\sin(\eta - \alpha) \\ \eta - \alpha &= \arcsin(\frac{-L_L^2 + (PQ)^2 + c^2}{2(PQ)c}) \end{aligned} \tag{4.6}$$

Solving Eq. 4.6 for α and substituting in the value of η from Eq. 4.5, we arrive at an equation for α purely in terms of the 4-bar linkage geometry.

$$\alpha = -\arcsin(\frac{-L_L^2 + (PQ)^2 + c^2}{2(PQ)c}) + \arccos(\frac{-d^2 + (OP)^2 + (PQ)^2}{2(OP)(PQ)}) \tag{4.7}$$

This can then be simulated to determine its stability properties. As mentioned previously, the blade angle α was in a negative feedback loop with the lag angle. When the blade lag angle β increased in previous tests, α also increased (increasing drag and causing more lag). Figure 4.9 shows that with a 4-bar linkage, α tends to decrease as β increases. This means that when the

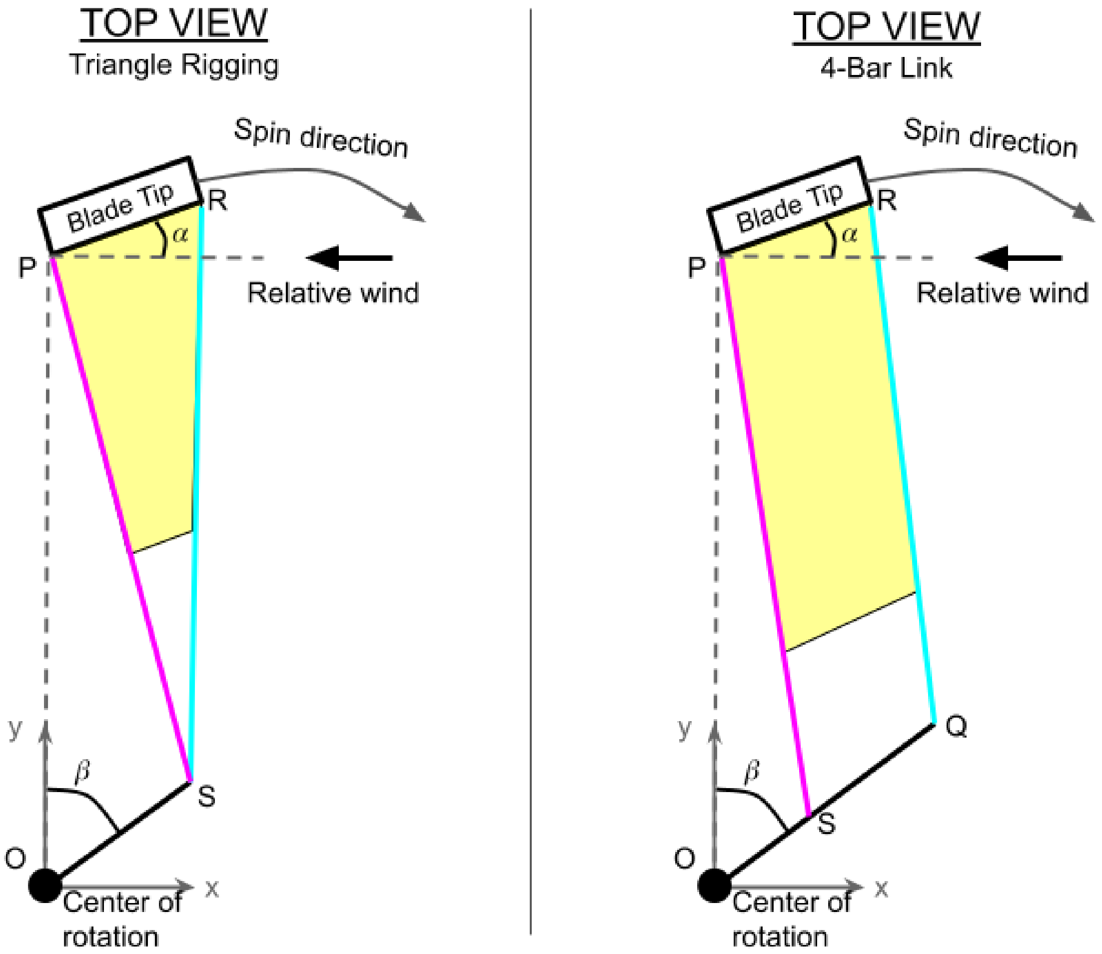

Figure 4.7: Comparison between the triangular rigging and 4-bar link.

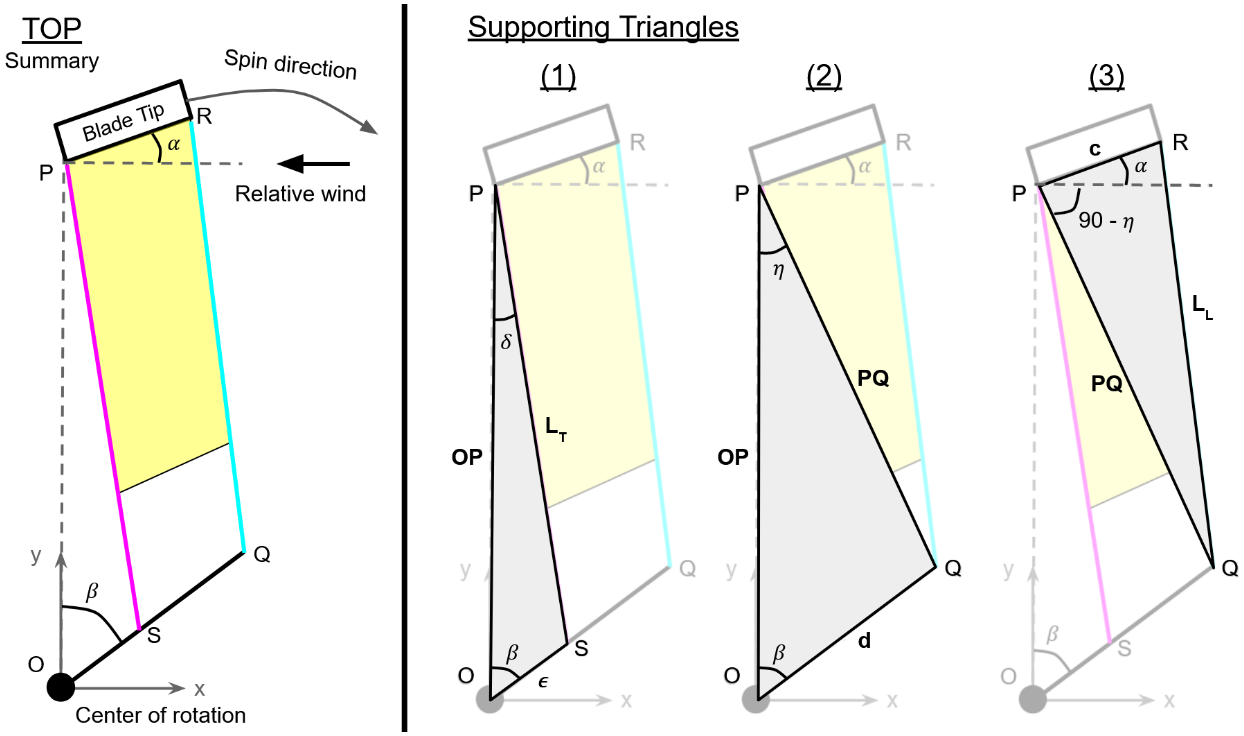

Figure 4.8: Schematic and supporting triangles of the 4-bar linkage rigging geometry.

blade lags due to a sudden increase in drag, the blade's angle of attack is reduced, reducing lag and settling back to a nominal lag angle. Since drag is never zero, and the blade tips are not producing thrust, lag angles less than zero as defined in Fig. (4.6) where the blade tip travels in front of the radial out direction is not possible except for short time periods during dynamic modes which are not currently being studied.

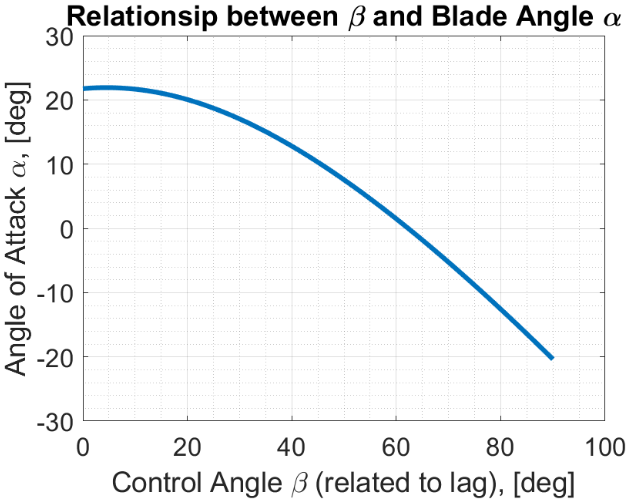

Figure 4.9: Relationship between β and α with a 4-bar linkage. $L_L = 2.93$ m, $L_T = 3$ m, $d = 0.2$ m, $\epsilon = 0.05$ m, $c = 0.2$ m.

4.3.2 V3: Natural Stability

With the analytical derivation promising positive results, a modified rigging arrangement was introduced to the existing test hardware that could validate those findings. Additionally, a deployment mechanism would be added in order to aid startup. These upgrades can be seen in Fig. 4.10 and were completed by May 2022. These tests seemed to validate the derivation that static stability is possible with geometry alone. The tip controllers were entirely disabled during these tests and the blade's response to perturbations was noticeably better than even its response under active damping. Another interesting result from this test was the realization that the blade surface takes a billowed form more like a sail or scoop than a flat plate, as seen in Fig. 4.11.

In order to directly control the angle of attack, actuators need to adjust the lengths of the

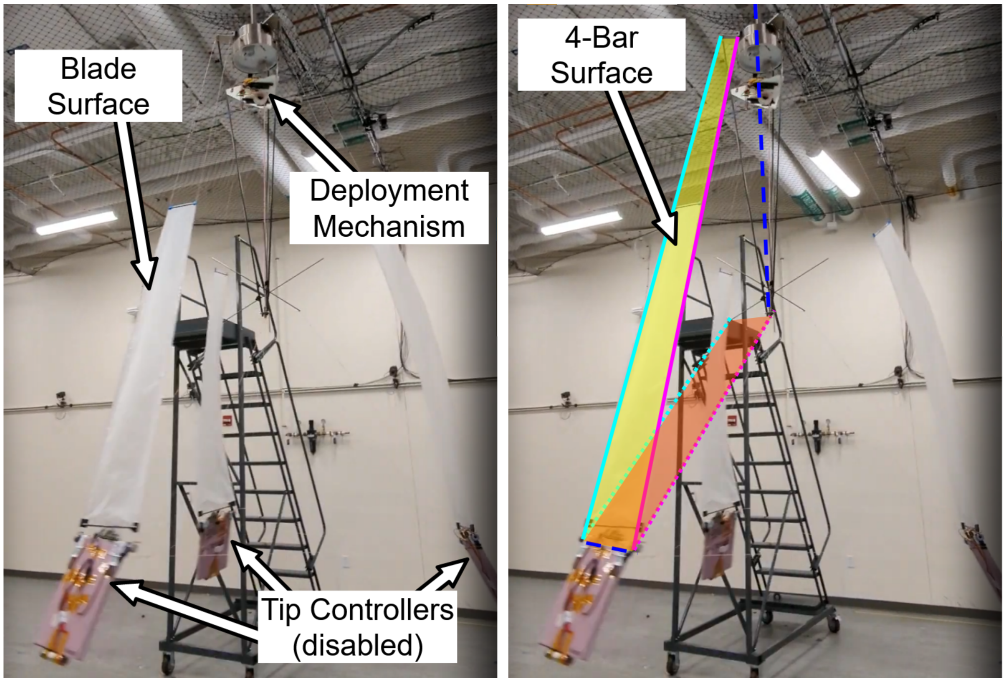

Figure 4.10: Description of the V3 prototype and visualization of the upper (yellow) and lower (orange) 4-bar linkage surfaces. LE (cyan), TE (magenta), Top rigging (solid), Bottom (dashed), with reference axes (blue dash). Note the offset between attachments points to the fan on the top and bottom.

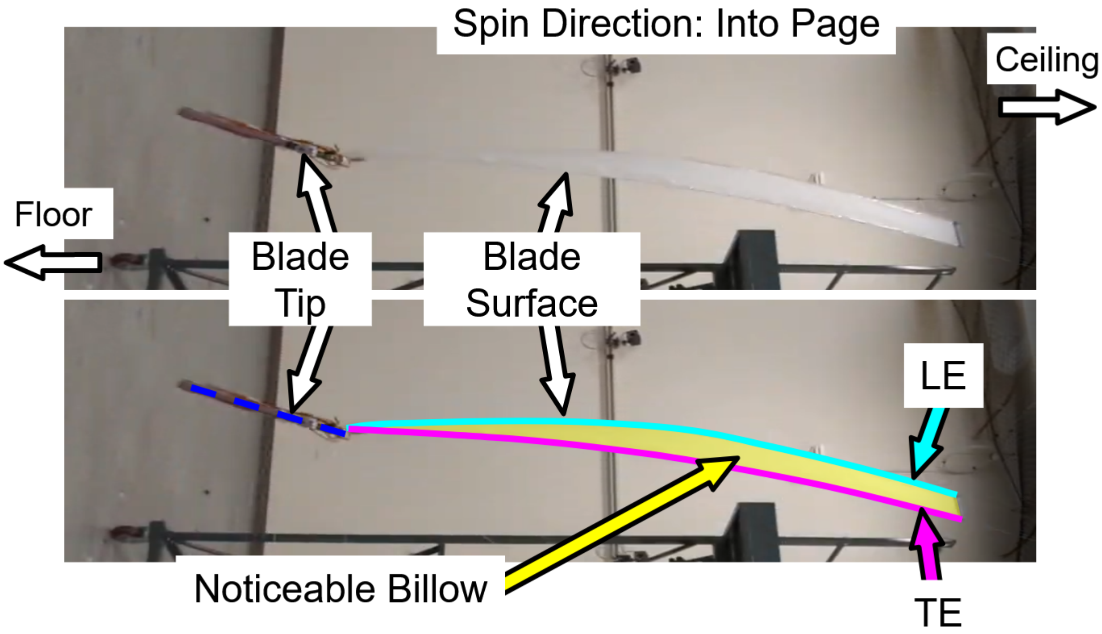

Figure 4.11: Visualization of blade billow with emphasis (bottom) of rigging and blade surface.

leading and trailing edges of the blade. It can be easily seen in both Eq. (4.7) and Fig. 4.8 that reducing the length of the leading edge (cyan) results in a reduction of the blade angle α. This was verified with testing by manually adjusting the string lengths between tests, but a more accurate, repeatable, and scalable option was sought for the next test version.

4.4 Beyond Stability: Controlling Lift

After completion of Version 3 testing, work began on another ground-up redesign with 3 major considerations in mind:

(1) A need for increased angular resolution of the string deployment servos, and the ability to store a longer length of string during the deployment process. This would allow for more precise control of string length and blade angle of attack while allowing test conductors to spin up the device to greater speed without tangling.

(2) A requirement for real-time string length adjustment during a test (rather than needing to stop the fan to adjust strings by hand). In addition to enabling the possibility of trimming each blade's angle of attack, this could allow for prescribed angles of attack to be reached.

(3) Previous tests were evaluated qualitatively using video recordings, making true comparisons between subsequent tests difficult. Instead, quantitative data needed to be collected and processed so that more specific conclusions could be drawn about blade performance.

Design modifications would also need to positively impact the scalability of the system. For example, while the Vicon system in the ASPEN lab could be used to collect data on the blades, such a system would not be viable for larger prototypes (that might be tested outside) or on a full scale lift augmented balloon. It would also require significant development towards new data processing and analysis codes.

4.4.1 Deployment Resolution

In order to get better resolution from the servos, a gear reduction system was designed. This was advantageous over purchasing new, higher quality servos since a full scale lift augmentation device is not necessarily intended to be recovered. Modification of the servos was necessary to enable continuous rotation, and flight software had to be rewritten to account for this. Further, as the final 10:1 gear reduction required significantly more space than was available on the blade tips, the entire line length control system was relocated to the gondola. Doing so also enabled a reduction in overall system complexity from an electronics point of view, as now a single microcontroller could monitor and manage all three blades rather than 3 separate microcontrollers each monitoring their own blade. Additionally, these larger spools enabled a 10x increase in stored string, allowing the device to deploy blades up to 5 m long.

4.4.2 Real Time Commands

While the previous line deployment mechanism was controlled remotely with a hobby RC controller, coordination of all 6 servos manually would be difficult. Instead, a remote ground station which could communicate to the lift augmentation gondola was designed and consisted of a low power radio module (whose pair was on the gondola), an Arduino for interfacing with the radio, and a MATLAB GUI for ease of use. An operator could select which blade (or groups of blades) needed adjustment, then could individually control differential and collective inputs to that blade (or group). This enabled real-time commanding of the blade angle as well as the ability to trim the blades individually without needing to stop the device. This also allowed for telemetered data from the gondola that could be analyzed after tests.

4.4.3 Device Telemetry

That telemetered data consisted of blade positions in 2D space measured by optical tracking cameras mounted to the gondola itself. Three OpenMV Cam H7s were mounted with their field of view pointing down and out towards the blade tips, now fitted with a 635 nm red LED. The cameras were also fitted with an inexpensive bandpass filter (bandwidth: 110 nm, center: 659 nm). In conjunction with software filtering that was implemented on-camera, the position of the tracking LED could be determined within the frame using a blob detection algorithm. This pixel location was sent to the gondola microcontroller for forwarding to the ground station.

4.4.4 V4: Angle of Attack Control

An updated design schematic of the new V4 test rig is available in Fig. 4.12 and a compilation of the prototype throughout the process can be seen in Fig. 4.13. Overall, the new mechanism weighs approximately 1.67 kg (3.68 lbs), as broken down in Tbl. 4.1. While mass efficiency was considered for the prototype, it was not a focus. Many parts can be further lightweighted, specifically the servo spools, the blade tips, and the support structure itself. It is anticipated that the overall mass of a full scale lift augmentation device could be as little as 1 kg.

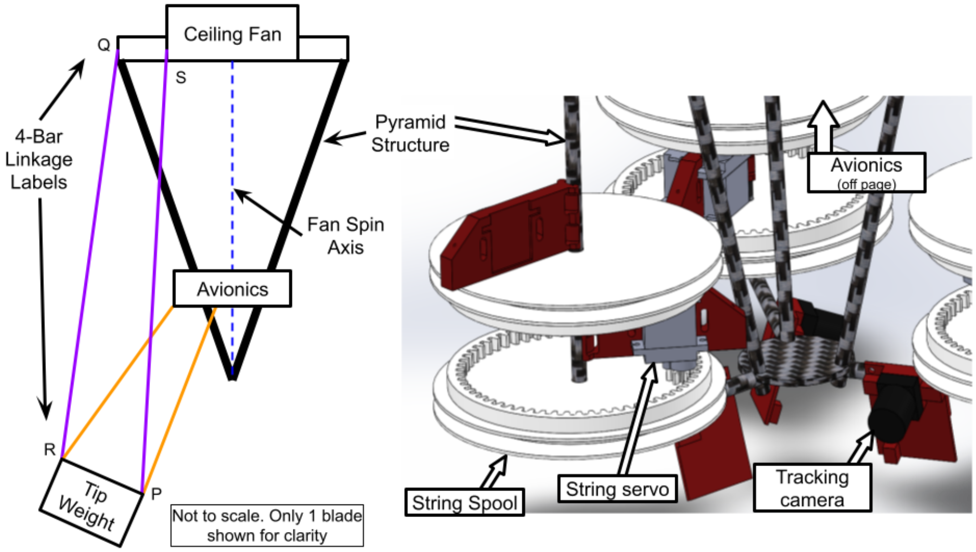

Figure 4.12: Schematic showing the major components of the V4 lift augmentation prototype. Note the changes from Fig. 4.3, namely the relocation and addition of a large amount of avionics.

Data from one of the onboard tip tracking cameras is shown in Fig. (4.14). We can clearly see the spin-up period for the first approximately 50 seconds of the test (initial deployment where no blade was in frame is truncated). Once the blade settles out, the lead/lag of the tip is approximately

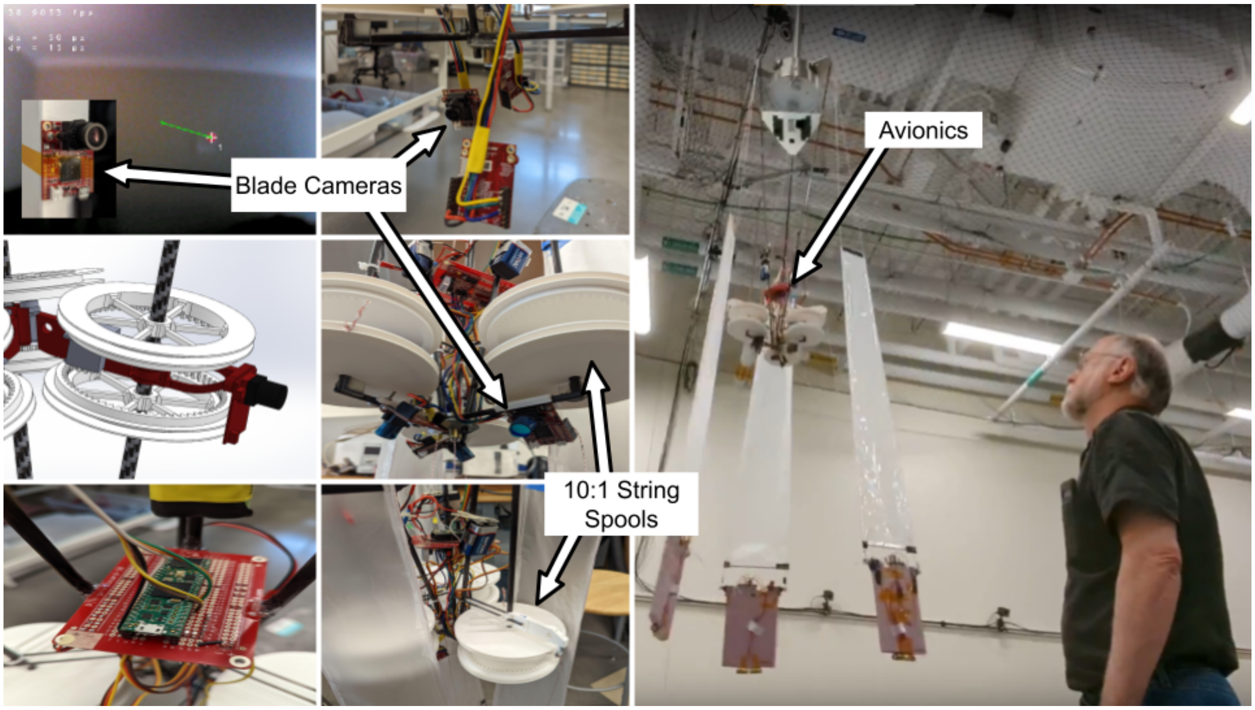

Figure 4.13: Compilation of the V4 design process. From top to bottom, left: Sample image of blob detection tracking a red LED; Initial CAD model for 10:1 spool reduction and camera mount; Main gondola board with Teensy microcontroller on top. Upper wires go to the radio, power converters and servos are on the bottom; Center: Cameras wired in and ready to be mounted to their new position; Bottom view of the completed device with cameras mounted and filters attached; Top view of the completed device with on-board power and 10:1 reduction spools (servos mounted internally to spools); Far right: Full V4 prototype hanging in the ASPEN Lab ready for testing.

Table 4.1: Mass budget of the V4 prototype.

Subsystem	**Mass [g]**
Structure	168
Blades	84
Tip weight	645
Servo spool assembly	522
Control avionics	40
Power	117
Tracking cameras	60
TOTAL	1,636

15 pixels wide, corresponding to a blade tip translation of approximately 18 cm. Tip flap is almost nonexistent with the sharp steps in the flap at 180 sec and 325 sec due to fan speed increases during the test. Note that no changes in blade angle were prescribed during this test, nor were external perturbations intentionally applied.

Further analysis of subsequent V4 tests were not conducted systematically. Loose camera mounts, poor spin rate and string length data, and optical artifacts made comparisons between tests difficult. Instead, V4 served to demonstrate an entirely new test architecture, one which would be further iterated to provide valuable cross-test insights and to further establish the pace at which physical testing could lead to sweeping design improvements.

It became clear at this stage that the test rig concept was valuable as more than just a way to test gossamer blades for scientific balloons. Rather, with some refinements, it could serve as a test platform for additional, more detailed studies of the aerodynamic behaviors of flexible blade sections.

4.5 Blade Performance

4.5.1 Remotely Measuring Lift and Drag

In order to quantify the aerodynamic performance of a blade, measurements of the lift and drag on the test section must be made. While traditional, rigid airfoils can be assessed by directly measuring these forces, such a measurement on a flexible blade is not possible. Interacting with the blade in any way results in modified behavior. Instead, a remote measuring technique is needed.

4.5.1.1 The Catenary Curve

The catenary curve is unique in that while it looks very similar to a parabola, its shape is actually that of an ideal chain or cable hanging under the uniform load of gravity, which is slightly different than a parabola [20]. The equation for a catenary centered about its lowest point is given in Eq. (4.8).

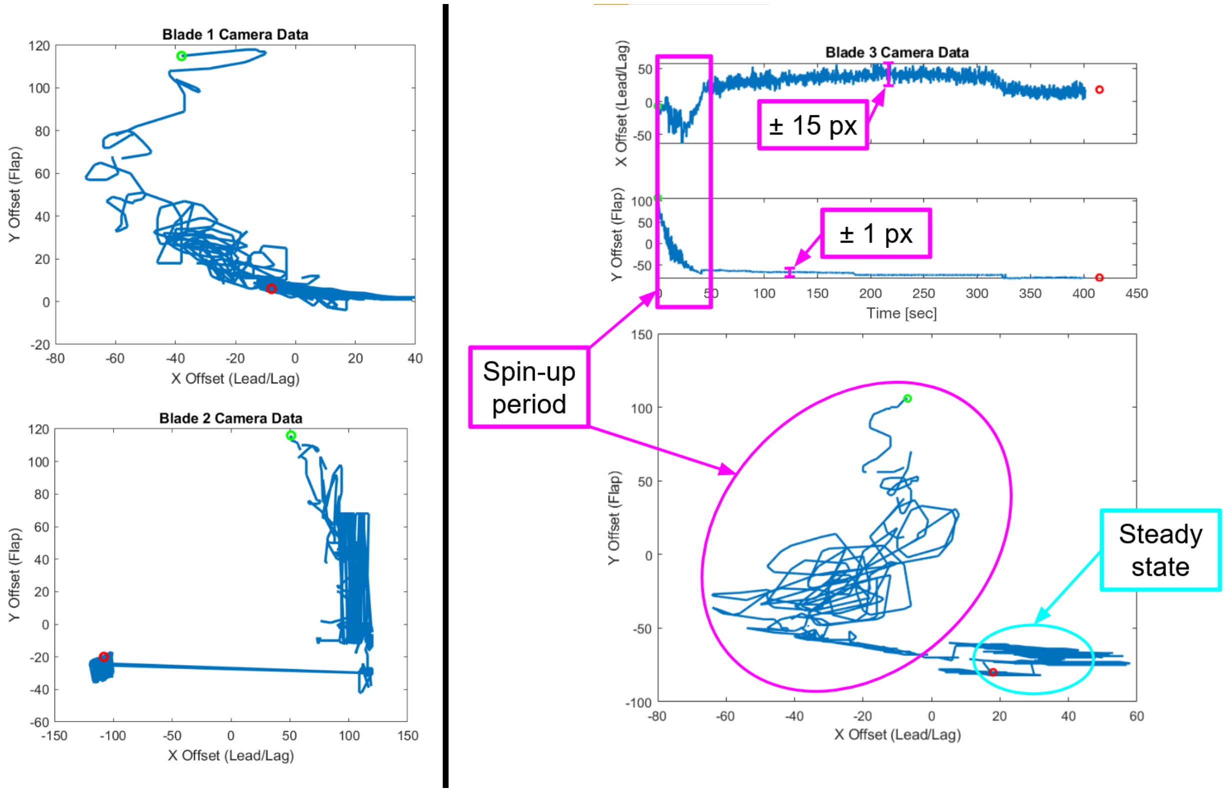

Figure 4.14: Camera data from all 3 blade tip tracking cameras from a test conducted on June 28th, 2022.

$$y = a\cosh\left(\frac{x}{a}\right) - a \tag{4.8}$$

While catenaries present themselves naturally when under a uniform gravitational load, in general, a catenary shape will be formed under any load which is uniformly distributed across a 1D line. When considered this way, the catenary parameter has a special relationship with the tension in the cable T_0 and the uniform load L, described in Eq. (4.9).

$$a = \frac{T_0}{L} \tag{4.9}$$

This concept enables the measurement of forces via geometry, as the impact of the uniform load is transferred into the cable through changes in tension, changing its shape.

4.5.1.2 Derivation of Forces from Tip Position

Two possibilities for collecting remote measurements have been explored, both relying on solving a force balance problem balancing the blade's centripetal and gravity forces against the tension forces in the strings. The behavior of these strings relates to the lift and drag of the blade section. Figure (4.15) shows the force balance diagram for solving the lift force, and Fig. (4.16) shows the drag.

Referring to Fig. (4.15), the tension in the blade (orange, indicated by T_u for upper tension), and consequently, the upper string, pulls the tip upwards under lift. We construct a virtual string (brown) that connects the tip position given the influence of the lifting blade to the top of the test rig, which has tension T_v indicating it is a virtual tension. The lower string also influences the position of the tip, pulling on it with T_l. As a result of the circular motion of the test rig and gravity, the tip experiences two additional forces in red.

The angle between T_u and T_v is determined by the shape of the blade and denoted as γ. The component of T_u which is orthogonal to the tension in the virtual string is a result of the accumulation of lift along the blade section, called $\tilde{L}$ to differentiate it from the true lift distributed

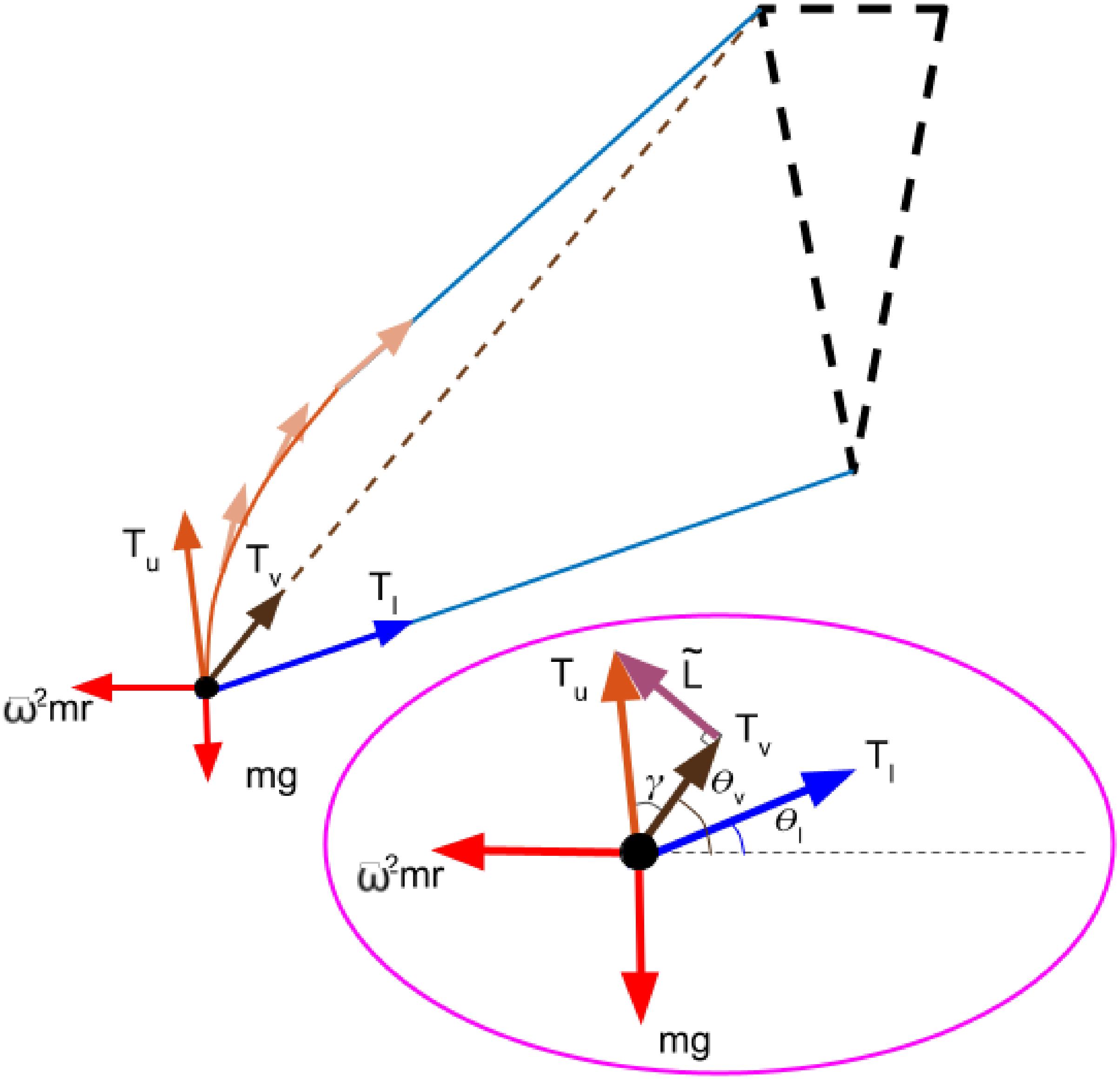

Figure 4.15: Free body diagram showing how to compute the lift of the blade

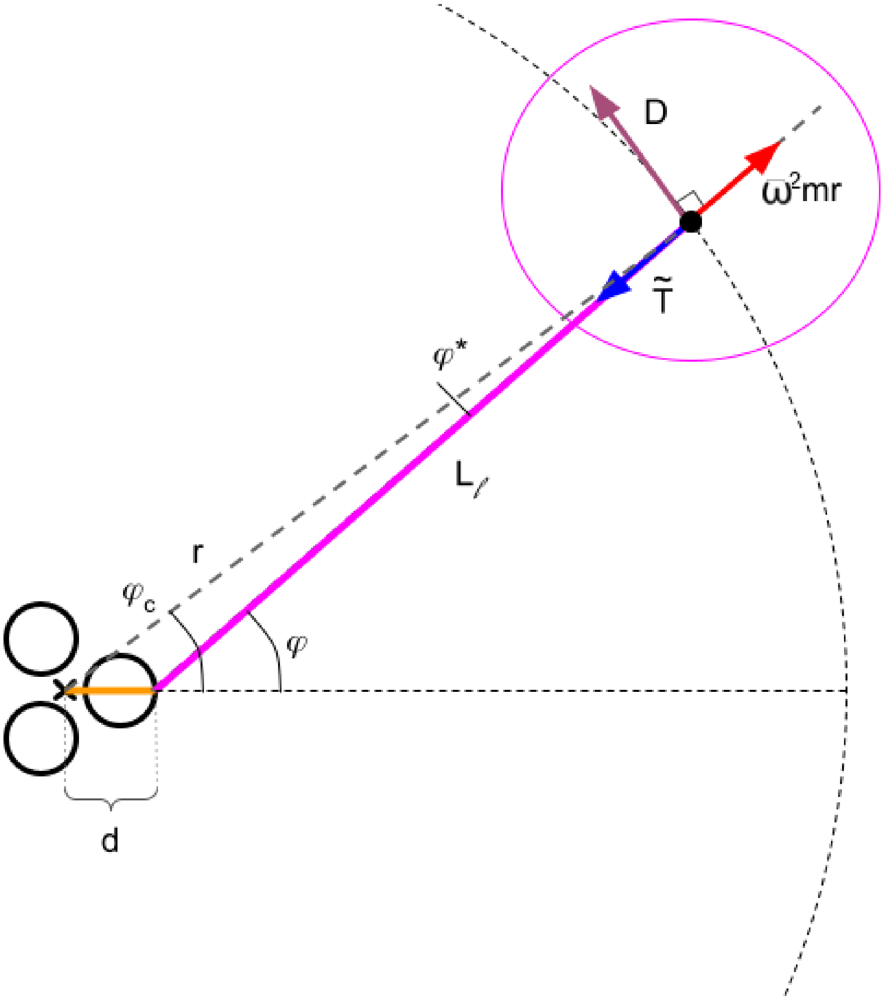

Figure 4.16: Free body diagram showing how to compute the drag of the blade

along the entire blade. We must solve this force balance to find T_u and T_l, then knowing γ we can compute the tip lift with Eq. (4.10).

$$\tilde{L} = T_u \sin(\gamma) \tag{4.10}$$

As the problem has been collapsed into 2 dimensions to solve just the lift, taking a span-wise slice of the blade, there are two equations associated with the force balance described in Eq. (4.11), with θ denoting the coning angles associated with each string:

$$\begin{aligned} T_l \cos(\theta_l) + T_u \cos(\theta_v + \gamma) &= \omega^2 mr \\ T_l \sin(\theta_l) + T_u \sin(\theta_v + \gamma) &= mg \end{aligned} \tag{4.11}$$

From the first balance equation, solve for T_l:

$$T_l = \frac{\omega^2 mr - T_u \cos(\theta_v + \gamma)}{\cos(\theta_l)} \tag{4.12}$$

Which can then be substituted into the second balance equation to solve for T_u:

$$\begin{aligned} \left(\frac{\omega^2 mr - T_u \cos(\theta_v + \gamma)}{\cos(\theta_l)}\right) \sin(\theta_l) + T_u \sin(\theta_v + \gamma) &= mg \\ \omega^2 mr \tan(\theta_l) - T_u \cos(\theta_v + \gamma) \tan(\theta_l) + T_u \sin(\theta_v + \gamma) &= mg \\ T_u(-\cos(\theta_v + \gamma)\tan(\theta_l) + \sin(\theta_v + \gamma)) &= mg - \omega^2 mr \tan(\theta_l) \\ T_u &= \frac{mg - \omega^2 mr \tan(\theta_l)}{-\cos(\theta_v + \gamma)\tan(\theta_l) + \sin(\theta_v + \gamma)} \end{aligned} \tag{4.13}$$

The drag can also be calculated by taking a different 2D slice of the full system, this time looking from above as seen in Fig. (4.16). Once again, two equations govern the motion of the tip, Eq. (4.14):

$$\begin{aligned} \tilde{T} \sin(\varphi^*) &= D \\ \tilde{T} \cos(\varphi^*) &= \omega^2 mr \end{aligned} \tag{4.14}$$

$\tilde{T}$ is used here because it is the string tension of the full 3D system projected into this 2D view. Since we know the distance d and r from the test rig and the position of the blade tip, as well as the length of the lower string L_l, we can again project that length into the 2D view to get $\tilde{l}$. This sets up a SAS triangle to solve for φ^*:

$$\cos(\varphi^*) = \frac{r^2 + \tilde{l}^2 - d^2}{2r\tilde{l}} \tag{4.15}$$

The equation for drag is then Eq. (4.16):

$$D = \omega^2 mr \tan(\varphi^*) \tag{4.16}$$

There are then two methods for obtaining the string angles θ_l, θ_v, and θ_u: The first method, called tip tracking, relies on being able to precisely identify the tip of the blade. This was accomplished with red marker LEDs and a camera system sensitive to the wavelength of those markers. The marker position in the camera frame can then be transformed into a global frame, given that camera lens intrinsics and a precise distance to the tip are known. This technique is visualized in Fig. (4.17). Stereo cameras could also be used, relaxing the assumption of a known string length. This method of tip positioning allows for blades of arbitrary geometry and arbitrary lift distributions to be used, as no assumptions are made regarding the shape of the blade during the test. This does introduce some bias in the measurement, however, as in these tests the marker LED is placed on a rigid extension from the gossamer wing surface.

The second method instead uses a known blade shape and upper string length to solve the string angles, rather than tracking the position of the tip directly. A depth camera is used to measure the shape and position of the blade throughout the test. Then, the depth data is transformed into 3D space much like with the tip tracking technique. Instead, however, a curve is fit to the depth data to parameterize it and smooth out any depth noise. This process can be seen in Fig. (4.18).

The blade can then be positioned in space using known upper string and blade lengths and assuming the boundary between the top of the blade (its root) and the upper string is tangent.

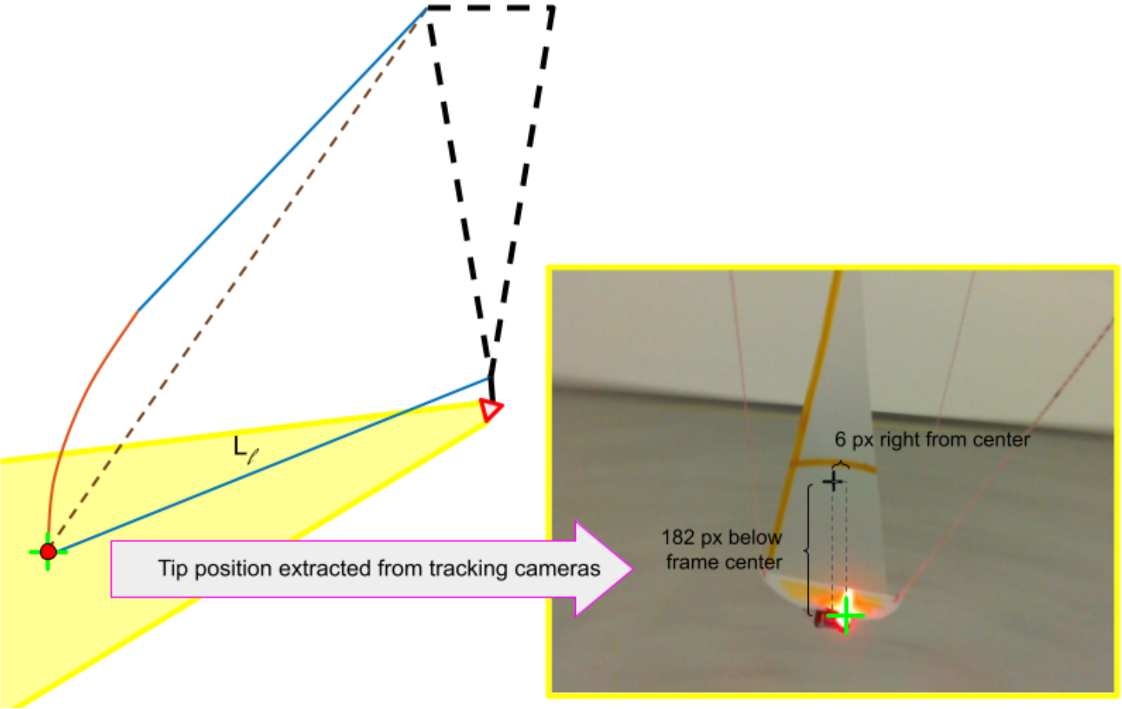

Figure 4.17: Schematic of the tip tracking measurement technique

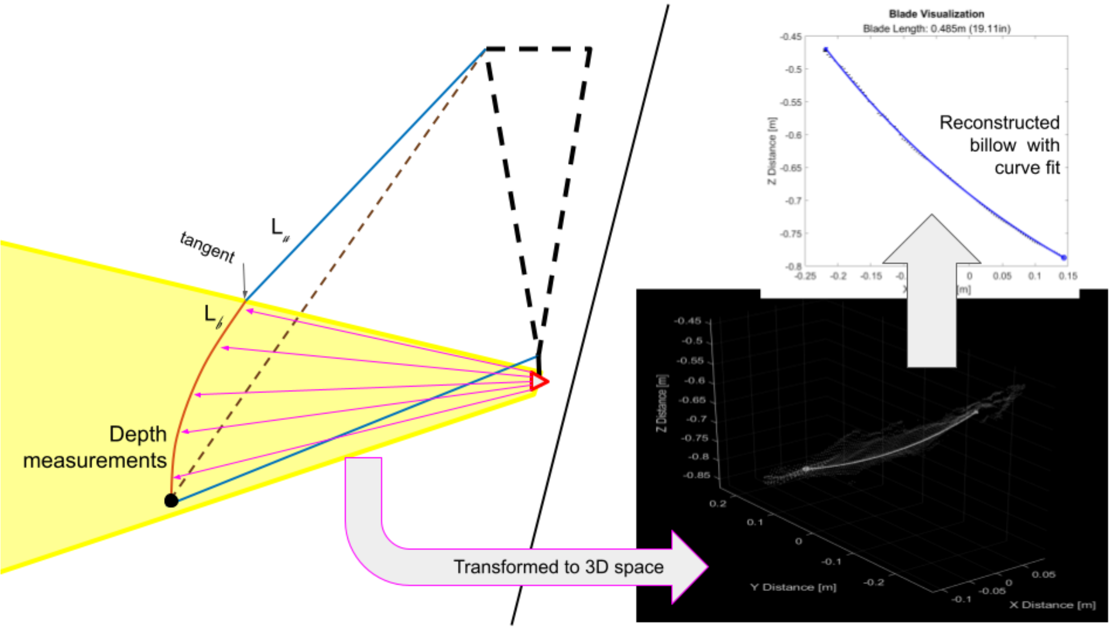

Figure 4.18: Schematic of the blade depth measurement technique

This is done by designating 3 frames of reference, as defined in Fig. (4.19).

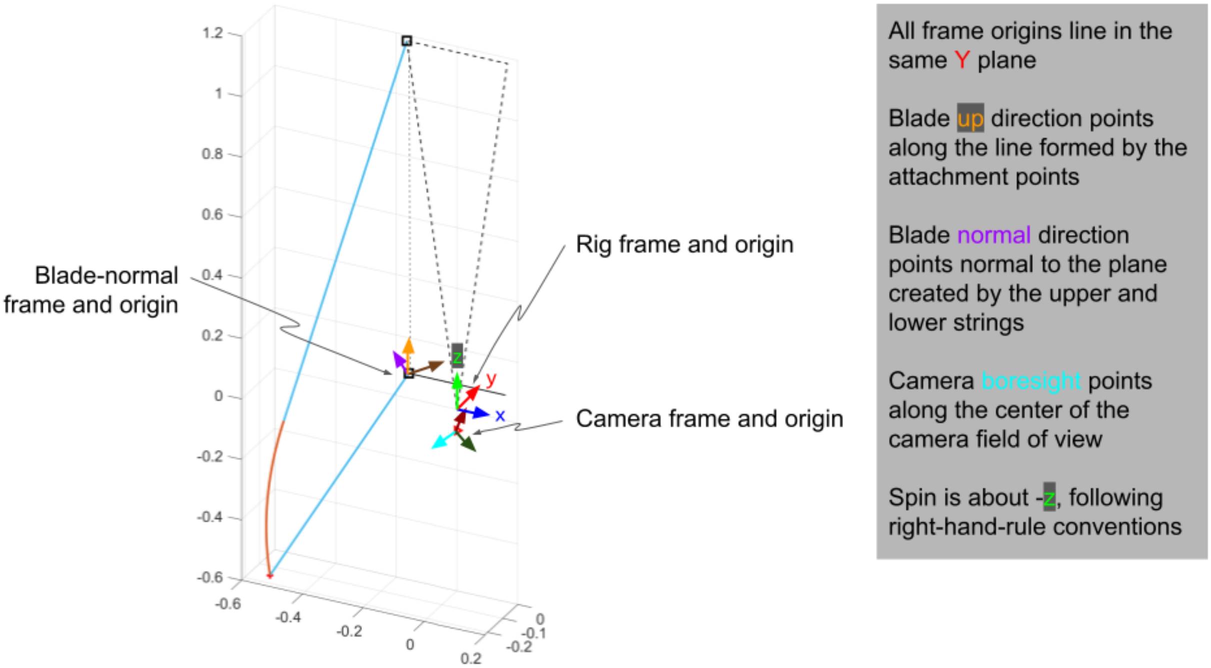

All frame origins line in the same Y plane

Blade up direction points along the line formed by the attachment points

Blade normal direction points normal to the plane created by the upper and lower strings

Camera boresight points along the center of the camera field of view

Spin is about -z, following right-hand-rule conventions

Figure 4.19: Diagram of the test rig with the 3 main frames of reference drawn.

The camera positioned at the center of the camera frame (and described in more detail in Sec. 4.5.2), observes the entire blade and using the Intel RealSense Viewer software, outputs a point cloud as well as raw RGB image frames. The point cloud is only used for fitting a parametric function to the billow data, and no transformations are conducted for depth data. Rather, to position the tip of the blade in the X-Z plane of the rig frame, a top string is generated which matches the measured length of the string used during the test. Parameters from the fitting routine then reconstruct the blade shape in the rig frame, constrained by the size of the actual blade from the test (measured manually). This reconstructed blade is then rotated about the Blade-Up axis as specified by a transformation of the lag data originating from the RGB images containing the tip marker LEDs. This produces a full digitized blade in rig space for further analysis in MATLAB.

4.5.2 V5: Development Test Rig

The final version of the test rig incorporated all the lessons learned from the prior versions with the goal of creating a more generalized test platform for characterizing not only gossamer blades for balloons but also other forms of flexible wings. It was also designed to be able to use both tip tracking and blade reconstruction for analysis. Four major improvements were made:

(1) Figure (4.20): Custom, purpose-built analog encoders were designed and integrated into the existing servo spools. Utilizing discrete phototransistors in quadrature and a tuned encoder pattern, angular displacements of the servo spool are resolvable down to 0.25 deg, corresponding to string length measurements of under 0.3 mm assuming the strings do not elongate under load. A PID controller is implemented on the Teensy microcontroller with a 0.75 deg deadband (limited by hobby-grade servo performance) corresponding to string length adjustments of 0.65 mm.

(2) Figure (4.21): The inclusion of a high-performance stereo depth camera enables the dual operating theories for deriving lift and drag as described in Sec. 4.5.1. This module also has an integrated RGB camera and an internal IMU. Controlled remotely via an SSH connection to an onboard Raspberry Pi, the camera saves ROS .bag files for further processing. This allows the use of Intel's data analysis tools, or in the future, custom-designed data processors as part of a ROS framework to be utilized.

(3) Figure (4.22): In order to reduce the effects and influence of tip vortices, and to standardize the blade tips moving forward, tip extensions with an elliptical planform were cut from thin fiberglass sheet. The same marker LEDs from the V4 rig were affixed to the new blades, but with the reduction of other unused control electronics, each blade tip only weighs 104 g. This leaves a large margin for the addition of tip weight in the future, which may affect the sensitivity of measurements due to the coupling of tip position with the aerodynamic forces.

(4) Numerous smaller improvements were also made, including: the inclusion of a gyroscope providing live spin rate telemetry (which also provides redundancy in post-processing to the IMU within the RealSense camera); refactoring of the ground station control software enabling direct string length inputs; redundant telemetry data storage of both .csv and binary telemetry logs; microcontroller flight software updates enabling closed loop servo control in conjunction with the encoders; and power stability and thermal improvements.

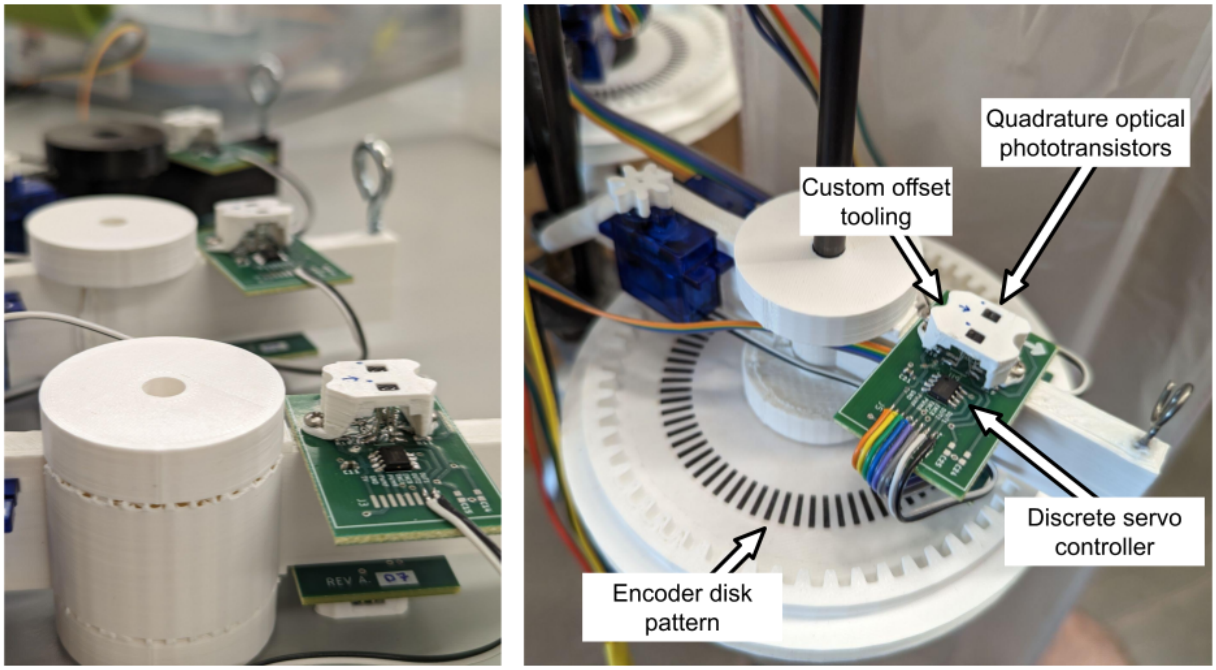

Figure 4.20: Custom designed PCB analog encoders for the V5 test rig.

4.5.2.1 Analog Encoders

With the string lengths needing to be known in order to accurately measure the position of the blades, a new method for measuring how much string has been released was needed. In the V4 rig, this could have been accomplished (but was never implemented) by keeping a running timer of how long the servos had been running. This limits the operation of the servos to a fixed speed, and given precise control of blade length is desired, a range of servo speeds are required. Additionally,

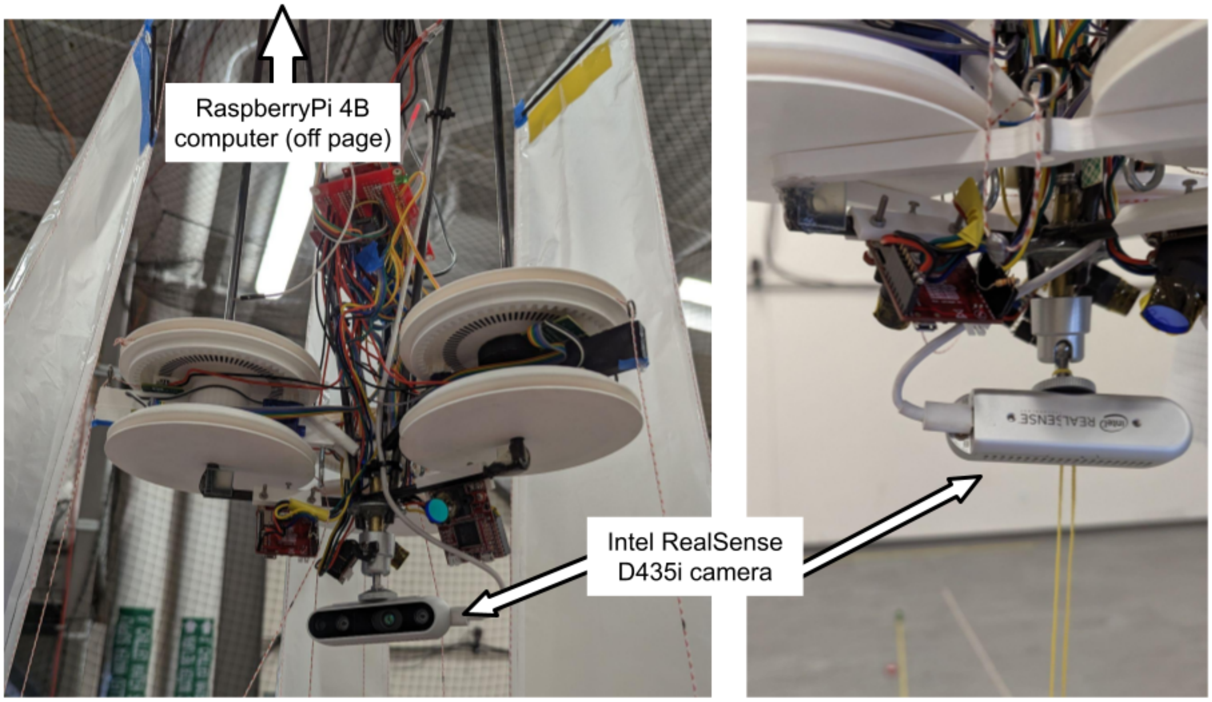

Figure 4.21: Intel RealSense camera mounted to the test rig. Control computer located on-board (out of frame) and accessed remotely via SSH during a test.

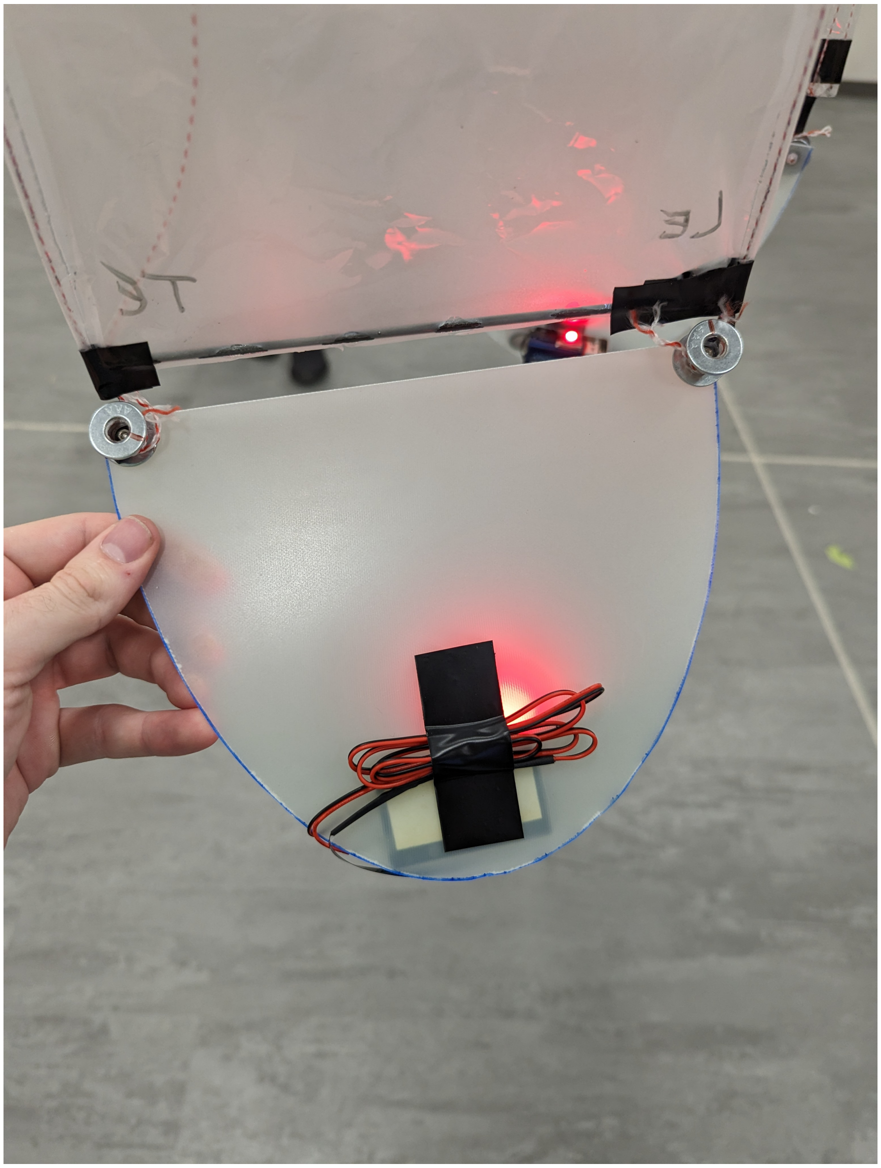

Figure 4.22: Elliptical blade tips with marker LED and triangular blades attached.

variations in servo speed could not be accounted for, such as when the batteries were low and servo rotation speeds are reduced.

Another requirement was that the sensing method not interact with the spools directly, as this could interfere with the string tension calculations. An optical encoder would be needed to measure the spool position, which could be converted to a string length by spool geometry. A custom encoder was designed in order to fit the test rig without significant modification.

Typically, encoders operate on a digital signal which determines the position of a sensing disk. Commercial encoders can pack thousands of pulses in a single rotation, enabling sensing resolutions better than 1/5 of a degree per pulse. In a custom-designed encoder, however, achieving this level of precision would be difficult. Instead, an analog encoder could be designed which measures the voltage returned between the quadrature signals to achieve far finer resolutions than a digital encoder of the same pulse count. Figure (4.23) depicts this concept.

Using this method, a 75-pulse disk, which can be printed to standard printer paper and which would normally have a resolution of nearly 5^o per pulse, can achieve resolutions down to 0.25^o per pulse.

All processing for these encoders is implemented on a Teensy 4.1 microcontroller. On each mainline loop, the analog to digital converters connected to the phototransistor outputs are sampled and the angle between voltage measurements is calculated and converted to a physical rotation angle. The time between samples is faster than the Nyquist frequency of a single pulse under maximum servo rotation, ensuring pulses cannot be skipped or missed (which would bias the physical angle by multiples of 4.8 deg given the 75 pulse disk).

4.5.3 Test Results

Numerous tests were conducted in May and June 2023. First, 4-bar link stability and string length control was verified without blade sections (Figure (4.24) and subsequently, small square blade sections were attached as in Fig (4.25).

These tests also allowed the data processing pipeline to be trialed. Figure (4.26) shows one

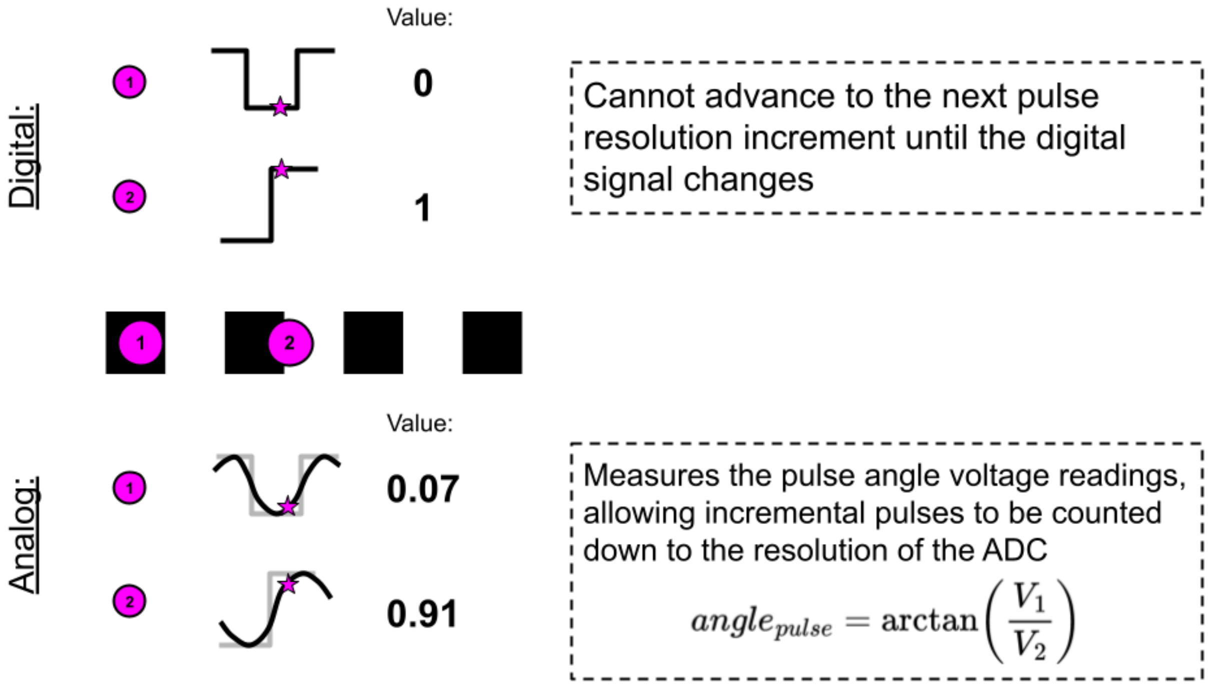

Cannot advance to the next pulse resolution increment until the digital signal changes

Measures the pulse angle voltage readings, allowing incremental pulses to be counted down to the resolution of the ADC

$$angle_{pulse} = \arctan\left(\frac{V_1}{V_2}\right)$$

Figure 4.23: Comparison of traditional digital encoders with that of an analog encoder. The magenta circles indicate the positions of the phototransistor sensing windows, with the resulting reading for each encoder type shown.

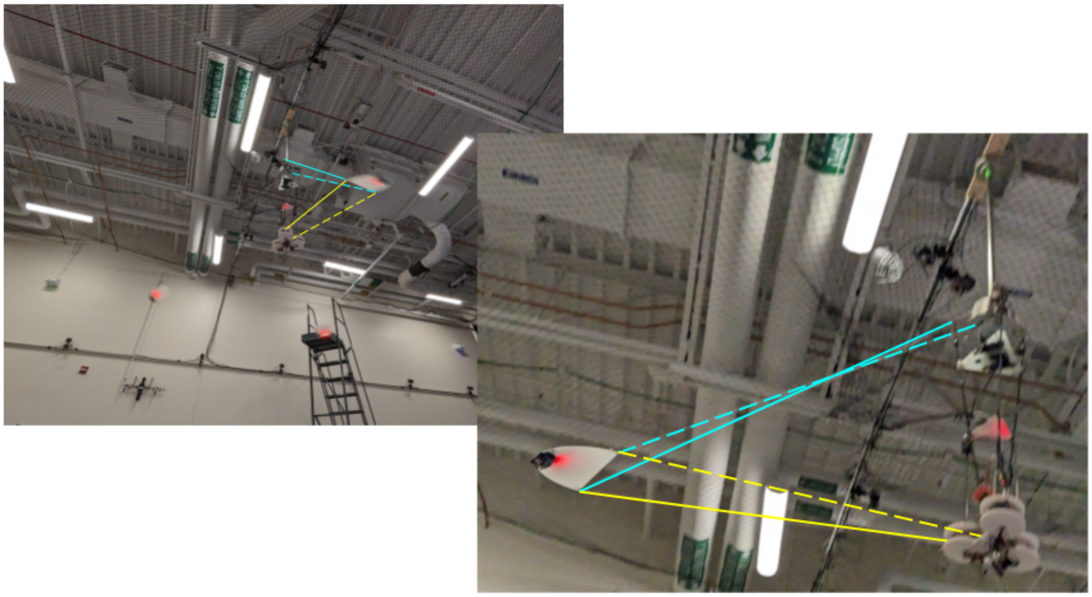

Figure 4.24: V5 test without blades attached (just tip boards and marker LEDs) with strings highlighted for one blade. Cyan: Upper strings; Yellow: Lower strings; Solid: Leading edges; Dashed: Trailing edges.

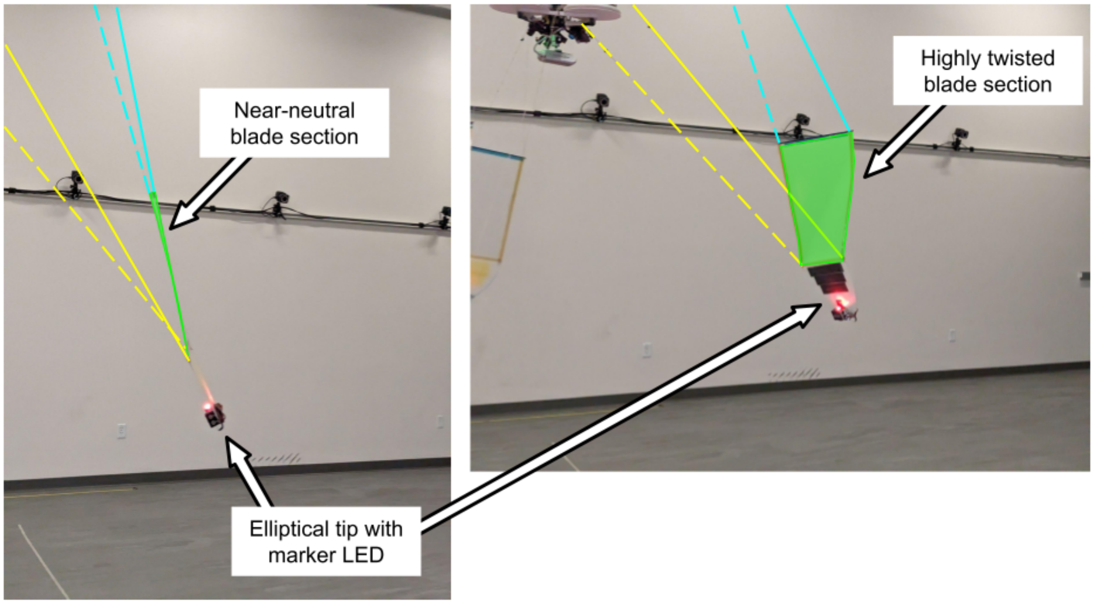

Figure 4.25: Testing with small square blade sections, highlighted in green. Left: Blade trimmed to near-neutral, exhibiting little twist. Right: Blade tip trimmed to large angle of attack, causing excessive blade section twist.

of the square blade sections as seen by the depth camera. Strings and the location of the test rig are approximated and added to the image for clarity. As you can see, the point cloud is reliably dense across the blade section and depth measurements down to 1 mm resolution are achievable.

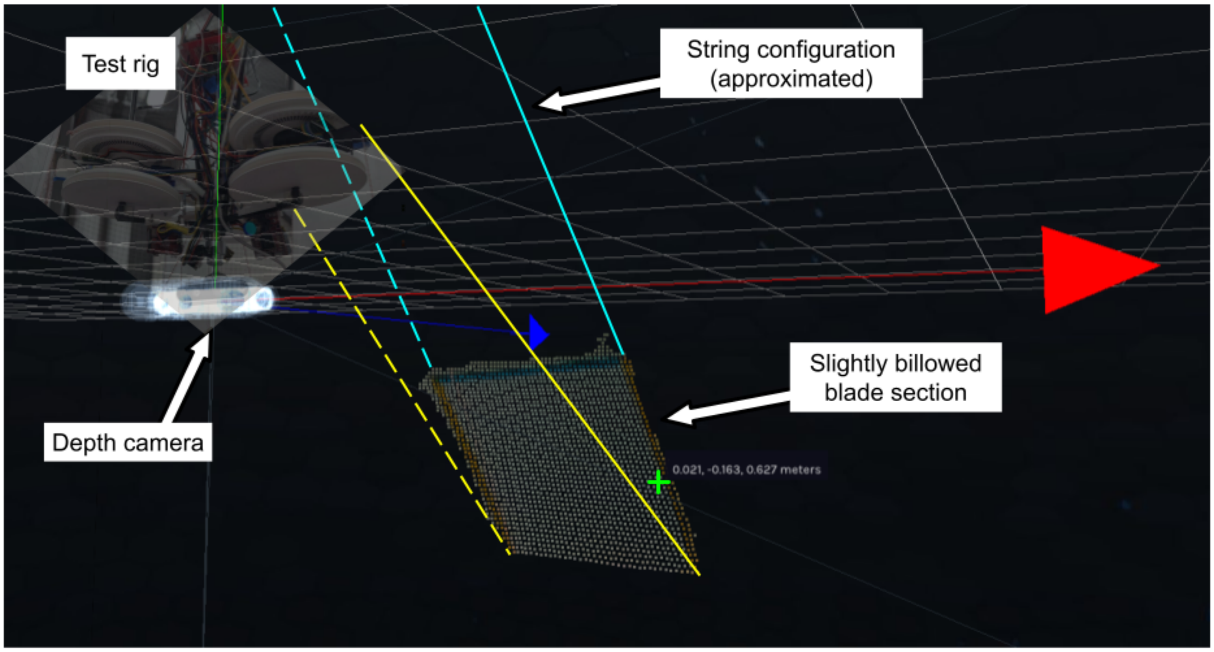

Figure 4.26: Blade section depth data visualized using the Intel RealSense Viewer software.

Ultimately a blade which exhibited a uniform lift distribution was desired. Additional justification for this will be provided in Sec. 4.5.5, but it was theorized that a triangular blade section, with a larger blade tip transitioning to a zero-length root, would better exhibit this uniform lift distribution. Such a blade was fitted and another test began. Since only a single depth camera was being used, meaning one could only collect data on a single blade at a time, the remaining blade sections were removed entirely to reduce the influence of prop wash or other blade effects on the test section of interest as seen in Fig. (4.27).

Multiple tests were conducted at two tip angles of attack: One where the blade section remained neutral and one where the blade section exhibited billow, generating lift. The difference in tip location for these two cases can be clearly seen in Fig. (4.28). With the blades spinning

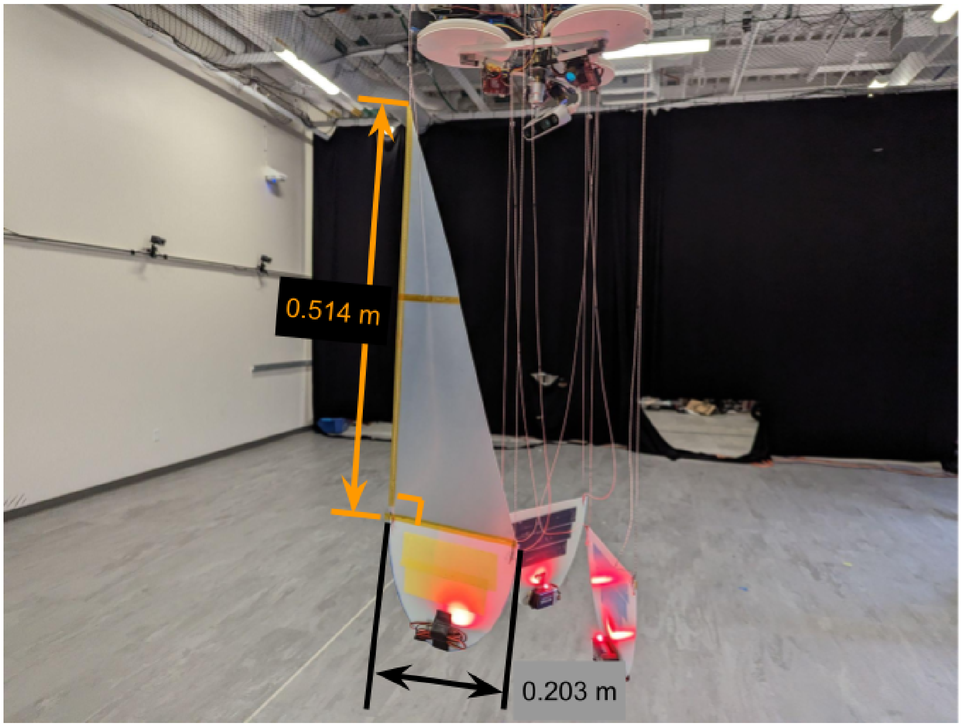

Figure 4.27: Triangular blade with other blade sections removed.

right to left, notice the reduced coning angle of the billowed blade (from the marker LED with a blue cross positioned higher than the neutral case) and increased lag angle (from the marker LED with a blue cross positioned further right than the neutral case). Looking at the depth data in Fig. (4.29), we can also clearly see a difference in the blade's billow, with the neutral blade exhibiting little to no noticeable billow and the billowed blade exhibiting a consistent billow across the test section.

4.5.4 Lift Distribution of the Billowed Blade

If the virtual cable drawn across the span of a billowed blade takes the form of a catenary, it could be reasonably assumed that the lift distribution across the blade was uniform, as a non-uniform lift would produce a different billowed shape. Then, if the tension in the strings were known, the catenary parameter a which best fit a catenary curve to the billowed depth data could be used to estimate the lift L across the blade.

Figure (4.29) shows the virtual cable in the magenta and green lines across the depth data, with catenary parameter a fitting to this data. In the billowed blade, the catenary fit has an a parameter of only 0.9588 and an R^2 value of 0.9975, indicating that a catenary curve is a very good fit for the depth data. Overall, the root mean squared error (RMSE) of this catenary fit was 1.7 mm. Compare this to the neutral case, with a much larger catenary parameter of 10.7061. While the RMSE of this fit is lower (1 mm), the R^2 value is also lower, 0.8806, suggesting that a catenary may not be the best-fit equation for the neutral case. Given we expect very little lift from a flat plate with no angle of attack, it makes sense that whatever shape the blade takes would not be catenary in form. The neutral blade is far better fit with a linear model, where depending on the selected virtual cable to fit, the R^2 value can easily get above 0.95.

With the shape of the blade now determined, we can take the approach described in Sec. 4.5.1 which takes advantage of a known blade shape. Using a measured blade leading edge length of 0.514 m and a known upper string length of 1.780 m for the leading edge, we can position the blade in 3D space and compute the lift and drag associated with the billowed test section. The

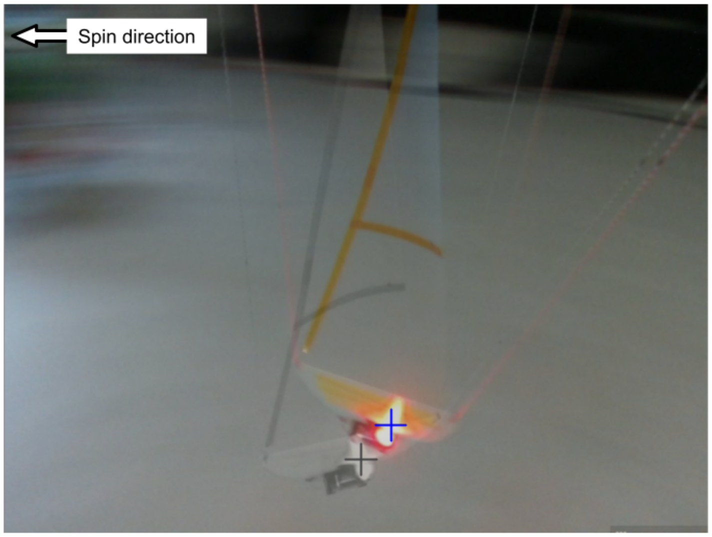

Figure 4.28: Tracked tip location difference from lift and drag. Grayscale image shows a neutral blade section, color image shows billowed section.

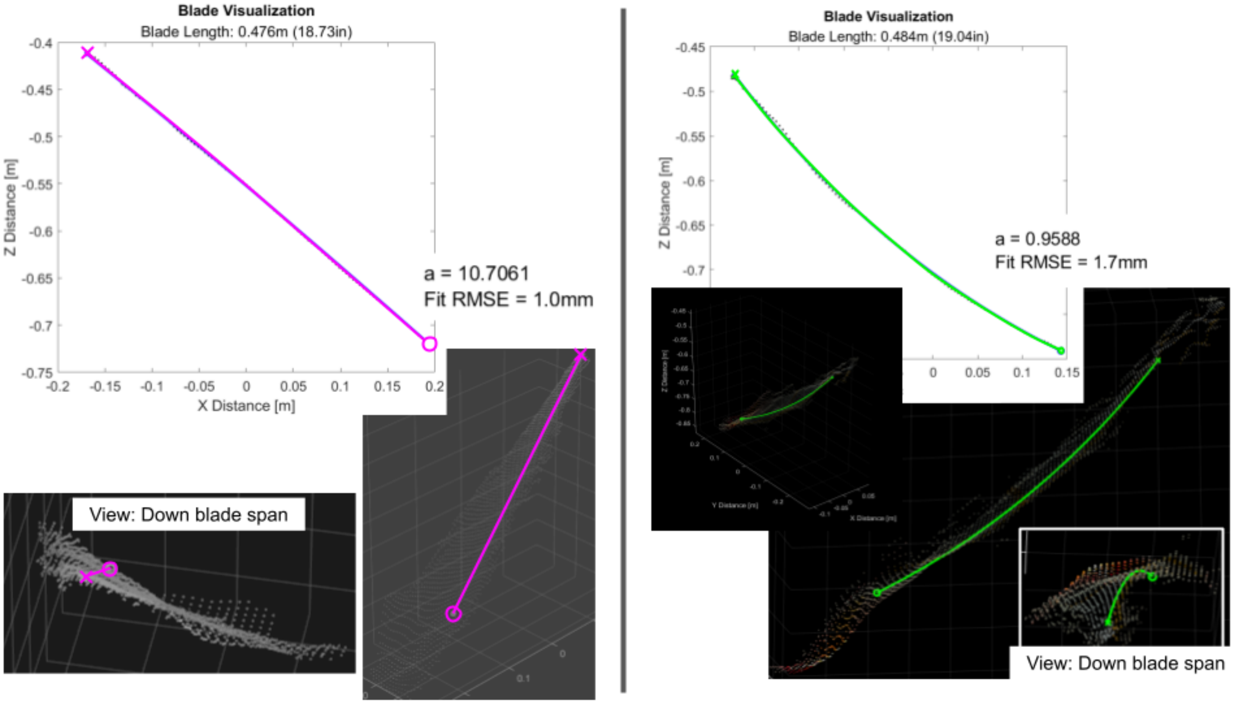

Figure 4.29: Comparison of neutral (left) and billowed (right) depth point cloud data and associated curve fit. The value a is the parameter of a catenary which fits the depth data.

results of this placement are shown in Fig. (4.30) and (4.31).

The measurement interval of 5 seconds covered approximately two full blade rotations and consisted of 34 frames of usable depth data. Using Eqs. (4.10)-(4.13), the average lift was calculated to be 0.0285 N. This value can be verified by using the upper string tension and the catenary parameter to back out the uniform force on the billowed blade, which was found to be 0.0293 N, a difference of only 0.8 mN, approximately 3%.

Drag was calculated using Eq. (4.16) and was determined to be 0.0865 N. Roughly 3x the lift force, this large drag is likely due to the increased "scooping" of the blade, particularly nearer the root of the blade section, resulting in extremely high angles of attack. Such extreme angles cause the blade to stall, resulting in much higher drag than anticipated.

The periodic oscillations result in variations in the lift and drag measurements. Figure (4.32) shows the 2σ bounds for the lag angle and blade billow given these oscillations during the measurement interval. Overall, the drag measurement varied by ±4 mN. Since the catenary curve has a nonlinear relationship between its shape and the lift force, the 2σ bounds for billow and lift are not centered around the mean, with the lower bound representing a lift of 0.0182 N and the upper bound a lift of 0.0567 N.

4.5.5 Theoretical Lift Results

In order to validate these experimental results, and to further justify the catenary fit assumption of a uniform lift distribution, a simple blade element theory model was constructed. Using the best estimates for the actual configuration and aerodynamic properties of the blade as tested (listed in Tbl. 4.2), the model predicts a total lift force of 0.028 N and remains within 20% of uniform across approximately 80% of the blade, only deviating at the blade root where the chord approaches zero. This fit area is shown in Fig. (4.33).

While the BET model only predicts moderate uniformity in lift distribution across the blade span with the non-zero root chord chosen to account for observations of non-zero lift at the blade root, the catenary fit to the depth data shows very good correlation with a catenary distribution,

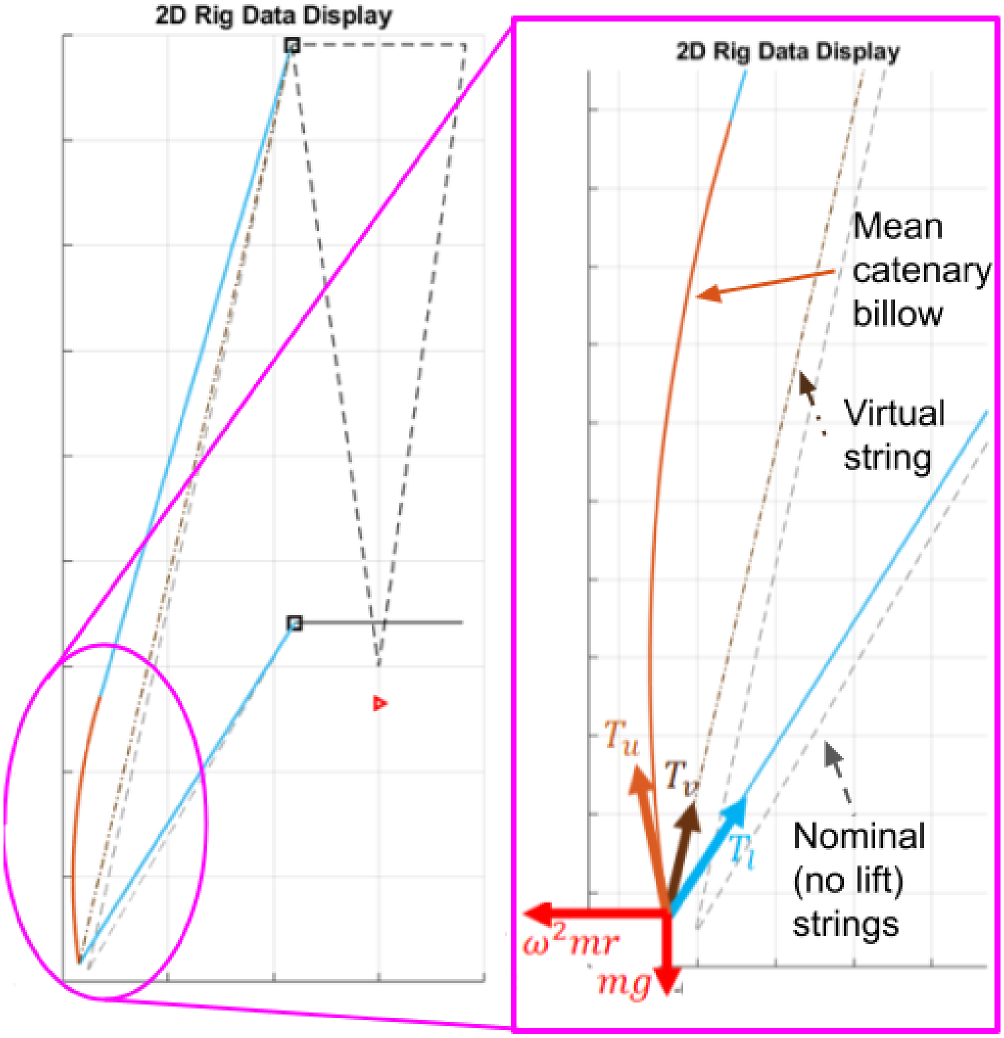

Figure 4.30: Billowed blade reconstructed into rig space for analysis of lift. Bold lines show the mean blade position and billow across a five second measurement interval. The brown line is the "virtual string" used for aerodynamic analysis, while the grey dashed lines indicate the neutral position of a non-lifting blade.

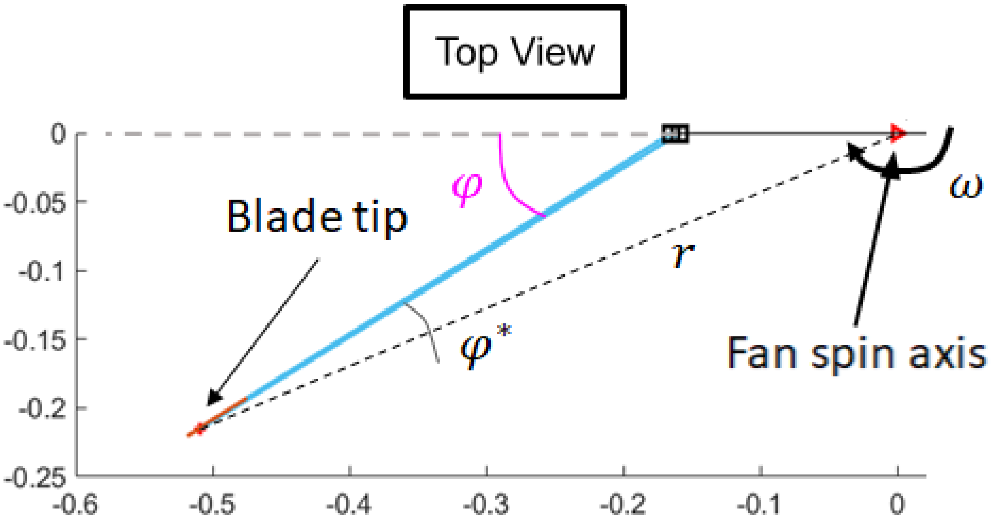

Figure 4.31: Blade reconstructed into rig space for drag analysis.

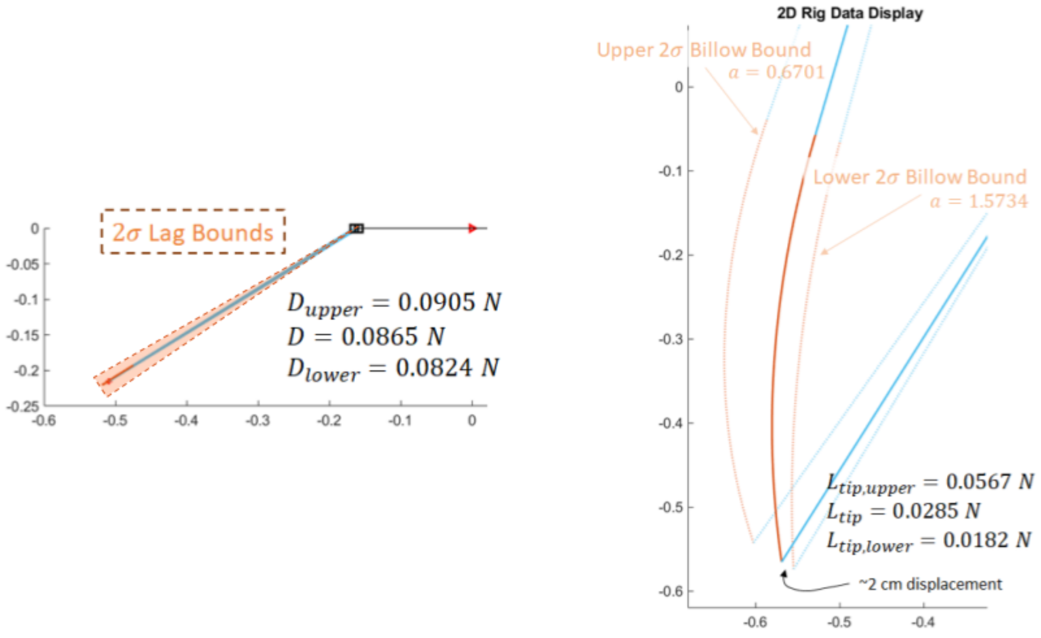

Figure 4.32: Variations of lift and drag due to oscillations during the test.

Table 4.2: Aerodynamic properties of the actual blade tested in the BET model.

Property	**Value**
Lift Coefficient	$2\pi\alpha + C_{l,0}$
Blade Span	0.3 m attached to a 1.3 m string
Coning Angle	77^o
Spin Rate	180 deg/sec
Tip $C_{l,0}$	0.1
Root $C_{l,0}$	0.5
Tip Chord	0.203 m
Root Chord	0.05 m*
Tip α	6^o
Root α	16^o

* Non-zero root chord is chosen to capture test observations which indicated non-zero lift at the root despite the chord going to zero, likely from 3D wing effects not captured in this BET model without providing a non-zero chord length.

suggesting that either 1) the actual lift distribution is more uniform than the BET model predicts due to aerodynamic effects not modeled in this simple implementation of BET; or 2) remaining within 20% of uniform across 80% of the blade produces a billow which appears catenary within the depth resolution of the camera.

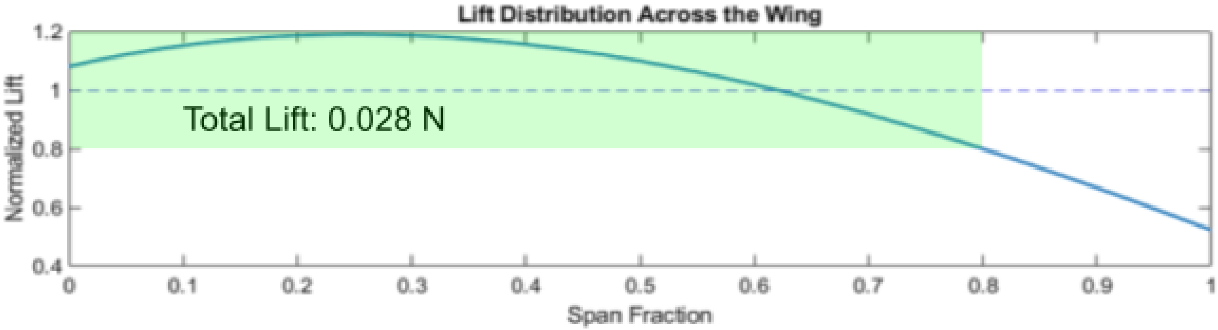

Figure 4.33: BET model results for the lift distribution of the actual blade section.

Future tests could aim to better analyze this discrepancy by designing a blade that exhibits better lift uniformity across a longer span. One such blade could have parameters similar to those described in Tbl. 4.3 and simulated in Fig. (4.34), where the blade remains within 20% of uniform for over 98% of the blade and within 10% of uniform across 80% of the span.

4.6 Model Discrepancies

Overall, comparing three different methods of computing the lift of the gossamer blade resulted in very similar results, summarized in Tbl. 4.4.

This represents model agreement within 3.3%, an impressive accuracy given the assumptions made to distill aerodynamic behaviors of flexible wing surfaces down to first principles equations. Specifically, ignoring tip effects and using a constant 2π lift curve slope from thin airfoil theory. Additionally, Eq. 4.13 applies the lift force at the tip only. Future model improvements could apply a lift distribution across the entire string section, or apply a single section lift at the wing's center of pressure.

The agreement in drag estimates to that of a lift-to-drag ratio of between 5:1 and 10:1 were not

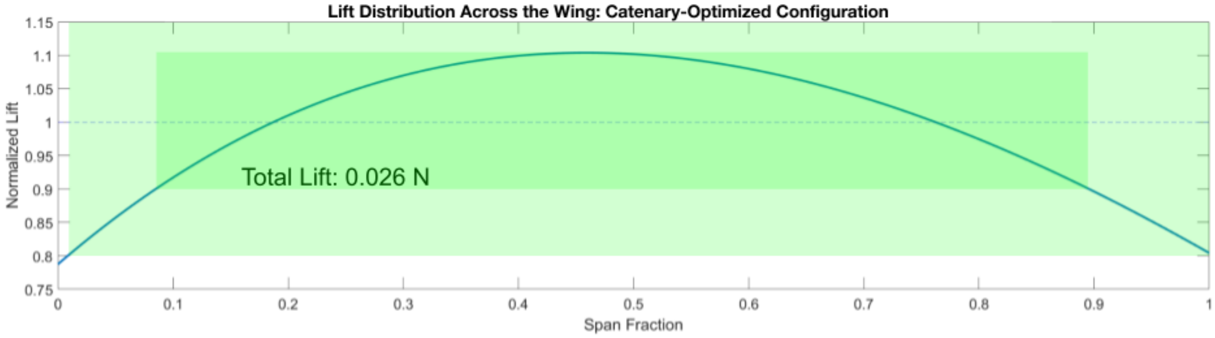

Figure 4.34: BET model results for a first pass of a catenary-optimized blade section.

Table 4.3: Aerodynamic properties of the V1 catenary-optimized blade which produces near-uniform lift across its span.

Property	**Value**
Lift Coefficient	$2\pi\alpha + C_{l,0}$
Blade Span	0.3 m attached to a 1.3 m string
Coning Angle	77^o
Spin Rate	180 deg/sec
Tip $C_{l,0}$	0.2
Root $C_{l,0}$	0.4
Tip Chord	0.2 m
Root Chord	0.08 m
Tip α	3^o
Root α	15^o

Table 4.4: Comparison of lift estimate results across the three methods described.

Method	**Value**	**Ref.**
BET Predicted Lift	0.0280 N	Fig. (4.33)
Force Balance Tip Lift	0.0285 N	Fig. (4.15)
Catenary Parameter	0.0293 N	Eq. (4.13) & Eq. (4.9)

nearly as good, with the drag calculated from the test rig being 0.0865 N compared to expectations on the order of 0.003 N. One possibility for this significant error are 3D wing effects like tip vortices which would cause an increase in drag that is not accounted for in the force balance model. Another possibility could be drag from the strings, which the model also doesn't account for.

Figure (4.35) shows the variation in the position of the tip marker LED as seen by the tracking camera, with the lag and coning angle variations referenced to their mean value during the billowed test case. With the measurement interval only capturing two full rotations of the gossamer propeller it is difficult to pinpoint the source of these variations, however, one likely source of disturbance could be air currents within the testing room. The slow periodicity of the variation suggests this is possible, with a steady airflow in the room causing a higher or lower airspeed across the blade section at two specific points normal to the current. This does not explain Fig. (4.35) entirely, as we would expect the period to match the rotor spin rate more closely (visualized with the black dashed lines) rather than be approximately twice as fast. Dynamic modes in the blades could be contributing, and dynamic damping of the blade tips by changing the string lengths during a rotation could improve stability performance.

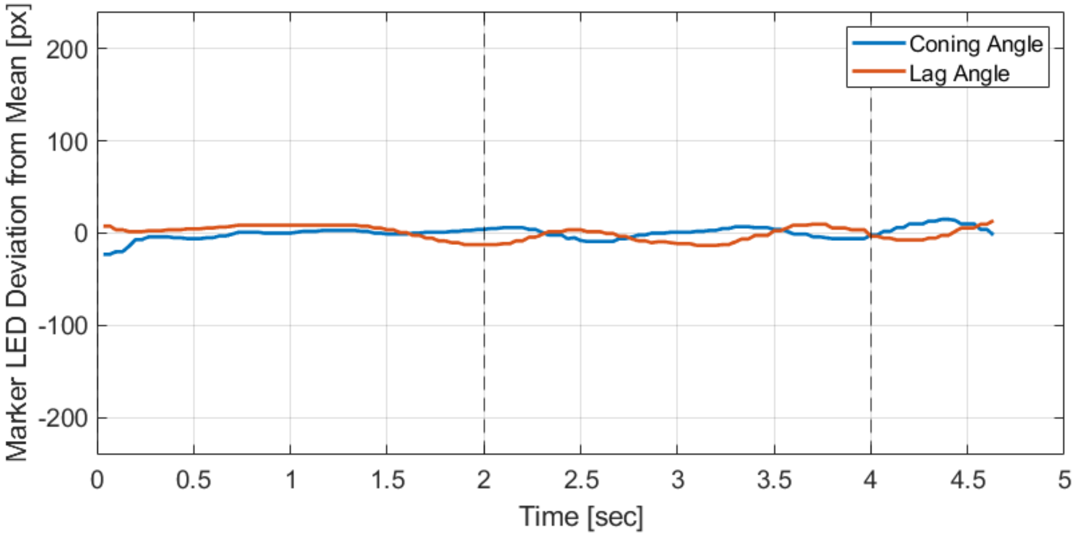

Figure 4.35: Variation in the position of the tip marker LED as seen by the tracking camera, with the lag and coning angle variations referenced to their mean value during the billowed test case. Black dashed lines indicate the rotation period of the rotor.

4.6.1 Future Work for the V5 Test Rig

A first step in improving the V5 test rig would be verifying the drag calculations with a known drag force. This could be conducted by spinning a small party balloon or paper cone at the blade tip and removing the wing surface entirely. A spherical balloon or cone spinning at a known rate would have a much better-defined drag force, which could be compared to the estimates obtained by the force balance method. A brief user manual for the test rig is compiled in Appendix A.

While this research focused on static blade stability and initial performance figures, the test rig is built with future studies in mind. The strings themselves can be dynamically adjusted with the servo spools and feedback from the analog encoders, and feeding in tip position could allow for finer control of the propeller's lift and drag. This tip position feedback could be used to dampen the oscillations from the room disturbances that impacted these results. Additionally, while only a single blade was studied here, the impacts of both collective and cyclic inputs on multiple blades of the gossamer propeller could be explored in the future using the same test rig.

4.6.1.1 Chord-Wise Depth Measurements and Wing Shape

The depth camera can also be used to study the shape of the blade section in the chord-wise direction, in addition to the span-wise analysis that was the focus of this research. Preliminary study of chord-wise depth data, presented in Fig. (4.36), shows the billowed blade section with catenary fits taken at three chord stations along the blade's span (near the tip, though inboard enough to remain outside the distortion area from the marker LED, in the middle of the blade, and near the blade root). Note that this frame was chosen specifically during a time of large billow (higher than the average billow and angle of attack seen during the test) in order to more clearly see variations across the span.

A clear increase in camber and angle of attack is evident due to the billowed gossamer blade section. In the future, this kind of data could be used to improve BET models of gossamer propellers

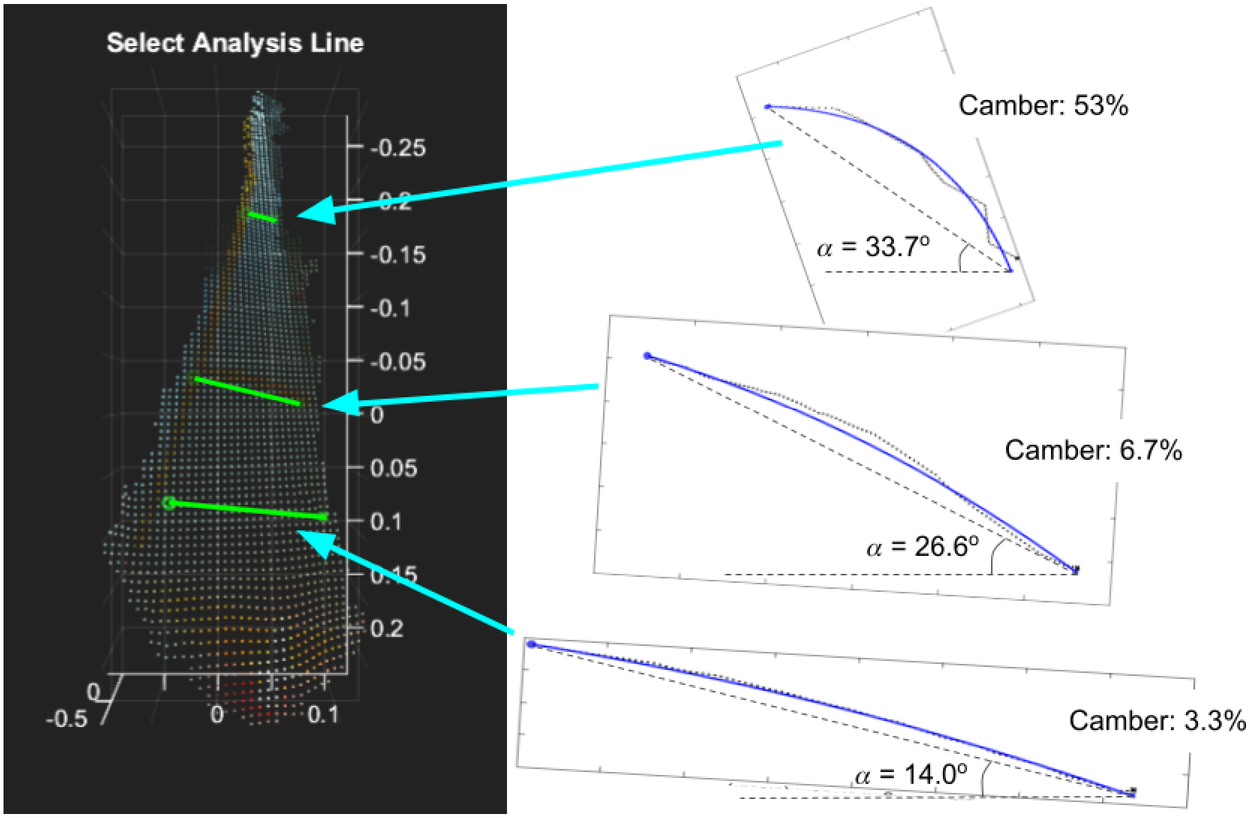

Figure 4.36: Catenary fits along the blade's span in the chord-wise direction showing the increased camber and angle of attack nearer the blade root from billow. Plots to scale and rotated to orient the relative wind of the blade from left to right.

and better understand the distribution of lift across other blade sections.

4.6.1.2 Wider Applicability

Small improvements aside, the test rig can be valuable for more than just the testing of gossamer blades for scientific balloons. As the optical measurement methods described above do not rely on assumptions of blade shape (in the case of depth tracking) or blade lift distribution (in the case of tip tracking), other forms of flexible aerodynamic surfaces could be tested using the same setup. The V5 test rig is another possible tool in the toolbox of engineers and experimental aerodynamicists as an alternative to the wind tunnel, particularly in cases where the structures would be negatively affected by direct force-sensing instrumentation.

4.7 Contributions to Gossamer Blade Stability

While initially inspired by heliogyros, the differences in gossamer blades used in space vs in atmosphere cannot be understated. The fundamental forces involved are simply much larger in atmosphere, and so new methods of ensuring blade stability were needed. The 4-bar link rigging method provides a way to achieve static stability of gossamer blades without any rigidizing structures, deriving stiffness from the centripetal tip forces alone. This represented a turning point in gossamer blade research for lift augmentation, as without the stability afforded by the 4-bar link, generating appreciable lift was not possible. Future work can now go towards better understanding the dynamics of these atmospheric gossamer blades, much in the way recent heliogyro research has focused on dynamic stability and control.

Chapter 5

Scalability Considerations

5.1 Model Overview

An analytical model was designed to explore the scalability of the lift augmentation device being developed. Decoupled from the specifics of blade dynamics and stability, the scalability model is designed to answer questions like, “Given an achievable lift:drag ratio, how fast would a lift augmentation device need to spin in order to cause an ascent/descent rate of X m/s?” and “If the blades spun at Y rpm, how fast would the balloon need to spin in order to counter the torque with viscous drag effects across the balloon surface?” Additionally, it is designed to help explore what parts of the design change as we transition from the ground-based testing discussed earlier to full scale tests. “What properties of the blades can change if larger or smaller balloons are used?” and more importantly, “What does an optimal lift augmentation device look like, and how do we even define optimal here?”

The model consists of a handful of separate MATLAB scripts for different parts of the study. An initial requirements identification script *rotorRequirements.m* models the expanding balloon to determine the form drag it experiences as it rises through the atmosphere. This allows for easily determining how much lift is required to achieve a desired ascent speed, which can be fed into other analysis scripts. To calculate the drag of the balloon, Boyle’s Law is used to calculate the volume (and subsequently the frontal area) of the balloon at varying altitudes which then directly feeds into Eq. 2.2. A custom implementation of the Standard Atmosphere is utilized [80], which allows a wider range of altitude inputs and also is more efficient and better documented than the MATLAB implementation, making modifications easier and large-scale simulations faster. This generates a handful of basic requirements based on just the balloon: specifically, the drag on the balloon at varying ascent/descent speeds as seen in Fig. (5.1).

These results can then be used to help inform the starting point for analysis of the blade design. The *rotorTradeStudy.m* script takes in balloon parameters and requirements and varies the design of a lift augmentation device, changing the length of the top and bottom strings (which most directly affects the blade coning angle and relative wind speed), the length and area of the blades (which most directly influences the lift and required rotor torque), and the rotation speed of the rotor (directly impacting the relative wind speed and therefore the lift). The analysis outputs a series of surface contour plots that visualize the effect of these scaling variables on things like power consumption, necessary rotor torque, and balloon counter-spin rate. The number of blades can also be varied.

Lift is calculated on these blades using a simplified Blade Element Theory model using a single section. Drag is then computed using a fixed L/D ratio rather than from BET, a decision that was made mostly due to the uncertainty in precise drag calculations for flexible blades at low Reynolds numbers. A single L/D scaling parameter allows models to be updated as a better understanding of these forces becomes available.

5.2 Baseline Design

The design baseline will start with the balloons used for many of the HYFLITS launches, which were 3000 g balloons approximately 3.6 m in diameter when launched. As the balloon ascents, Boyle's Law predicts they grow to greater than 14 m in diameter by 30 km. Since one goal with lift augmentation was to provide a mounting place for turbulence sensors which are outside the balloon wake, the blades would need to be larger than this balloon radius. As a baseline, analysis will continue with an upper string that is 10 m long including the blade. This provides margin outside the balloon wake and also keeps the tips outside the balloon radius even with larger coning angles. Additionally, the operational altitudes of our balloon system will also mirror that of HYFLITS,

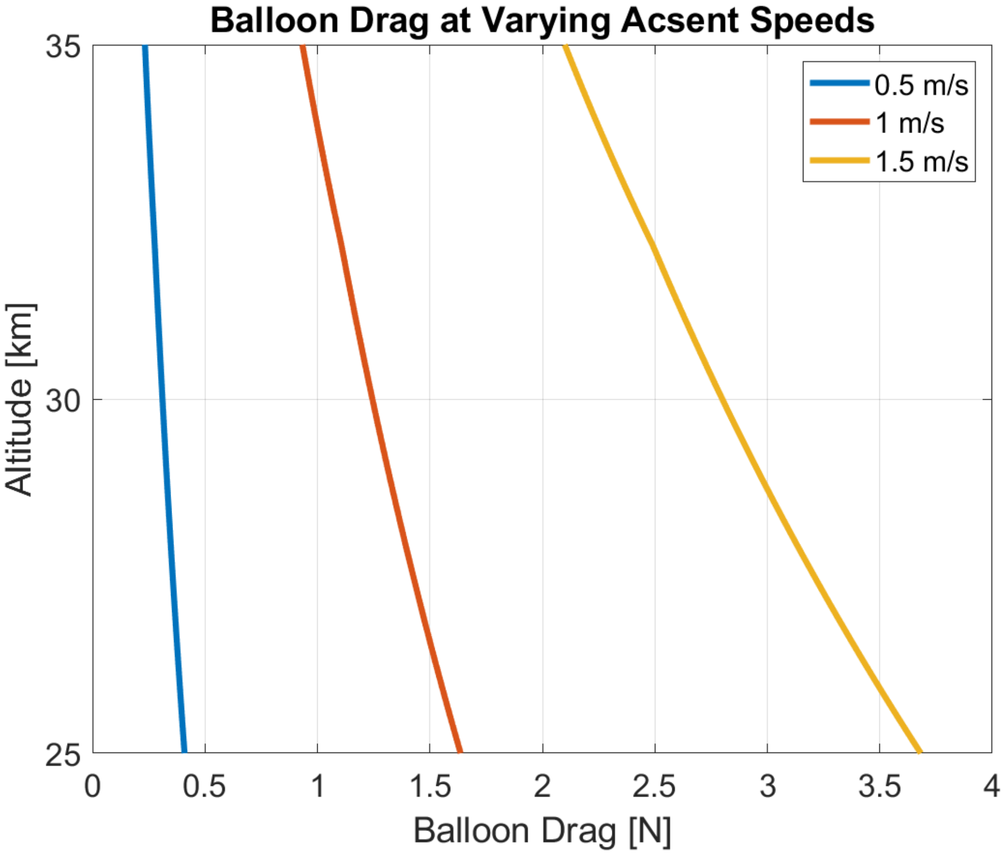

Figure 5.1: Form drag of a 3.6 m balloon (at ground level) from various translation speeds when operating in the stratosphere (where it grows to 15 m). While the balloon's area grows as it ascends, the thinner air results in a reduction of form drag with altitude.

aiming to profile between 25 km and 35 km.

A baseline for the design of the blades themselves will also be useful when considering optimizations later on. As such, the blades should have the properties and parameters as described in Tbl. 5.1.

Table 5.1: Properties of the baseline full-scale lift augmentation design for further analysis.

Property	**Value**
$C_{L,\alpha}$	5.9
Blade Span	1 m (attached to a 9 m string for a total length of 10 m)
Blade Count	3
Lower String Length	9 m
Rotor Spin Rate	1 RPM
Required Translation	1 m/s
Chord Length	0.1 m
L/D	7

A lift curve slope of 5.9 comes from Airfoil 8 in [83] and also is reasonably close to the 2π lift curve slope we would expect from thin airfoil theory. Additionally, the baseline L/D of 7 is simplistic but will serve as a reasonable baseline. In the future, results from [83] could also be incorporated, or other sources on low Reynolds number aerodynamics could be further explored.

A 3 blade propeller serves as the baseline as it strikes a realistic balance between complexity and blade area. Further, a 2 blade design might be more susceptible to variations in tip lag causing an unbalanced rotor, resulting in oscillations of the entire vehicle. Additional blades could reduce spin rate and length requirements by providing a larger wing area which to generate lift, but are not being considered in this research due to the operational complexity that such multi-blade gossamer propellers could entail (particularly for deployment).

5.2.1 Blade Coning Angle

The coning angle of the blade is a critical factor in the operation of a lift augmentation system, defining the effective airspeed over the wing section, the distance at which the blade's drag creates torque, the fraction of the total lift force that is directed "upward" (in the frame of the balloon), and the overall distance outside the balloon's wake any instruments on the tip may be situated.

For a single string, the coning angle θ can be derived using the force balance described in Fig. (4.1). In Eq. (5.1),

$$\theta = 2\arctan\left(\sqrt{\frac{\sqrt{g^2 + 4l^2\omega^4} - 2l\omega^2}{g}}\right) \tag{5.1}$$

However, the lift augmentation device as described uses both upper and lower strings in order to control the blade's angle of attack. There are 3 possibilities, shown in Fig. (5.2): 1) The upper string is tensioned but the lower one is not; 2) Both string are fully tensioned; and 3) The lower string is tensioned but the upper string is loose.

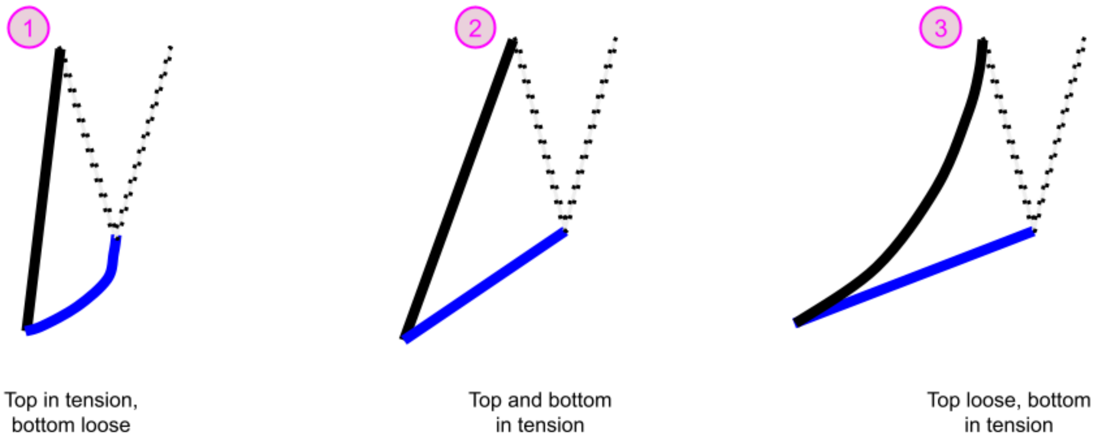

Figure 5.2: String tension states of upper and lower strings when spinning.

If the goal is to remain in a condition where both strings are tensioned, which provides continuous control of the tip (via the lower strings) and stability of the blade (via the 4-bar links in the upper and lower strings) then situations 1 and 3 would require adjustment. From 1, either increasing the rotation rate of the rotor or reducing the deployed length of the lower string would return the device to tensioned equilibrium. Conversely from condition 3, reducing the spin rate or increasing the length of the lower strings would bring the system back to equilibrium. There is then a range of spin rates and/or lower string lengths that result in equilibrium. This result is described in Fig. (5.3), where a fixed length upper string (blade line, 10 m long) and differing lower string lengths (blue lines, length indicated on right) are spun at various spin rates (x-axis). The resulting coning angles are visualized on the y-axis. The area between curves shows the equilibrium region. So, for an upper string length of 10 m and a lower string length of 2 m, there is a larger equilibrium range than for a lower string length of 6.5 m.

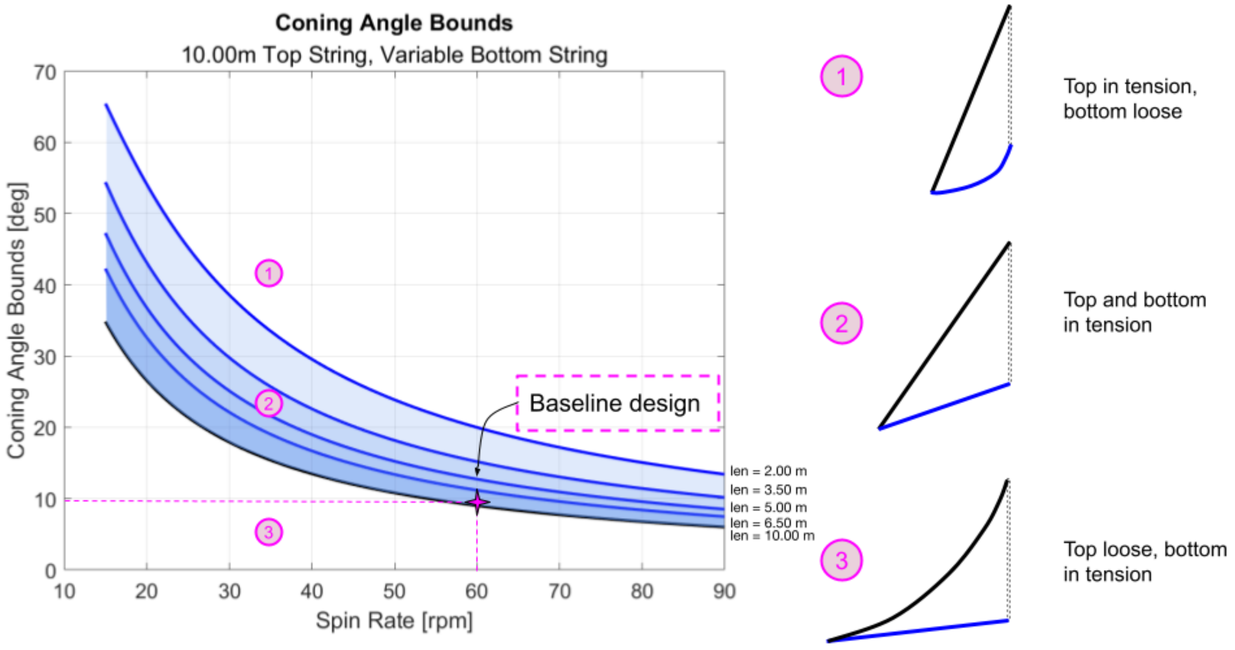

Figure 5.3: Equilibrium ranges of various string lengths at different spin rates, as well as the fixed coning angle of the baseline design given the defined string lengths and spin rate.

While a given rotation rate can accommodate a range of string lengths, and vice versa, if *both* the string length and rotation rate is known, there is only a single unique coning angle where both the upper and lower strings are in tension. Thus, for the baseline design described with 10 m upper strings and 9 m lower strings at a fixed spin rate, the coning angle is constrained to 9.27^o as indicated in Fig. (5.3).

5.2.2 Torque Requirements

Required torque is a major driving factor in the design of a full-scale lift augmentation system. Higher torque requirements lead to needing a larger drive motor, increasing cost and weight, as well as larger required balloon spin speeds (or a second motor for counter-rotating blades). Figure (5.4) shows the required blade motor torque for the baseline design at three different ascent speeds.

Note that the baseline design can only operate within the full altitude envelope of 25 km - 35 km with the slowest translation speed of 0.5 m/s. At 1 m/s, the blades simply do not produce enough lift above 33 km, and for a 1.5 m/s translation, altitudes above 25.2 km are not achievable. To operate in those regions at those desired speeds, either the blades would need to be larger or would need to spin faster.

As expected, the torque required vs. altitude remains fairly constant, decreasing slightly with altitude. While the air is much thinner at 35 km compared to at 25 km which reduces drag from the blades, that thin air also leads to a decrease in lift, meaning the blades must spin faster to produce the required translation speed (resulting then in more drag). The reason torque requirements still decrease slightly overall is due to the form drag of the balloon also decreasing as seen in Fig. (5.1), meaning while the thin air reduces lift production, less lift is required to translate the balloon system.

5.2.3 Power Requirements

Related to torque is the required power for translating at some desired speed. This power is calculated according to Eq. (5.2), where P is power, τ is rotor torque (as described above), and ω is rotor spin rate (60 RPM for the baseline).

$$P = \tau\omega \tag{5.2}$$

This represents an ideal, minimum power to operate, and doesn't consider factors such as mechanical efficiency or any other losses associated with generating or storing power. Rather, this

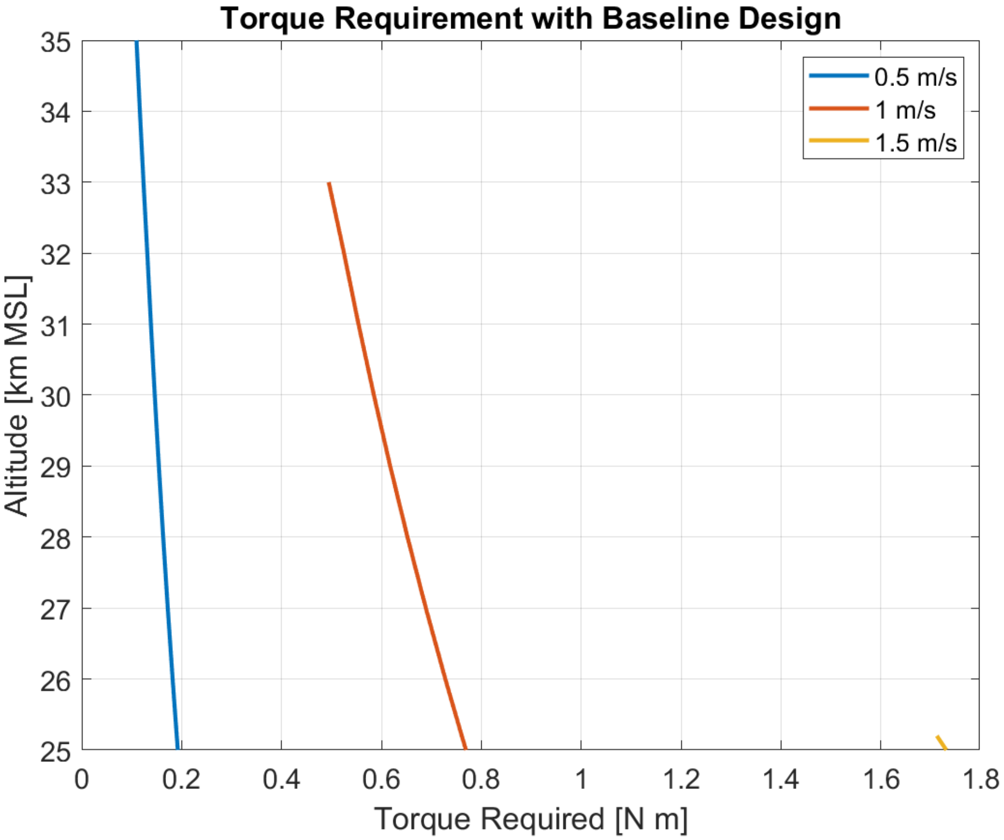

Figure 5.4: Torque required for various ascent speeds of the baseline lift augmentation design. Note 1.5 m/s translation is not possible above 25.2 km with the baseline design.

figure provides a minimum starting point with which to compare designs.

Given the fixed rotor spin rate τ of 60 RPM for the baseline, the power requirements mirror the torque requirements. Further analysis on both torque and power will be conducted as we scale the system in future sections, resulting in more interesting power trends.

5.2.4 Spin Rate Requirements

The balloon spin rate is the final major trade result to explore for design optimizations. The torque from the motor must be balanced, and by spinning the balloon itself, we generate viscous drag on the surface producing a counter-torque based on the balloon's radius. These viscous forces are described in [54], and calculated according to Eq. (5.3), where T is torque generated by a rotating sphere, ν is the kinematic viscosity, ρ is the air density, R is the radius of the sphere (in this case, the balloon), and Ω is the spin rate of the balloon.

$$T = 8\pi\nu\rho R^3\Omega \tag{5.3}$$

The viability of this strategy for countering rotor torque likely depends on many unknown factors, but is certainly dependant on how fast the balloon would need to spin. Spin rates which are too large may cause the balloon to burst. On the other hand, this rotation causes the balloon to flatten out (taking the shape more of a pancake than a sphere), which would increase the viscous torque generated as more of the balloon would be farther away from the center of rotation (this would also effect the balloon drag and rotor lift requirements). Ultimately, spinning the balloon as a counter for rotor torque is a complex problem requiring further investigation and testing. These results can serve as a starting point.

The trends from Fig. (5.6) vary from those of torque or power, having much more sensitivity to altitude and spin rate than the other design variables. Given the reduced atmosphere at altitude and only slight reduction in rotor torque, one might expect the required balloon RPM to increase with altitude, as viscous forces would reduce. Instead, the required balloon RPM actually decreases significantly. While it is true the aerodynamic effects are depressed as altitude decreases if all else

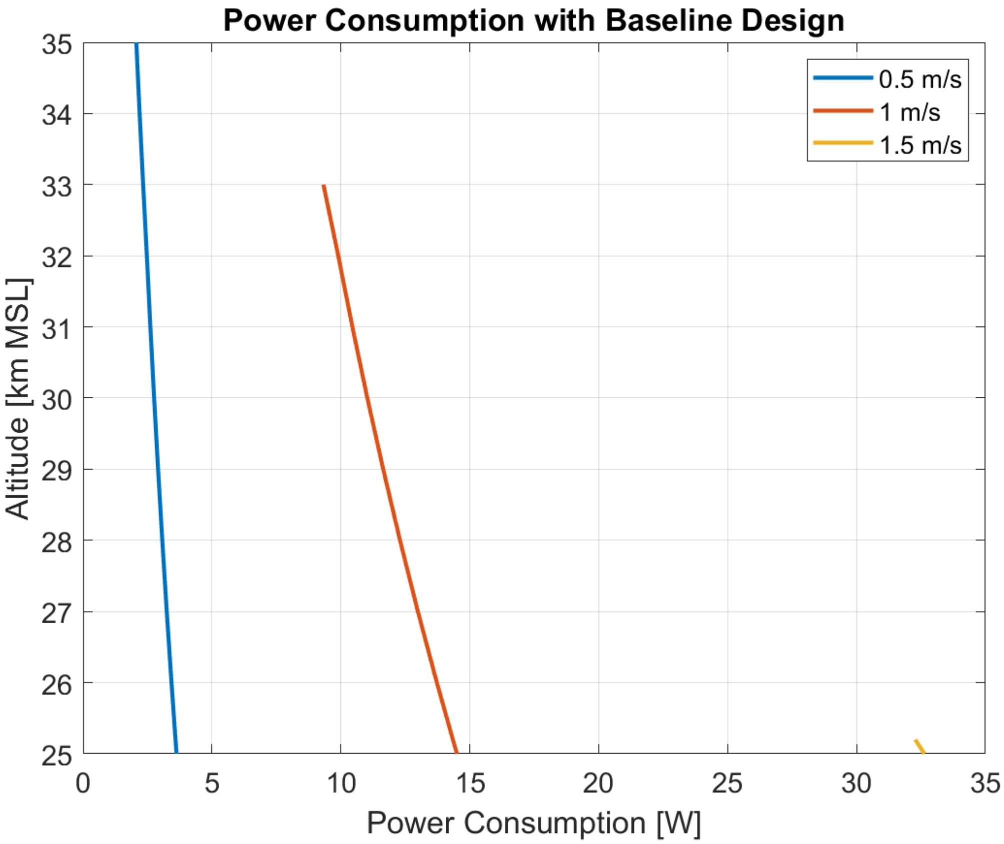

Figure 5.5: Power required for various ascent speeds of the baseline lift augmentation design. Note 1.5 m/s translation is not possible above 25.2 km with the baseline design.

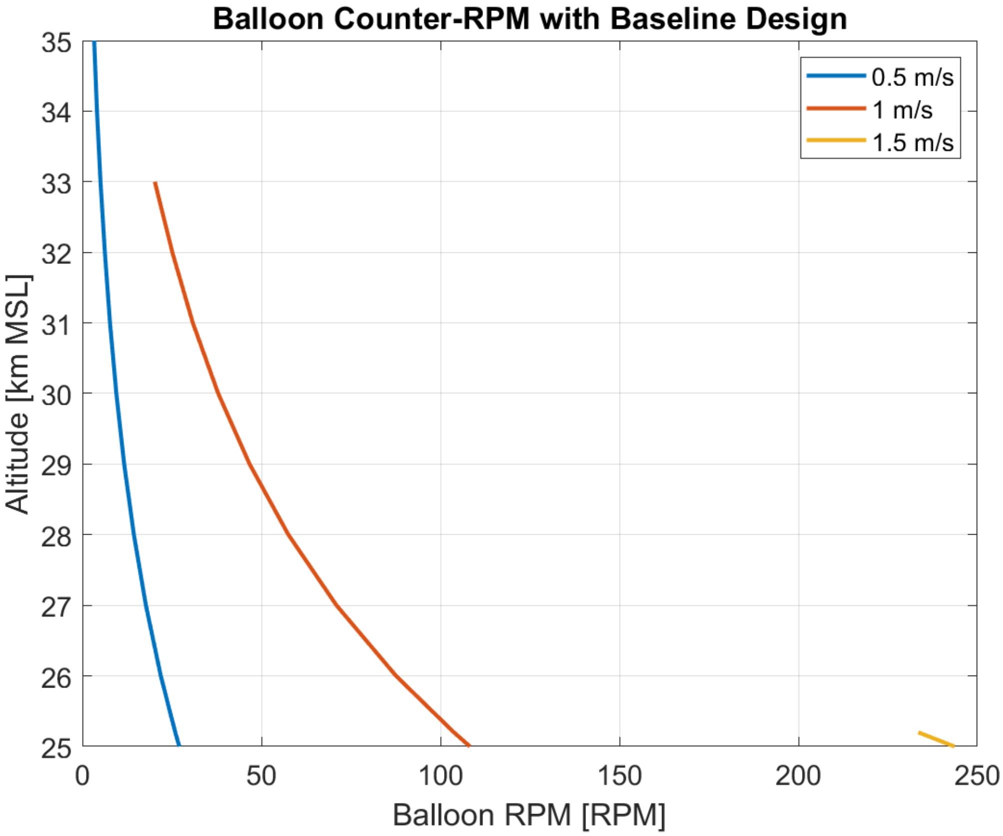

Figure 5.6: Balloon RPM required for various ascent speeds of the baseline lift augmentation design in order to counter rotor torque with viscous effects. Note 1.5 m/s translation is not possible above 25.2 km with the baseline design.

remains constant, the increasing radius of the balloon increases its surface area and causes these forces to act on a much larger radius, increasing the balloon's torque significantly.

Still, the balloon RPM remains higher than that of the rotor, as the viscous drag effects are less pronounced and the rotor radius is larger than that of the balloon (in order to remain outside its wake). One alternate idea for countering the torque from the rotors is to use counter-rotating blades. While this can be advantageous by not relying on spinning the balloon, it also provides double the lift resulting in much lower required spin rates! Two major drawbacks however are the increased cost, mass, and power requirements of needing to spin two rotors, as well as the increased complexity of deploying two separate lift augmentation devices in opposite directions on a potentially unsteady scientific balloon. These challenges remain a future step towards a full scale device.

5.3 Deviations from Baseline

With a baseline established, design changes can be made to determine their effects on lift augmentation. Two trade variables will be analyzed: overall upper string length and rotor spin rate. Their effects on coning angle, torque, power, and balloon spin rate will be studied and compared. For each case, the lower string will be constrained to 90% of the length of the upper string (i.e. like in the baseline where the upper string was a total of 10 m and the lower string was 9 m).

Figure (5.7) shows the effects of string lengths from 5 m - 25 m and rotation rates of 10 RPM - 100 RPM on the system result variables at an altitude of 30 km. Notice how the slowest spin rates and smallest string lengths, despite a full-size (1 m) blade, cannot produce enough lift to achieve the target 1 m/s translation speed. Additionally, the 1:1 mirroring of power and torque no longer holds with the changing rotation speeds due to the system targeting a minimum lift condition (resulting in minimum drag) regardless of spin rate, which is why torque remains relatively spin rate agnostic. It takes more power to spin faster though, so generally longer strings (more torque) and higher spin rates require the most power. As expected, the coning angle is smallest (the rotor disk is flattest) for higher spin rates, and only as this spin rate increases when the centripetal forces begin to overpower gravity forces do we see the coning angle being significantly influenced by string length.

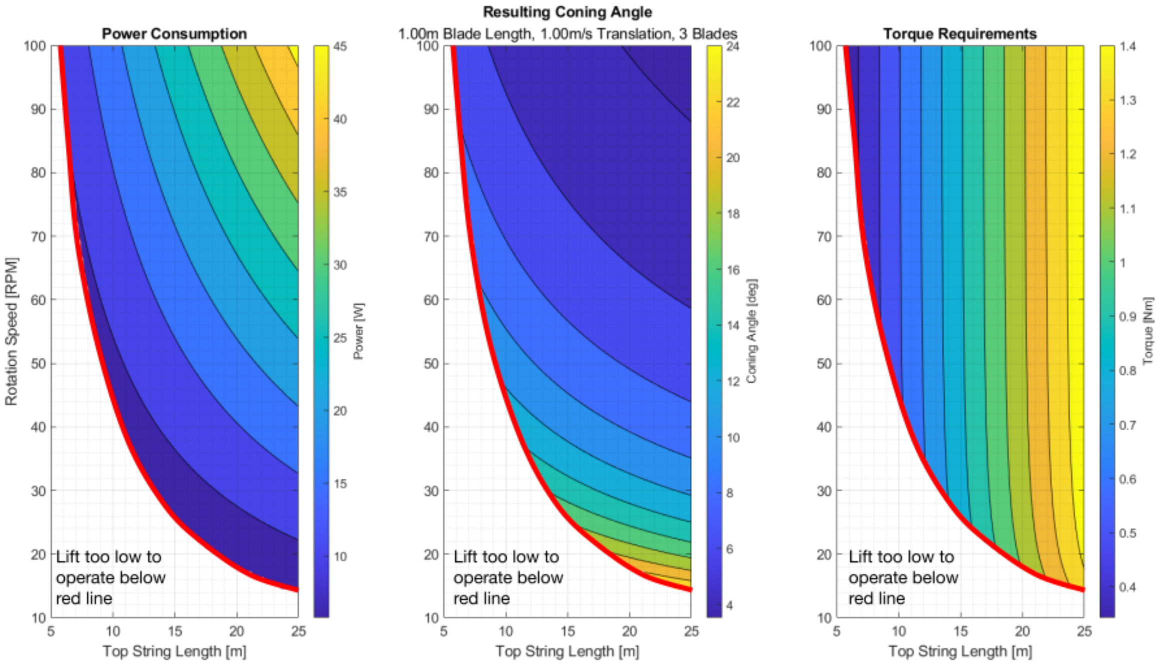

Figure 5.7: Effects of various string lengths and rotation speeds on power, coning angle, and torque. 3.6 m balloon (at ground level) for a 1 m/s translation at 30 km.

The balloon's spin rate follows the same trend as rotor torque, which is expected because it is directly proportional to the viscous drag torques it produces.

5.3.1 Interpreting Trade Study Plots

With multiple free variables (2 in this case; rotor spin rate and string length) and even more resultant impacts (4 here, rotor torque, rotor coning angle, rotor power, and balloon spin rate), these trade study plots can have a lot to unpack.

The first thing to recognize is the shaded areas vs the bare white space below and to the left of the red curve. This curve represents the line of zero margin for lift generation. The blade is limited to an angle of attack of 10^o, and on this line, the blade angle reaches that limit. Operation of the lift augmentation device below and to the left of that line is then impossible if the full 1

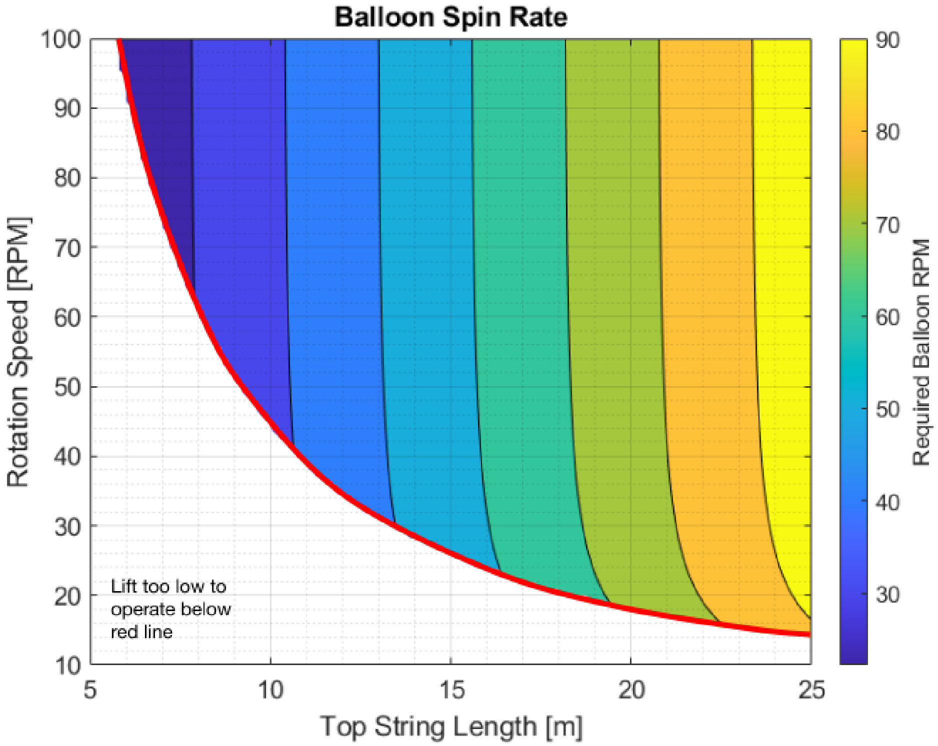

Figure 5.8: Effects of various string lengths and rotation speeds on balloon spin rate. 3.6 m balloon (at ground level) for a 1 m/s translation at 30 km.

m/s translation speed is to be reached. Moving farther from the red curve (up and right) then represents blade angles reducing and the margins for generating extra lift (by increasing the blade angle of attack) increasing.

Focusing on the baseline plots in Fig. (5.7), it is clear that a 10 m top string spinning at 30 RPM would not produce enough lift to operate. Instead, the 10 m propeller could spin faster (the minimum operating speed is approximately 45 RPM), a 30 RPM rotor could use longer strings (the minimum operating length is approximately 13.5 m), the blade section could be increased from 1 m, or a combination of increased speed, string length, and blade size could be used.

If the interest is to minimize both design variables, a tangent bisection method could be used to locate the knee of the curve of zero lift margin as in Fig. (5.9).

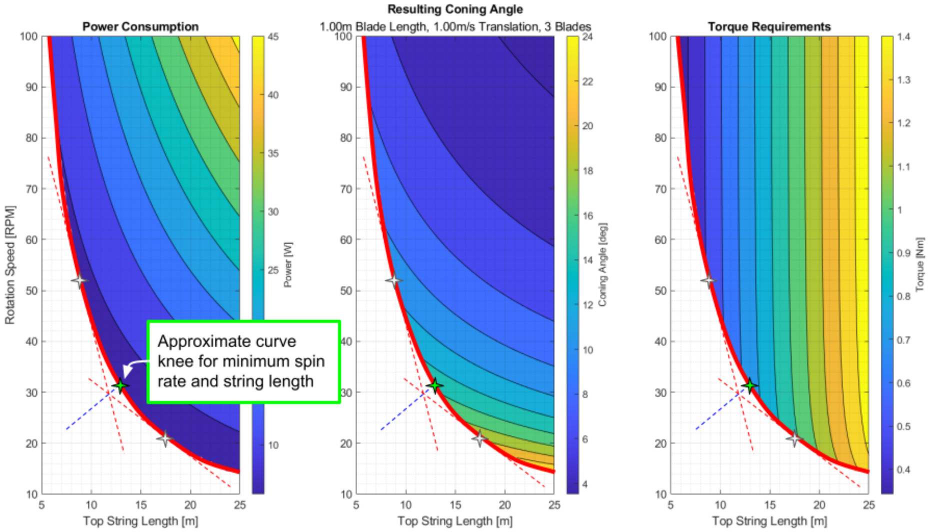

Figure 5.9: Tangent bisection method applied to the zero margin line to locate the minimum spin rate and string length combination for operation of the baseline balloon at a 1 m/s translation speed at 30 km.

While this point, located at approximately 13 m string length and 33 RPM rotation rate is the minimum of the design variables, interestingly it does not at all align with the minimums of power consumption, coning angle, or torque requirements. Such minimums often lie near the upper and lower bounds of trade variables, which will be discussed further in Sec. 5.8.

Generally, required torque is not very dependent on spin rate (indicated by the near vertical lines of the third panel in Fig. (5.7) and in Fig. (5.8)). This is a result of the blades dynamically changing their angle of attack to only produce the necessary lift. Given the fixed L/D assumption of 7:1, this fixed lift results in fixed drag (and therefore torque for a fixed string length regardless of rotation speed). In contrast, coning angle is much more independent on string length (the opposite trend vs torque). This is because the coning angle is governed by a balance between centripetal loads and gravity loads. The centripetal forces have a squared relationship with spin rate compared to a linear relationship with distance, so spin rate is a much more critical factor in determining coning angle than string length.

With the simplified power relationship from Eq. (5.2), it is no surprise that power is dependent fairly equally on string length and spin rate.

5.4 Effects of Balloon Size

While analysis thus far has focused on smaller, hand-launched balloons (though they still may require multiple personnel to launch), there are many other classes of scientific balloons which could take advantage of lift augmentation. From much smaller 1000 g and less balloons up to massive super-pressure balloons, how would a lift augmentation device operate?

Mass aside, you would expect a smaller balloon to require less lift to achieve a similar translation speed due to its reduced form drag. Conversely, however, the smaller balloon would produce less viscous torque, so balloon rotation rates would be expectantly higher than larger balloons.

Figures (5.10) and (5.11) show the scalability impacts of lift augmentation of a much smaller balloon, starting at just 1 m in diameter on the surface and growing to only 4 m at 30 km. As expected, the torque (which is proportional to the lift generated) is two orders of magnitude smaller than for the larger 3.6 m balloon (which grew to nearly 15 m). However, this greatly reduced torque did not result in a reduction in balloon spin rate, which remains nearly the same as with the larger balloon. Note that to account for the smaller balloon, the range of string lengths to analyze was reduced to 25% of the previous analysis.

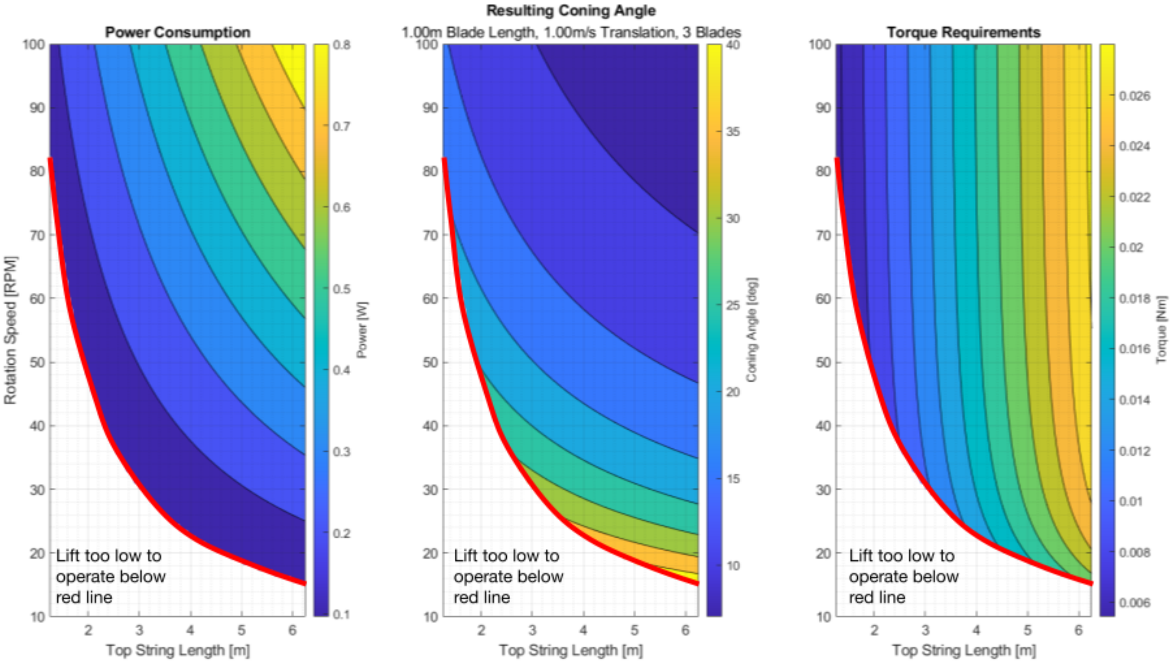

Figure 5.10: Result of using a smaller 1 m diameter balloon (at ground level) on system requirements. 1 m/s translation at 30 km operation remains the same.

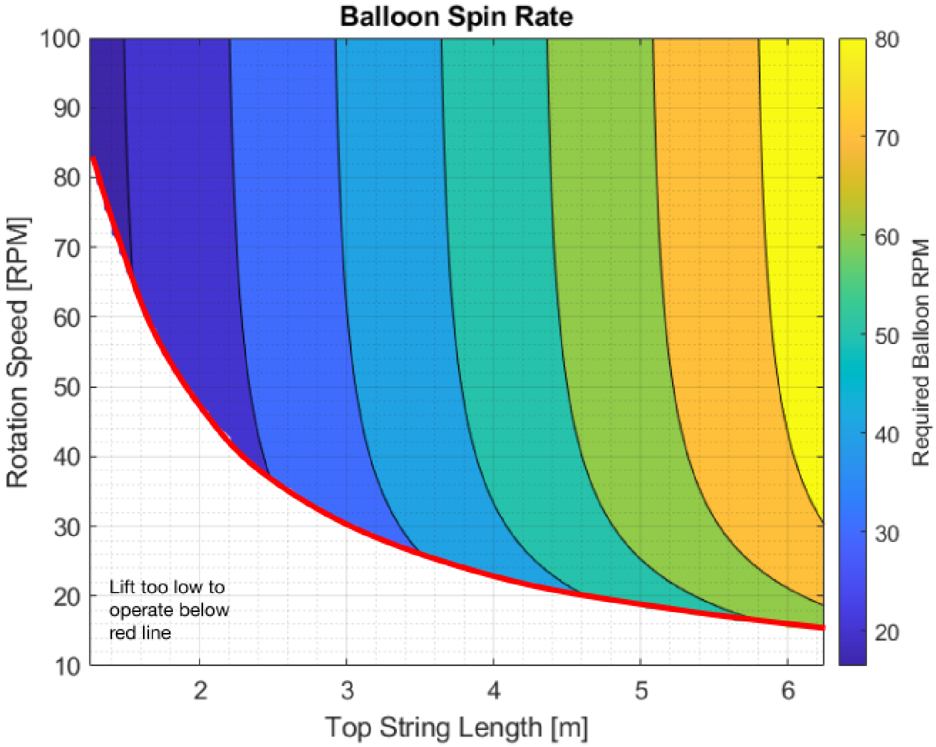

Figure 5.11: Result of using a smaller 1 m diameter balloon (at ground level) on balloon spin rate. 1 m/s translation at 30 km operation remains the same.

The opposite should be true for a large super pressure balloon, which may grow to over 100 m at altitude. Now with string lengths 6x the original (so the tips are still outside the wake for about half of the analyzed cases), and with a 15 m blade section (up from 1 m, again to ensure enough lift can be generated with the larger balloon), the results can be seen in Fig. (5.12) and (5.13). The expected trends hold, with torque now 2 orders of magnitude above the baseline yet only requiring half the balloon spin rate. Note the power however, on the order of 10s of kW. While many large balloons carry comparatively large solar arrays for power, as can be clearly seen in Fig. (5.14), requiring that much power simply for propulsion may not be feasible.

5.5 Effects of Blade Size

Returning to our nominal sized latex balloon starting around 3.6 m on the ground and growing to approximately 15 m, fundamentally, the torque requirements are driven by the drag generated by the blades themselves. Reducing this drag should result in a corresponding decrease in torque, reducing the required balloon spin rate and the power needed to operate the device. Such logic suggests that small blades with large wing areas, spinning just quickly enough to produce the required lift, may be a good operating condition. If the blades could be made small enough, possibly a rigid blade could be used instead of a gossamer one. The results of this are shown in Figs. (5.15) and (5.16). Here, string lengths from 0.5 m up to 10 m were simulated spinning from 60 RPM up to 1000 RPM, where the entire blade section was covered in wing. Even at 1000 RPM, blades shorter than 1 m cannot produce enough lift at altitude to support a 1 m/s translation rate. Note that for the case of a 1 m string, this blade has an identical aspect ratio to the previous baseline design, with an increased aspect ratio for longer lengths due to the entire string length being covered in wing area. The original assumption of L/D of 7 remains constant, however, an approximation which still captures performance trends but would not be strictly true with changing aspect ratios.

While modest reductions in torque and balloon spin rate are achieved, it comes at the expense of a fairly large increase in required power. Additionally, with shorter blades, the tips would not be outside the balloon's wake. This highlights the necessity of gossamer wings vs rigid ones, showing

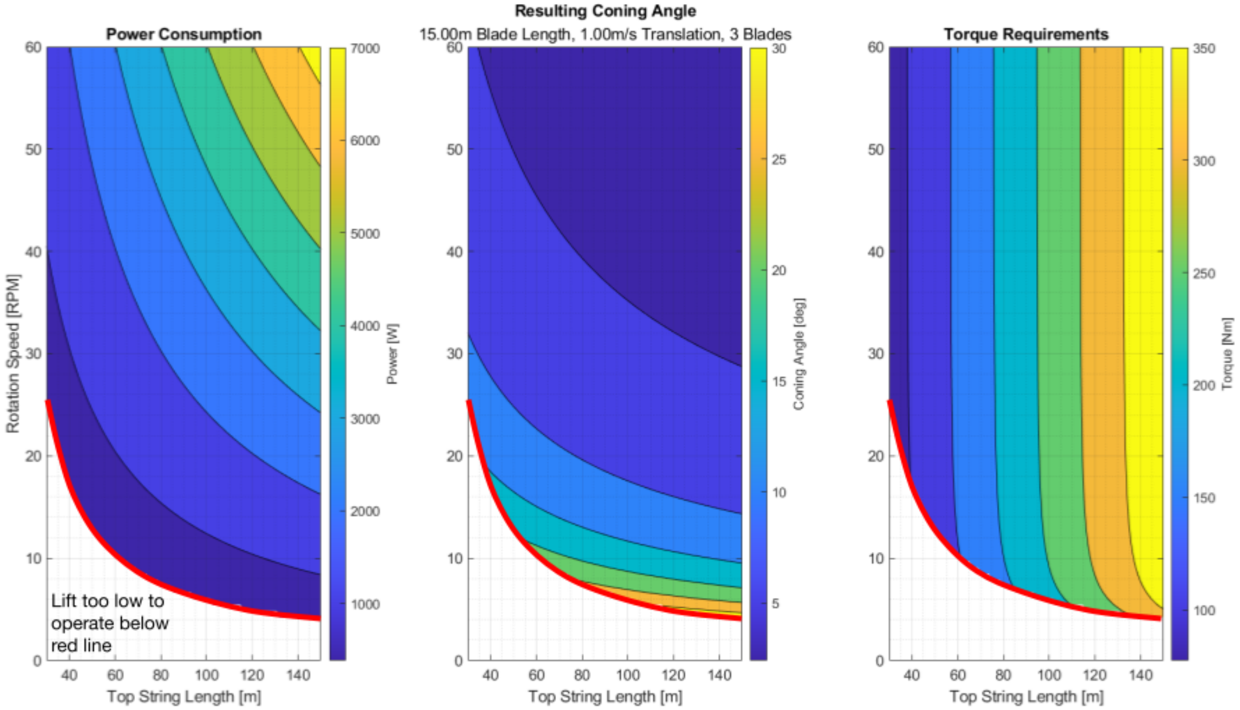

Figure 5.12: Result of using a larger 100 m diameter balloon (at 30 km) on system requirements. 1 m/s translation remains the same.

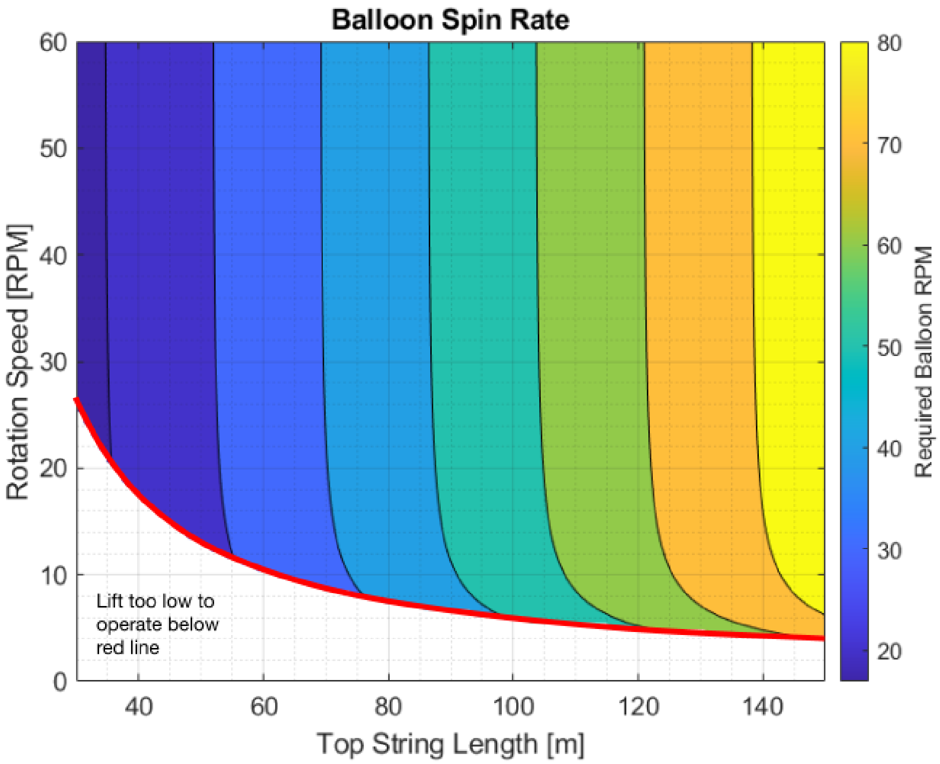

Figure 5.13: Result of using a larger 100 m diameter balloon (at 30 km) on balloon spin rate. 1 m/s translation remains the same.

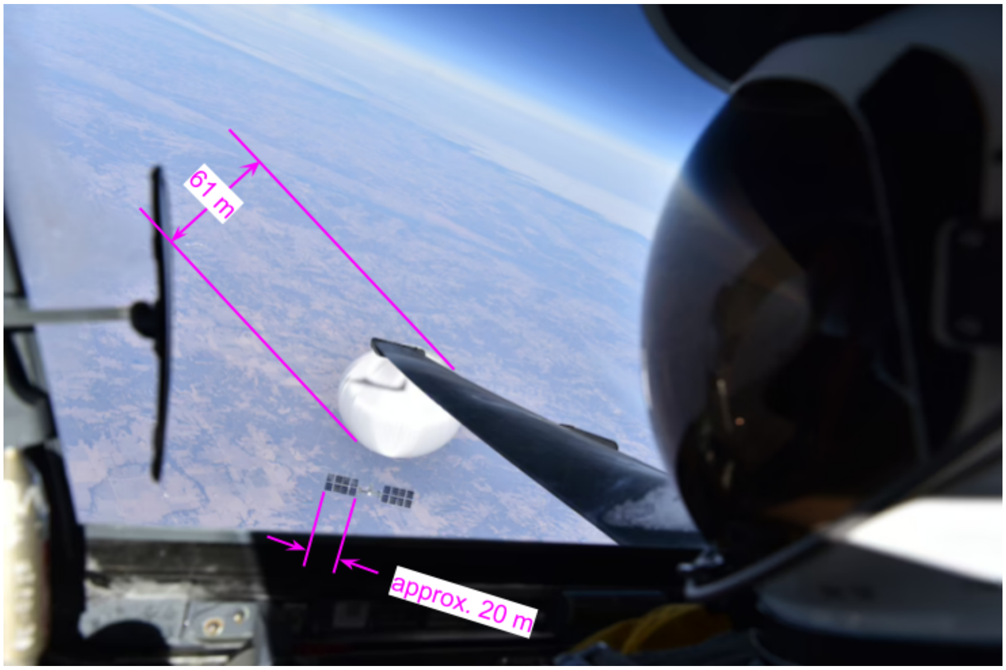

Figure 5.14: Image[49] from a U2 spy plane of the Chinese spy balloon, which was cited as being over 61 m in diameter [49] [71].

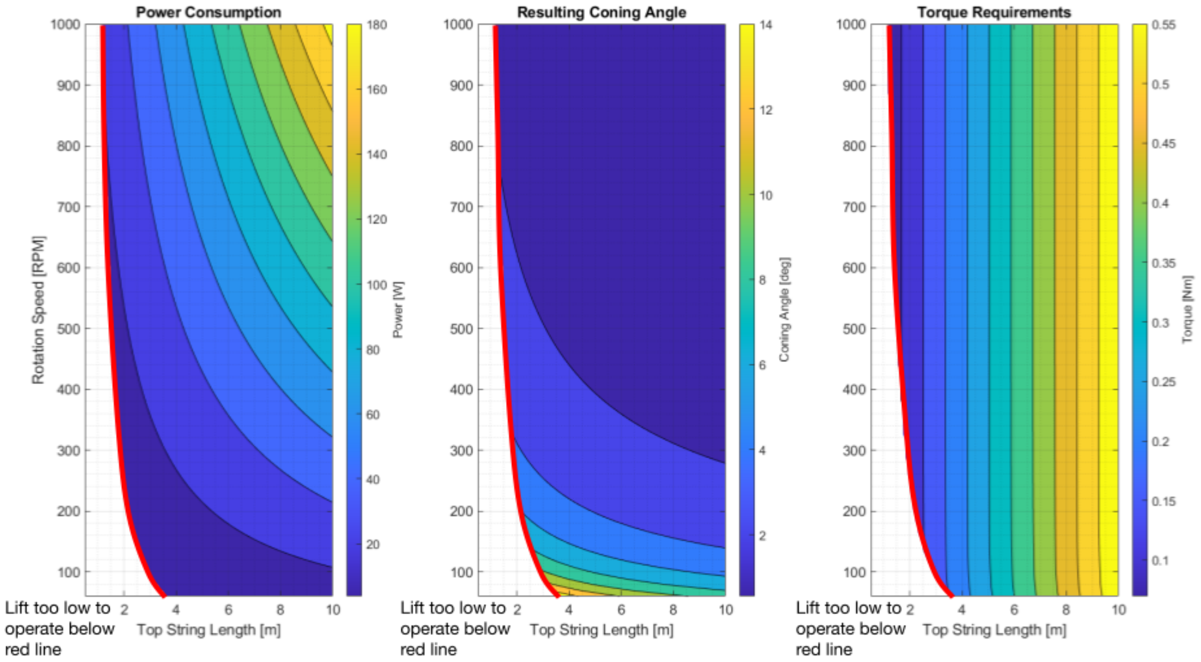

Figure 5.15: Result of short blades spinning quickly with a nominal sized balloon (3.6 m diameter at ground level). 1 m/s required translation at 30 km operation.

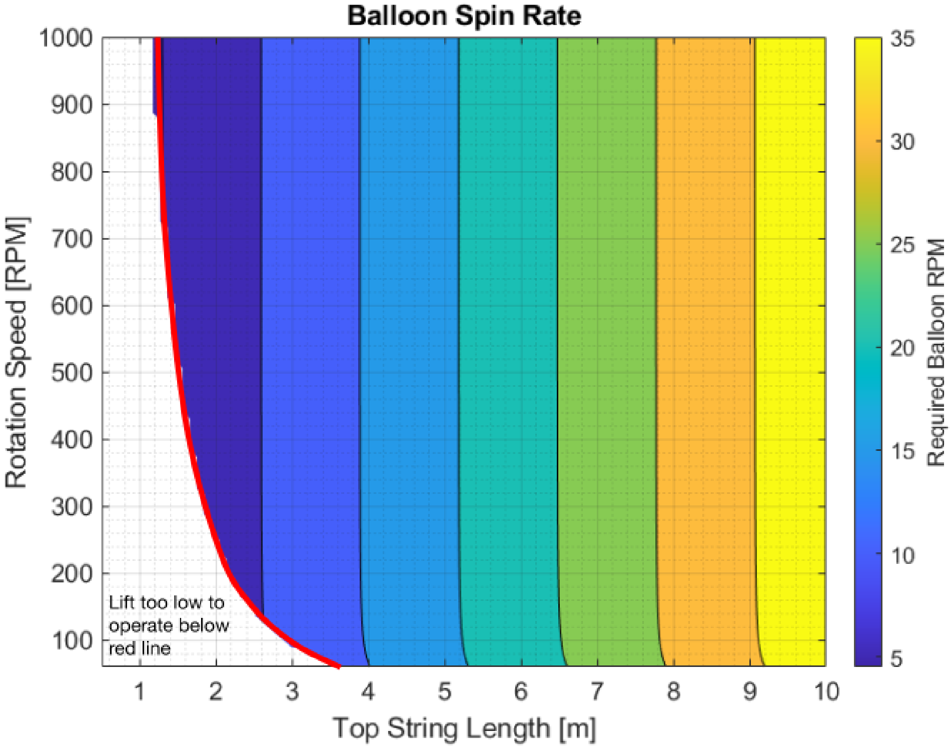

Figure 5.16: Result of short blades spinning quickly with a nominal sized balloon (3.6 m diameter at ground level) on its spin rate. 1 m/s required translation at 30 km operation.

that a 2 m propeller disk still must spin in excess of 1000 RPM to generate enough lift in the stratosphere. Such a propeller, if rigid, would require a significant amount of mass.

5.6 Effects on Martian Ballooning

One exciting prospect of lift augmentation as a form of balloon control is that its design and design principles remain very similar regardless of atmospheric composition. Such a consideration is important given the increased interest in atmospheric science on other planets and moons. As discussed in Sec. 1.2.3 and 2.2.1, the idea of a phase changing fluid has been considered for altitude control. Such a concept relies on specific, known properties of the atmosphere the balloon is flying through in order to tune the choice of fluid to meet mission needs. Different lifting gasses have also been proposed, with water being a possible choice for balloons on Venus [35]. Such balloons would be untestable on Earth, presenting large risk for an expensive spaceflight mission.

Lift augmentation is testable and verifiable on Earth, with the Martian atmosphere in particular very closely resembling that of Earth's stratosphere in terms of the variables that lift augmentation relies on (namely, air density). Figs. (5.17) and (5.18) show the baseline balloon flying on Mars at an altitude of 5 km. Notice that because of the similarity in atmospheric density, the power, torque, and balloon spin are all nearly identical to that of the Earth-based baseline. However, given the reduced force of gravity on Mars, a much lower coning angle can be achieved.

An immediate difference between the Mars simulation plots vs the Earth-based ones is the reduced design area where operations are possible. While before the minimized rotor speed and string length combination was around 13 m and 33 RPM, on Mars this minimum combination does not occur until approximately 18 m and 56 RPM. The difference is a consequence of the Earth's stratosphere not exactly matching Mars's 1:1. As shown in Fig. (5.19), the air density at 5 km on Mars corresponds more closely to 35 km on Earth, and the pressure more closely matches that of 37 km on Earth. These are much higher than the original baseline plots were generated at.

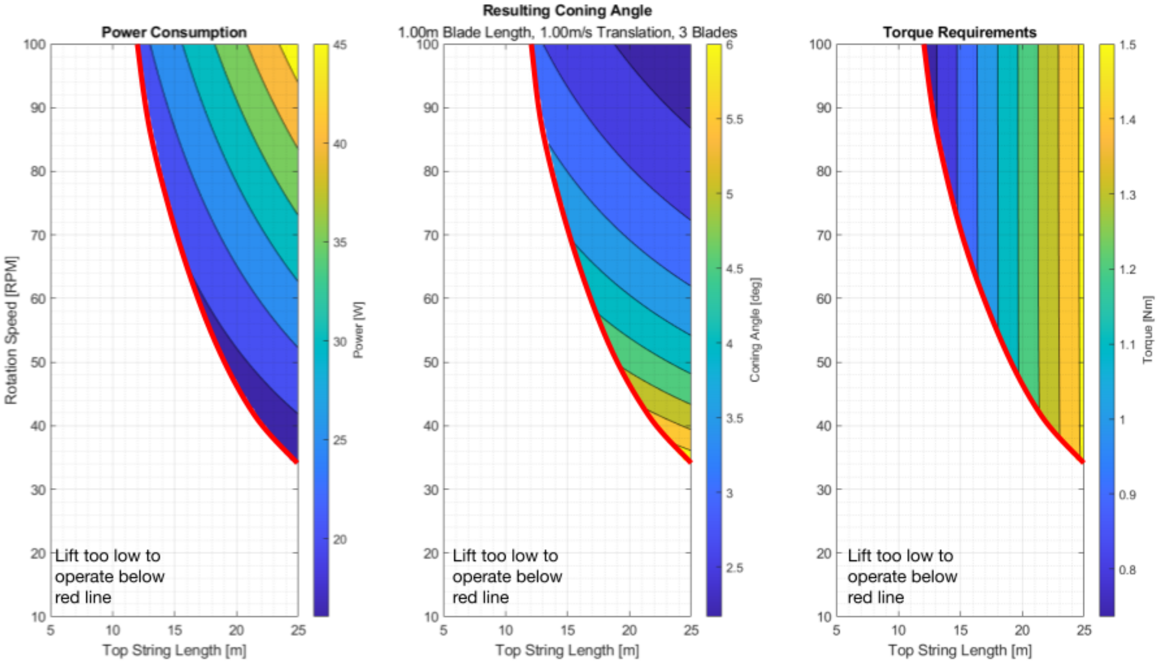

Figure 5.17: Baseline balloon (3.6 m diameter at ground level on Earth) lift augmentation device flying at 5 km on Mars for a 1 m/s translation requirement.

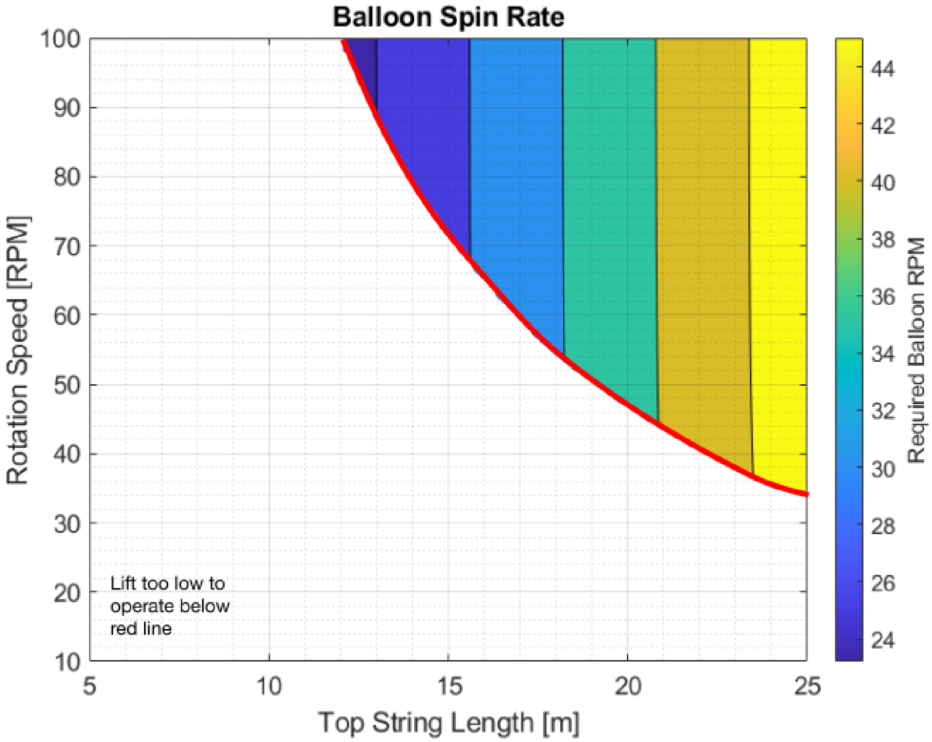

Figure 5.18: Resulting spin rate of the baseline balloon lift augmentation device (3.6 m diameter at ground level on Earth) flying at 5 km on Mars at a 1 m/s translation rate.

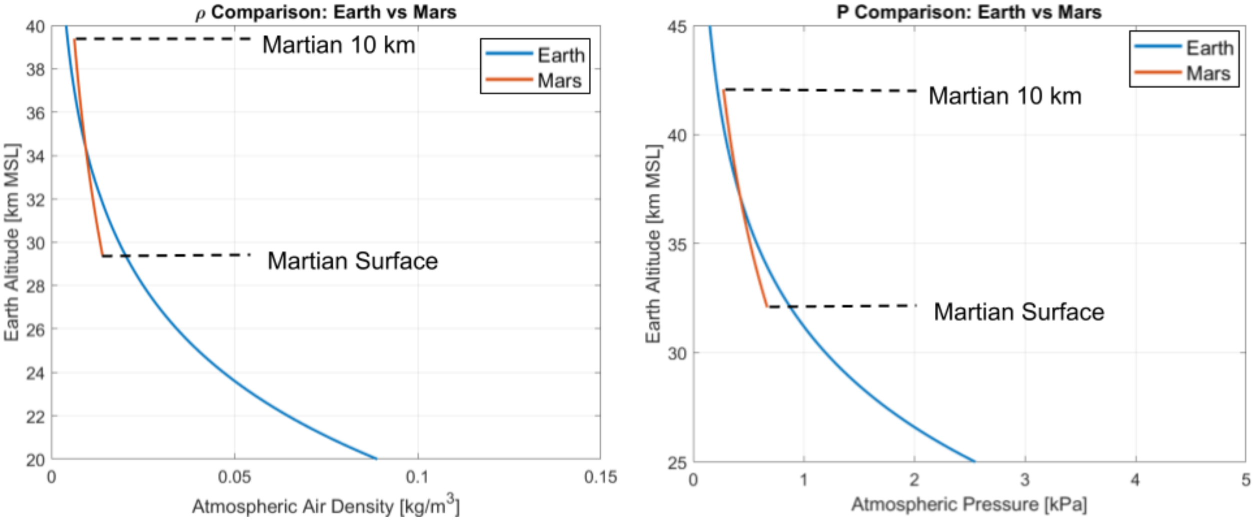

Figure 5.19: Comparison of air density (left) and air pressure (right) of Earth and Mars. Notice how the conditions of the Martian surface mimic but are not identical to those around 30 km on Earth.

5.7 Effects of Operating at Low Altitude

Exploration of a lift augmentation device's operation at lower altitudes near ground level highlights why the concept is particularly well-suited for the conditions being studied at higher altitudes above 25 km on Earth. Figures (5.20) and (5.21) show the same design trade plots for a gossamer propeller system operating at 1800 m above sea level (approximately ground level in Boulder, CO).

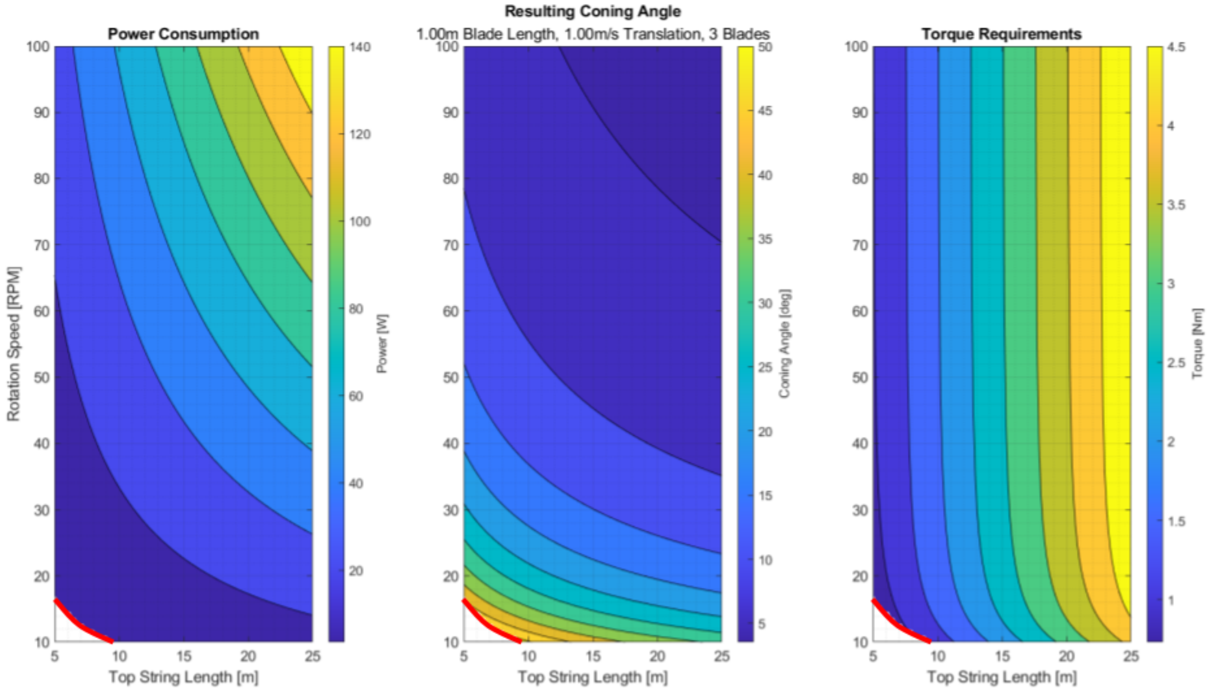

Figure 5.20: Baseline balloon (3.6 m diameter at ground level) lift augmentation device flying at ground level (such as just after release) meeting a 1 m/s translation requirement.

While the balloon itself is much smaller just after launch compared to the previous baseline plots generated at 30 km, the air density is much larger, resulting in a greater required thrust force from the gossamer propeller, requiring nearly 4 times the power and torque to achieve a 1 m/s translation.

While we saw before that the viscous drag forces scaled equally across balloon sizes at altitude, resulting in roughly equal balloon spin rates regardless of drag differences from balloon size, at low

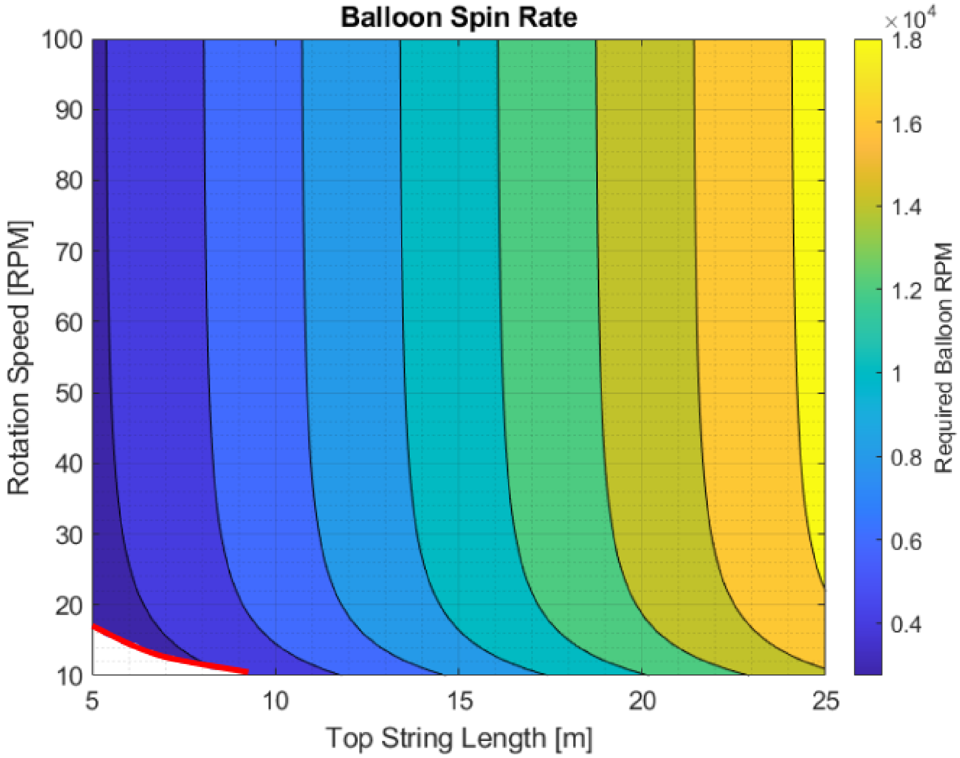

Figure 5.21: Resulting spin rate of the baseline balloon lift augmentation device (3.6 m diameter at ground level) flying at ground level (such as just after release) meeting a 1 m/s translation requirement.

altitudes this trend does not hold. At such a low altitude, the air's viscosity is two orders of magnitude lower than at 30 km, resulting in a balloon spin rate at ground level of at least 2,700 RPM and up to nearly 20,000 RPM. Such high balloon spin rates would not be achievable, limiting the devices use to higher altitudes or requiring another method, such as counter rotating blades, for producing the necessary counter torque.

5.8 Optimizations

With so many factors affecting lift augmentation and so many different applications for its use, a single optimal design likely does not exist. Rather, depending on the expected environmental conditions, balloon and payload size, and sensitivity to cost, an optimal lift augmentation system may look slightly different.

For example, if you were flying a large balloon made of a very fragile material, from Fig. (5.12), a faster spinning, shorter blade may be advantageous to keep the balloon spin rate low assuming the payload includes a method for generating 20 kW of power or more for propulsion. In contrast, if instead a large rigid balloon was used, which could take larger loads, extremely large, slow spinning blades may be more advantageous to keep power consumption low.

For a very small balloon, it is likely that payload mass would be of high importance. However, the blades themselves of a lift augmented balloon only make up a small fraction of the overall mass of the system, so larger, slower spinning blades, which balanced the balloon's ability to counter-rotate, would likely be optimal in order to keep power requirements low.

Regardless, the objective of this thesis is not to design an optimal lift augmentation system. Rather, the goal is to provide a jumping-off point for future analysis, studying and surveying a general design concept that could be widely applicable regardless of the direction of future work.

5.9 Deployment Considerations

One such piece of future work that is especially pertinent to the scalability of lift augmentation is that of deployment. Blades that are 10s of meters long would be difficult to launch without some way to store then deploy them at altitude. Even with the 2 m blade sections tested thus far (described in Ch. 4), blades tangling while trying to spin up is common. The deployment and control hardware likely take up the majority of the mass (and cost) of a full scale lift augmentation payload, so special care needs to be taken to keep it as lightweight as possible while still remaining robust to failure. A method which spools up the propeller, much like a heliogyro, would seem to be the most obvious deployment mechanism, but further testing of that idea is needed.

5.10 Scalability Summary

Given a scalability design with a number of aerodynamic assumptions, specifically that a L/D ratio of 7:1 can be achieved at 30 km, results from ground based testing have been extended first to a baseline design and then explored through variations of string length and rotor spin rate. Relaxing the L/D assumption could lead to increased drag on the rotor at high altitudes, impacting these results and requiring a full scale lift augmentation system to consume more power and counter more torque than these models indicate.

Nevertheless, the scalability model presented is an important first step in verifying that operation of a full scale system is feasible and motivates future work on refining both the model and lift augmentation design. Specifically, this model predicts much lower balloon rotation rates for countering rotor torque with viscous drag than prior models due to the rotor now operating in a lower drag configuration (only producing as much lift as is necessary to maintain the desired traverse rate). Additional study of balloon membranes under rotation stresses is needed to determine if this counter-torque concept is viable or if counter-rotating blades or some other counter-torque techniques are needed.

Chapter 6

Conclusions and Future Work

6.1 Contributions to the Field

Scientific balloons have come a long way since the first balloon flew in earnest in 1783. Since then, balloons have seen applications from directly measuring atmospheric phenomena like turbulence and aerosols, to proving rides to the upper stratosphere for drop tests of spaceflight hardware. From collecting some of the first data on the atmosphere of Venus to being an inexpensive tool for citizen science on Earth, balloons remain a critical tool in a scientist's toolbox for broadening our understanding of the world around us.

Despite their maturity compared to aircraft and satellites, balloons remain limited in their capabilities in terms of precise control over long durations, especially when cost and operational complexity are driving factors in mission design. While many forms of balloon control are available, a broadly applicable and low cost solution does not currently exist. Venting and ballast, while inexpensive, are inherently limited to a finite number of profiles. In projects like HYFLITS, this meant that a balloon can only collect data on a single descent. Longer duration forms of control, like air ballasts and differential expansion, suggest the possibility of indefinite operation but are limited to large balloons given the weight and power requirements of the pumps used to operate them. Phase changing fluids offer a pump-less alternative but require a detailed understanding of the flight environment to select the right fluid to accomplish mission goals.

Electric lift augmentation aims to provide another option for balloon control that is generally applicable to a wide range of balloons and across a large operational environment. This research explored the concept of electric lift augmentation, addressing three primary questions noted below and followed by a summary of the findings.

(1) What are some of the mission applications that could be achieved through lift augmentation?

  (a) What forms of balloon control already exist and what can be learned about them?

  Electric lift augmentation combines concepts from propellers, gossamer structures, and heliogyros, but applies them in a combination not considered before. It was found that unlike other balloon control methods explored throughout Ch. 2, electric lift augmentation is widely applicable to a range of mission types, and offers the possibility of balloon missions limited in duration not by their propulsion system but instead by the life of the balloon envelope itself. This prospect had not been previously possible in other forms of control for small latex balloons.

  (b) What are the advantages of gossamer blade lift augmentation compared to traditional altitude control techniques in the context of these missions?

  When considering specific missions and balloon classes, lift augmentation stands to have the greatest impact on small to medium balloon payloads where maximum data needs to be collected at a low cost or with relatively few flights. If a lift augmentation device were fitted to HYFLITS balloons, each flight could collect turbulence data on both ascent and descent, and payloads could perform dozens or more profiles before the latex balloons degraded. It would be like flying the same 100 flights (which currently capture 100 profiles total), but the dataset would contain over 2,400 turbulence profiles.

  Extraterrestrial ballooning is another mission class that, if sufficient risk could be reduced in the lift augmentation design, could be greatly impacted. Whether by the multiple profiles conducted by a single balloon, or by the relatively low mass and cost of the system enabling multiple balloons to be released, lift augmentation could enable new atmospheric science missions on Mars, Venus, and beyond. Previous concepts for extraterrestrial ballooning were difficult to test at scale and required large, expensive balloon systems. A lift augmented balloon could fly as a secondary payload much like the Mars Ingenuity helicopter flew secondary to the Perseverance Rover, enabling risk reduction at lower cost.

(2) In a gossamer blade with no rigid members, is it possible to achieve static stability with enough stiffness to control the blade's lift?

    (a) What would such a statically stable blade look like?

    The aerodynamic forces and moments present even in the sparse atmosphere of the stratosphere present a challenge in stabilizing propellers with no inherent stiffness. While heliogyros are able to operate against solar radiation pressure in space and remain rigid from centripetal forces alone, the gossamer blades used for lift augmentation of balloons experience aerodynamic moments not present in space. Additionally, lift and drag forces are orders of magnitude larger than solar radiation pressure, making insights from heliogyros only partially applicable.

    A unique way of rigging the string of the gossamer blade, the 4-bar link, results in natural static stability, something that remained elusive in early tests. Discovery, proof, and validation of this stability were instrumental in continuing work on characterizing the performance of the gossamer blades, and marked a turning point in the development of the test rig. Prior to this work, terrestrial or atmospheric gossamer blades without rigidizing members have never been used, likely in part due to their lack of stiffness. The 4-bar link rigging method directly solves this problem and results in a stiff, stable structure that can be made extremely large while remaining lightweight. Such a structure was critical in the testing for lift augmentation of balloons and enables future work on the concept from a statically stable baseline.

    (b) How can the performance of a gossamer blade be measured?

A method of determining the lift and drag on the blade section was derived from a force balance between the tension in the strings and the centripetal and gravity forces on the tip. Two ways of determining tip location were explored and compared, with a blade depth method allowing for estimates of the lift distribution across the blade and a tip tracking method enabling blades of arbitrary geometry to be studied.

While this research found the blade billow takes the form of a catenary, the test rig allows for evaluation of blades of any shape and lift distribution. This means blades with non-uniform lift distributions can be studied, or the catenary assumptions can be further verified by designing blades optimized for uniform lift. This measurement technique is unique in that the lift and drag forces on the blade section can be determined from photogrammetry alone. Typical flexible membrane experiments only use optical methods to determine the membrane shape, opting to use separate force transducers to measure the aerodynamic loads.

(3) What are some of the flight regimes and balloon configurations where this concept could be applied?

   (a) How and why does the lift augmentation strategy work in these conditions?

   Initial scalability models were built with the knowledge gained from the ground-based, scaled test campaigns. While relying on performance assumptions of low Reynolds number aerodynamics, namely that a lift to drag ratio of 7 can be achieved, this research represents the first step towards a full scale lift augmentation prototype and shows that such a device can be practical.

   Such modeling is critical, as with the current test rig, achieving the coning angles predicted at altitude is near impossible due to the much stronger aerodynamic forces at ground level. While physical testing at a small scale was critical to developing these models, much could be gained by testing a larger device at a higher altitude.

   (b) What design considerations might there be for different types of balloons and mission objectives?

Optimal designs were explored, with a precise definition of what it means to be an "optimal" lift augmentation design being highly dependent on the mission objectives and system limitations. In small balloons where payload mass is extremely limited, larger blades seem optimal as the blades themselves contribute little mass due to their gossamer construction while rotor speeds can be kept low for lower power consumption. Conversely, on larger balloons, many different blade sizes could make sense depending on mission requirements.

In operations on Mars, similar results were found compared to Earth's stratosphere, though the results are more sensitive to string length due to a reduction in gravity and the effects of spinning the tip mass. Regardless, unlike many other forms of control, the atmospheric conditions of interest to the operation of a lift augmentation device in the stratosphere closely mimic that of Mars, proving a rare testing environment that closely mimics that of the real thing.

6.2 Future Work

Determining feasibility and general performance expectations is an important first step in any new design concept, and future work in electric lift augmentation can go in many different directions. From a theoretical standpoint, the current work relies on many assumptions regarding the aerodynamic performance of thin, flexible blades in the low Reynolds number environment of the Stratosphere. Additional effort should go into challenging those assumptions and improving on the performance expectations of a full scale device. The elliptical tip extensions, while intended to reduce the effects of tip vortices, do complicate comparisons between tests and models. Effects from these tips, or any other form of tip extension need to be added to the theoretical models to fully understand the contributions of the gossamer propellers.

While placing instruments on the tips of the gossamer blades is theorized to allow for disturbance-free measurements, a better understanding of how the blades interact with each other is needed to confirm this. The wake from the balloon also remains an uncertainty. Is it enough to use gossamer propellers that are larger than the balloon's diameter to ensure wake-free measurements? Computational fluid dynamics models present a promising path forward to address these problems.

Controllability, specifically of the blade tips and how exactly that influences the billow of the blades can also be further explored. This has implications for aerodynamic performance as well. The current test rig has the capability for measuring and dynamically changing the string length, so incorporating feedback from the blade tip location or other means could allow for finer control of the propeller, including damping from environmental disturbances.

From an applied engineering perspective, the advantages of "simply" flying a full scale prototype and analyzing the results cannot be understated. Comparisons between test data and models can be made and verified in ways not yet possible. However, a number of problems still stand in the way of a full scale prototype. First, deployment of the strings remains a challenge even at reduced scales in controlled environments. The idea of spinning the balloon to counter rotor torque with viscous drag should be explored, as blade deployment may be complicated by counter-rotating blades. Feedback of tip position is also critical for an operational gossamer propeller, as that is the mechanism by which prescribed augmented lifting forces can be applied to the balloon system. Additional work on the data collection and processing architecture will be needed, as the current prototypes are designed for data collection and post-processing, not processing in real-time.

Finally, and more generally, refinements to the V5 test rig detailed in Ch. 4 and Appendix A could enable future testing of new types of flexible airfoils where remote measurement is critical, with changes in tip mass contributing to changes in measurement sensitivity due to the balance between the gravity, centripetal, and aerodynamic loads (transferred to the tip through string tension). While the exact impacts from tip mass are not immediately clear even from Eq. 4.10 due to the dependence of mass in the blade's coning angle (which is a measured, not derived, quantity), it would be expected that a smaller tip mass would cause aerodynamic forces to have a greater effect on tip position, amplifying both the gossamer propeller's lift and drag as well as any disturbances. Further investigation into the behavior of billowed airfoils can be conducted, and the catenary assumptions applied in this research can be tested and improved. Billow shapes for other lift distributions could be derived and verified.

Bibliography

[1] Kim Aaron, Matthew Heun, and Kerry Nock. Balloon trajectory control. In International Balloon Technology Conference, Balloon Systems Conferences. American Institute of Aeronautics and Astronautics, June 1999.

[2] K.M. Aaron, M.K. Heun, and K.T. Nock. A method for balloon trajectory control. Advances in Space Research, 30(5):1227–1232, 2002.

[3] Bianca Baier, Colm Sweeney, Jack Higgs, Timothy Newberger, Sonja Wolter, Steven Borenstein, and Brian Argrow. The NOAA High-altitude Operational Return Uncrewed System (HORUS) for Atmospheric Observing. 2021:A11C–01, December 2021. Conference Name: AGU Fall Meeting Abstracts ADS Bibcode: 2021AGUFM.A11C..01B.

[4] Bob Balaram, Timothy Canham, Courtney Duncan, Håvard F. Grip, Wayne Johnson, Justin Maki, Amelia Quon, Ryan Stern, and David Zhu. Mars Helicopter Technology Demonstrator. In 2018 AIAA Atmospheric Flight Mechanics Conference, AIAA SciTech Forum. American Institute of Aeronautics and Astronautics, January 2018.

[5] Richard E. Bellman. Dynamic Programming. Princeton Landmarks in Mathematics and Physics. Princeton University Press, 1957.

[6] Richard Blomquist, William Whittaker, Dimitrios Chair, George Apostolopoulos, Andreas Kantor, and Von Flotow. Heliogyro Control. April 2009.

[7] Tim Burdett, Jason Gregg, and Kenneth Van Treuren. An Examination of the Effect of Reynolds Number on Airfoil Performance. pages 2203–2213. American Society of Mechanical Engineers Digital Collection, March 2012.

[8] David Cease, Nolan Ferguson, Braden Barkemeyer, Ryan Lansdon, Kelly Crombie, Jacob Marvin, Jared Dempewolf, Kyle McGue, Tyler Faragallah, and Paolo Wilczak. High Altitude Lifting Orbiter (HALO) Project Final Report. page 94, May 2020.

[9] E. Chassefière, O. Korablev, T. Imamura, K. H. Baines, C. F. Wilson, D. V. Titov, K. L. Aplin, T. Balint, J. E. Blamont, C. G. Cochrane, Cs. Ferencz, F. Ferri, M. Gerasimov, J. J. Leitner, J. Lopez-Moreno, B. Marty, M. Martynov, S. V. Pogrebenko, A. Rodin, J. A. Whiteway, and L. V. Zasova. European Venus Explorer: An in-situ mission to Venus using a balloon platform. Advances in Space Research, 44(1):106–115, July 2009.

[10] SPIDER Collaboration, P. A. R. Ade, M. Amiri, S. J. Benton, A. S. Bergman, R. Bihary, J. J. Bock, J. R. Bond, J. A. Bonetti, S. A. Bryan, H. C. Chiang, C. R. Contaldi, O. Doré, A. J. Duivenvoorden, H. K. Eriksen, M. Farhang, J. P. Filippini, A. A. Fraisse, K. Freese, M. Galloway, A. E. Gambrel, N. N. Gandilo, K. Ganga, R. Gualtieri, J. E. Gudmundsson, M. Halpern, J. Hartley, M. Hasselfield, G. Hilton, W. Holmes, V. V. Hristov, Z. Huang, K. D. Irwin, W. C. Jones, A. Karakci, C. L. Kuo, Z. D. Kermish, J. S.-Y. Leung, S. Li, D. S. Y. Mak, P. V. Mason, K. Megerian, L. Moncelsi, T. A. Morford, J. M. Nagy, C. B. Netterfield, M. Nolta, R. O'Brient, B. Osherson, I. L. Padilla, B. Racine, A. S. Rahlin, C. Reintsema, J. E. Ruhl, M. C. Runyan, T. M. Ruud, J. A. Shariff, E. C. Shaw, C. Shiu, J. D. Soler, X. Song, A. Trangsrud, C. Tucker, R. S. Tucker, A. D. Turner, J. F. van der List, A. C. Weber, I. K. Wehus, S. Wen, D. V. Wiebe, and E. Y. Young. A Constraint on Primordial B-Modes from the First Flight of the SPIDER Balloon-Borne Telescope, March 2021. arXiv:2103.13334 [astro-ph].

[11] Sarah M. Cook and D. A. Lawrence. Sensitivity of a physically realizable heliogyro root pitch control system to inherent damping models | Elsevier Enhanced Reader, 2021.

[12] Sarah M. Cook, Dale A. Lawrence, Jerry E. Warren, and W. Keats Wilkie. Improved Modal Damping Characterization for Small-Scale Heliogyro Blades. Journal of Spacecraft and Rockets, 57(4):642–655, 2020. Publisher: American Institute of Aeronautics and Astronautics _eprint: https://doi.org/10.2514/1.A34518.

[13] Qiumin Dai, Xiande Fang, Xiaojian Li, and Lili Tian. Performance simulation of high altitude scientific balloons | Elsevier Enhanced Reader, December 2011.

[14] R. E. Danielson, J. E. Gaustad, M. Schwarzschild, H. F. Weaver, and N. J. Woolf. SYMPOSIUM ON INSTRUMENTAL ASTRONOMY: Mars observations from Stratoscope II. The Astronomical Journal, 69:344, June 1964.

[15] R. E. Danielson, M. G. Tomasko, and B. D. Savage. High-resolution imagery of Uranus obtained by Stratoscope 2. Technical Report NASA-CR-132024, June 1972. NTRS Author Affiliations: Princeton Univ. Observatory NTRS Document ID: 19730015119 NTRS Research Center: Legacy CDMS (CDMS).

[16] G. de Matteis and L. de Sociot. Nonlinear aerodynamics of a two-dimensional membrane airfoil with separation. Journal of Aircraft, 23(11):831–836, November 1986. Publisher: American Institute of Aeronautics and Astronautics.

[17] A. Doerenbecher, C. Basdevant, P. Drobinski, P. Durand, C. Fesquet, F. Bernard, P. Cocquerez, N. Verdier, and A. Vargas. Low-Atmosphere Drifting Balloons: Platforms for Environment Monitoring and Forecast Improvement. Bulletin of the American Meteorological Society, 97(9):1583–1599, September 2016. Publisher: American Meteorological Society Section: Bulletin of the American Meteorological Society.

[18] Huafei Du, Mingyun Lv, Jun Li, Weiyu Zhu, Lanchuan Zhang, and Yifei Wu. Station-keeping performance analysis for high altitude balloon with altitude control system. Aerospace Science and Technology, 92:644–652, September 2019.

[19] Cuyler Dull, Lauren Wagner, Larry Young, and Wayne Johnson. Hover and Forward Flight Performance Modeling of the Ingenuity Mars Helicopter. San Jose, CA, 2022. NTRS Au-

thor Affiliations: Science and Technology Corporation (United States), Ames Research Center NTRS Document ID: 20210026235 NTRS Research Center: Ames Research Center (ARC).

[20] E.H. LOCKWOOD. A BOOK OF CURVES. CAMBRIDGE UNIVERSITY PRESS, 1961.

[21] Richard Eppler and Dan M. Somers. Aerodynamic Design of a Propeller for High-Altitude Balloon Trajectory Control. Technical Report GSFC.CR.7502.2012, March 2012. NTRS Author Affiliations: Technische Hochschule, Airfoils, Inc. NTRS Document ID: 20130000746 NTRS Research Center: Goddard Space Flight Center (GSFC).

[22] FAI. Press Release - FAI Ballooning Commission Annual Conference, May 2008.

[23] Rodger Farley. BalloonAscent: 3-D Simulation Tool for the Ascent and Float of High-Altitude Balloons. In AIAA 5th ATIO and16th Lighter-Than-Air Sys Tech. and Balloon Systems Conferences, Aviation Technology, Integration, and Operations (ATIO) Conferences. American Institute of Aeronautics and Astronautics, September 2005.

[24] Emily Feng and Lexie Schapitl. How a Chinese 'spy balloon' prompted the U.S. to scour the skies. NPR, February 2023.

[25] P. D. Fleming and S. D. Probert. Design and performance of a small shrouded cretan windwheel. Applied Energy, 10(2):121–139, February 1982.

[26] M. Fulchignoni, A. Aboudan, F. Angrilli, M. Antonello, S. Bastianello, C. Bettanini, G. Bianchini, G. Colombatti, F. Ferri, E. Flamini, V. Gaborit, N. Ghafoor, B. Hathi, A. M. Harri, A. Lehto, P. F. Lion Stoppato, M. R. Patel, and J. C. Zarnecki. A stratospheric balloon experiment to test the Huygens atmospheric structure instrument (HASI). Planetary and Space Science, 52(9):867–880, August 2004.

[27] A. Gallice, F. G. Wienhold, C. R. Hoyle, F. Immler, and T. Peter. Modeling the ascent of sounding balloons: derivation of the vertical air motion. Atmospheric Measurement Techniques, 4(10):2235–2253, October 2011. Publisher: Copernicus GmbH.

[28] Terry Gamber, Kerry Nock, J. Balaram, Matthew Heun, I. Smith, Kerry Nock, J. Balaram, Matthew Heun, I. Smith, and Terry Gamber. Mars 2001 Aerobot/Balloon System overview. In International Balloon Technology Conference, Balloon Systems Conferences. American Institute of Aeronautics and Astronautics, June 1997.

[29] Alexander Gehrke, Jules Richeux, Esra Uksul, and Karen Mulleners. Aeroelastic characterisation of a bio-inspired flapping membrane wing. Bioinspiration & Biomimetics, 17(6):065004, September 2022. Publisher: IOP Publishing.

[30] Marija Gimbutas. The goddesses and gods of Old Europe, 6500-3500 BC : myths and cult images. London : Thames and Hudson, 1982.

[31] Joseph B. Habeck, Christopher J. Hogan, James A. Flaten, and Graham V. Candler. Development of a calibration system for measuring aerosol particles in the stratosphere. In AIAA SCITECH 2022 Forum, AIAA SciTech Forum. American Institute of Aeronautics and Astronautics, December 2021.

[32] Thomas F. Heinsheimer, Robyn C. Friend, and Neil G. Siegel. Concepts for autonomous flight control for a balloon on Mars. October 1988. NTRS Author Affiliations: Titan Systems, Inc., Gardena, Siegel, Neil G., Redondo Beach NTRS Document ID: 19890006229 NTRS Research Center: Legacy CDMS (CDMS).

[33] Hui Hu, Masatoshi Tamai, and Jeffery T. Murphy. Flexible-Membrane Airfoils at Low Reynolds Numbers. Journal of Aircraft, 45(5):1767–1778, 2008. Publisher: American Institute of Aeronautics and Astronautics _eprint: https://doi.org/10.2514/1.36438.

[34] Yoshifumi Inatani, Nobuaki Ishii, Koju Hiraki, Motoki Hinada, Takashi Nakajima, Nobuyuki Yajima, Masahisa Honda, Takashi Makino, Yoshifumi Inatani, Nobuaki Ishii, Koju Hiraki, Motoki Hinada, Takashi Nakajima, Nobuyuki Yajima, Masahisa Honda, and Takashi Makino. Parachute deployment experiment for a small capsule dropped from a balloon. In 14th Aerodynamic Decelerator Systems Technology Conference, Aerodynamic Decelerator Systems Technology Conferences. American Institute of Aeronautics and Astronautics, June 1997.

[35] N. Izutsu, N. Yajima, H. Honda, and T. Imamura. Venus balloons using water vapor. Advances in Space Research, 33(10):1831–1835, January 2004.

[36] N. Izutsu, N. Yajima, H. Honda, and T. Imamura. Venus balloons using water vapor. Advances in Space Research, 33(10):1831–1835, January 2004.

[37] Christopher H.M Jenkins. Gossamer Spacecraft: Membrane And Inflatable Structures Technology For Space Applications. American Institute of Aeronautics and Astronautics, Reston ,VA, 2001. _eprint: https://arc.aiaa.org/doi/pdf/10.2514/4.866616.

[38] Les Johnson, Roy Young, Edward Montgomery, and Dean Alhorn. Status of solar sail technology within NASA. Advances in Space Research, 48(11):1687–1694, December 2011.

[39] Andrew Jones. China conducts parachute tests for asteroid sample return mission, June 2023.

[40] Claude Kansaku, Linda Kehr, and Catherine Lanier. Stem Related K 12 Outreach Through High Altitude Balloon Program Collaborations. pages 12.1301.1–12.1301.14, June 2007. ISSN: 2153-5965.

[41] James Keogh, Tracie Barber, Sammy Diasinos, and Graham Doig. Techniques for Aerodynamic Analysis of Cornering Vehicles. pages 2015–01–0022, March 2015.

[42] V. V. Kerzhanovich, J. A. Cutts, H. W. Cooper, J. L. Hall, B. A. McDonald, M. T. Pauken, C. V. White, A. H. Yavrouian, A. Castano, H. M. Cathey, D. A. Fairbrother, I. S. Smith, C. M. Shreves, T. Lachenmeier, E. Rainwater, and M. Smith. Breakthrough in Mars balloon technology. Advances in Space Research, 33(10):1836–1841, January 2004.

[43] Chris Koehler. Balloonsat: Missions to the Edge of Space. Small Satellite Conference, August 2002.

[44] Witold J. F. Koning, Wayne Johnson, and Brian G. Allan. Generation of Mars Helicopter Rotor Model for Comprehensive Analyses. San Francisco, CA, January 2018. NTRS Author Affiliations: Science and Technology Corp., NASA Ames Research Center, NASA Langley Research Center NTRS Report/Patent Number: ARC-E-DAA-TN50660 NTRS Document ID: 20180008645 NTRS Research Center: Ames Research Center (ARC).

[45] Stefanie Kremser, Larry W. Thomason, Marc von Hobe, Markus Hermann, Terry Deshler, Claudia Timmreck, Matthew Toohey, Andrea Stenke, Joshua P. Schwarz, Ralf Weigel, Stephan Fueglistaler, Fred J. Prata, Jean-Paul Vernier, Hans Schlager, John E. Barnes, Juan-Carlos Antuña-Marrero, Duncan Fairlie, Mathias Palm, Emmanuel Mahieu, Justus Notholt, Markus Rex, Christine Bingen, Filip Vanhellemont, Adam Bourassa, John M. C. Plane, Daniel Klocke, Simon A. Carn, Lieven Clarisse, Thomas Trickl, Ryan Neely, Alexander D. James, Landon Rieger, James C. Wilson, and Brian Meland. Stratospheric aerosol—Observations, processes, and impact on climate. Reviews of Geophysics, 54(2):278–335, 2016. _eprint: https://onlinelibrary.wiley.com/doi/pdf/10.1002/2015RG000511.

[46] Swathi Krishna, Melissa A. Green, and Karen Mulleners. Flowfield and Force Evolution for a Symmetric Hovering Flat-Plate Wing. AIAA Journal, 56(4):1360–1371, 2018. Publisher: American Institute of Aeronautics and Astronautics _eprint: https://doi.org/10.2514/1.J056468.

[47] Andreas Kräuchi, Rolf Philipona, Gonzague Romanens, Dale F. Hurst, Emrys G. Hall, and Allen F. Jordan. Controlled weather balloon ascents and descents for atmospheric research and climate monitoring. Atmospheric Measurement Techniques, 9(3):929–938, March 2016. Publisher: Copernicus GmbH.

[48] Vincent E. Lally. The radiation controlled balloon (RACOON). Advances in Space Research, 3(6):19–24, January 1983.

[49] Dan Lamothe. U.S. releases photo of Chinese balloon captured by U-2 spy plane. Washington Post, February 2023.

[50] Geoffrey Landis. Low-Altitude Exploration of the Venus Atmosphere by Balloon. In 48th AIAA Aerospace Sciences Meeting Including the New Horizons Forum and Aerospace Exposition, Aerospace Sciences Meetings. American Institute of Aeronautics and Astronautics, January 2010.

[51] Shane L. Larson, John C. Armstrong, and William A. Hiscock. The first frontier: High altitude ballooning as a platform for student research experiences in science and engineering. American Journal of Physics, 77(6):489–497, June 2009.

[52] Dale A. Lawrence, Brian Argrow, Joseph L. Pointer, Nicholas Kenny, Christopher A. Roseman, James Flaten, Graham V. Candler, Aroh Barjatya, and Julio Guardado. In-situ Turbulence and Particulate Measurements in Support of the BOLT II Flight Experiment. In AIAA SCITECH 2023 Forum. American Institute of Aeronautics and Astronautics. _eprint: https://arc.aiaa.org/doi/pdf/10.2514/6.2023-0480.

[53] Paul LeBlanc. Everything you need to know about the suspected Chinese spy balloon | CNN Politics, February 2023.

[54] U. Lei, C. Y. Yang, and K. C. Wu. Viscous torque on a sphere under arbitrary rotation. Applied Physics Letters, 89(18):181908, October 2006. Publisher: American Institute of Physics.

[55] J. Lelieveld, P. J. Crutzen, V. Ramanathan, M. O. Andreae, C. A. M. Brenninkmeijer, T. Campos, G. R. Cass, R. R. Dickerson, H. Fischer, J. A. de Gouw, A. Hansel, A. Jefferson, D. Kley, A. T. J. de Laat, S. Lal, M. G. Lawrence, J. M. Lobert, O. L. Mayol-Bracero, A. P. Mitra,

T. Novakov, S. J. Oltmans, K. A. Prather, T. Reiner, H. Rodhe, H. A. Scheeren, D. Sikka, and J. Williams. The Indian Ocean Experiment: Widespread Air Pollution from South and Southeast Asia. Science, 291(5506):1031–1036, February 2001. Publisher: American Association for the Advancement of Science.

[56] Tianshu Liu, Akira Oyama, and Kozo Fujii. Scaling Analysis of Propeller-Driven Aircraft for Mars Exploration. Journal of Aircraft, 50(5):1593–1604, September 2013.

[57] E. Loth. Drag of non-spherical solid particles of regular and irregular shape. Powder Technology, 182(3):342–353, March 2008.

[58] Yutaka Masuyama, Yusuke Tahara, Toichi Fukasawa, and Naotoshi Maeda. Database of sail shapes versus sail performance and validation of numerical calculations for the upwind condition. Journal of Marine Science and Technology, 14(2):137–160, June 2009.

[59] Larry Matthies. Titan Aerial Daughtercraft. 2014.

[60] Daniel J. McCarthy. Operating Characteristics of the Stratoscope II Balloon-Borne Telescope. IEEE Transactions on Aerospace and Electronic Systems, AES-5(2):323–329, March 1969. Conference Name: IEEE Transactions on Aerospace and Electronic Systems.

[61] J. H. Mcmasters and M. L. Henderson. Low-speed single-element airfoil synthesis. January 1979. NTRS Author Affiliations: Boeing Commercial Airplane Co. NTRS Document ID: 19790015719 NTRS Research Center: Legacy CDMS (CDMS).

[62] Robert Mitcheltree, Robin Bruno, Eric Slimko, Curtis Baffes, Edward Konefat, and Al Witkowski. High Altitude Test Program for a Mars Subsonic Parachute. In 18th AIAA Aerodynamic Decelerator Systems Technology Conference and Seminar. American Institute of Aeronautics and Astronautics. _eprint: https://arc.aiaa.org/doi/pdf/10.2514/6.2005-1659.

[63] Marc J. M. Mulkens and Albert O. Ormerod. Measurements of aerodynamic rotary stability derivatives using a whirling arm facility. Journal of Aircraft, May 2012.

[64] D. M. Murphy. Validation of a Scalable Solar Sailcraft. Monterey, CA, January 2006. NTRS Author Affiliations: ATK Space Systems NTRS Document ID: 20060004997 NTRS Research Center: Marshall Space Flight Center (MSFC).

[65] NASA. U.S. Standard Atmosphere, 1976. Technical Report NOAA-S/T-76-1562, October 1976. NTRS Document ID: 19770009539 NTRS Research Center: Legacy CDMS (CDMS).

[66] Barry G. Newman. Aerodynamic theory for membranes and sails. Progress in Aerospace Sciences, 24(1):1–27, January 1987.

[67] Brett Newman. Propeller Analysis and Synthesis for Ultra-Long Duration Balloon Trajectory Steering. In AIAA 5th ATIO and16th Lighter-Than-Air Sys Tech. and Balloon Systems Conferences, Aviation Technology, Integration, and Operations (ATIO) Conferences. American Institute of Aeronautics and Astronautics, September 2005.

[68] J. N. Nielsen. Theory of Flexible Aerodynamic Surfaces. Journal of Applied Mechanics, 30(3):435–442, September 1963.

[69] K Nock, K Aaron, J Jones, D McGee, G Powell, A Yavrouian, and J Wu. Balloon ALtItude Control Experiment (ALICE) project. In 11th Lighter-than-Air Systems Technology Conference, Lighter-Than-Air Conferences. American Institute of Aeronautics and Astronautics, May 1995.

[70] Jean-Baptiste Renard, François Dulac, Gwenaël Berthet, Thibaut Lurton, Damien Vignelles, Fabrice Jégou, Thierry Tonnelier, Matthieu Jeannot, Benoit Couté, Rony Akiki, Nicolas Verdier, Marc Mallet, François Gensdarmes, Patrick Charpentier, Samuel Mesmin, Vincent Duverger, Jean-Charles Dupont, Thierry Elias, Vincent Crenn, Jean Sciare, Paul Zieger, Matthew Salter, Tjarda Roberts, Jérôme Giacomoni, Matthieu Gobbi, Eric Hamonou, Haraldur Olafsson, Pavla Dagsson-Waldhauserova, Claude Camy-Peyret, Christophe Mazel, Thierry Décamps, Martin Piringer, Jérémy Surcin, and Daniel Daugeron. LOAC: a small aerosol optical counter/sizer for ground-based and balloon measurements of the size distribution and nature of atmospheric particles – Part 1: Principle of measurements and instrument evaluation. Atmospheric Measurement Techniques, 9(4):1721–1742, April 2016. Publisher: Copernicus GmbH.

[71] Reuters. Explainer: What we know and don't know about the Chinese balloon. Reuters, February 2023.

[72] Peter C. E. Roberts and Patrick G. Harkness. Drag Sail for End-of-Life Disposal from Low Earth Orbit. Journal of Spacecraft and Rockets, 44(6):1195–1203, November 2007. Publisher: American Institute of Aeronautics and Astronautics.

[73] L. Javier Romualdez, Steven J. Benton, Anthony M. Brown, Paul Clark, Christopher J. Damaren, Tim Eifler, Aurelien A. Fraisse, Mathew N. Galloway, Ajay Gill, John W. Hartley, Bradley Holder, Eric M. Huff, Mathilde Jauzac, William C. Jones, David Lagattuta, Jason S.-Y. Leung, Lun Li, Thuy Vy T. Luu, Richard J. Massey, Jacqueline McCleary, James Mullaney, Johanna M. Nagy, C. Barth Netterfield, Susan Redmond, Jason D. Rhodes, Jürgen Schmoll, Mohamed M. Shaaban, Ellen Sirks, and Sut-Ieng Tam. Robust diffraction-limited near-infrared-to-near-ultraviolet wide-field imaging from stratospheric balloon-borne platforms—Super-pressure Balloon-borne Imaging Telescope performance. Review of Scientific Instruments, 91(3):034501, March 2020.

[74] Christopher A. Roseman, Dale A. Lawrence, Joseph L. Pointer, Steve Borenstein, and Brian M. Argrow. A Low-Cost Balloon System for High-Cadence, In-Situ Stratospheric Turbulence Measurements. In AIAA AVIATION 2021 FORUM, AIAA AVIATION Forum. American Institute of Aeronautics and Astronautics, July 2021.

[75] R. Z. Sagdeev, V. M. Linkin, J. E. Blamont, and R. A. Preston. The VEGA Venus Balloon Experiment. Science, 231(4744):1407–1408, March 1986. Publisher: American Association for the Advancement of Science.

[76] Erfan Salami, Thomas A Ward, Elham Montazer, and Nik Nazri Nik Ghazali. A review of aerodynamic studies on dragonfly flight. Proceedings of the Institution of Mechanical Engineers, Part C: Journal of Mechanical Engineering Science, 233(18):6519–6537, September 2019. Publisher: IMECHE.

[77] Sherif Saleh and Weiliang He. New design simulation for a high-altitude dual-balloon system to extend lifetime and improve floating performance. Chinese Journal of Aeronautics, 31(5):1109–1118, May 2018.

[78] Miguel San Martin, Berenice Mettler, Brian Allan, Larry Young, Milan Mandic, Daniel P. Scharf, Carlos Malpica, Wayne Johnson, Havard Fjaer Grip, Berenice Mettler, Brian Allan, Larry Young, Milan Mandic, Daniel P. Scharf, Carlos Malpica, Wayne Johnson, and Havard Fjaer Grip. Flight Dynamics of Mars Helicopter. September 2017. Publisher: Pasadena, CA: Jet Propulsion Laboratory, National Aeronautics and Space Administration, 2017.

[79] Davi Santos, Andouglas G. Silva Junior, Alvaro Negreiros, João Vilas Boas, Justo Alvarez, Andre Araujo, Rafael Vidal Aroca, and Luiz M. G. Gonçalves. Design and Implementation of a Control System for a Sailboat Robot. Robotics, 5(1):5, March 2016. Number: 1 Publisher: Multidisciplinary Digital Publishing Institute.

[80] sky s. Standard Atmosphere Functions, October 2021. original-date: 2017-07-03T17:46:08Z.

[81] Rick Smith and Wei Shyy. Computation of aerodynamic coefficients for a flexible membrane airfoil in turbulent flow: A comparison with classical theory. Physics of Fluids, 8(12):3346–3353, December 1996. Publisher: American Institute of Physics.

[82] Arnold Song, Xiaodong Tian, Emily Israeli, Ricardo Galvao, Kristin Bishop, Sharon Swartz, and Kenneth Breuer. Aeromechanics of Membrane Wings with Implications for Animal Flight. AIAA Journal, 46(8):2096–2106, August 2008. Publisher: American Institute of Aeronautics and Astronautics.

[83] Shigeru Sunada, Akitoshi Sakaguchi, and Keiji Kawachi. Airfoil Section Characteristics at a Low Reynolds Number. Journal of Fluids Engineering, 119(1):129–135, March 1997.

[84] Andrey Sushko, Aria Tedjarati, Joan Creus-Costa, Sasha Maldonado, Kai Marshland, and Marco Pavone. Low cost, high endurance, altitude-controlled latex balloon for near-space research (ValBal). In 2017 IEEE Aerospace Conference, pages 1–9, March 2017.

[85] Jian Tang, Dragos Viieru, and Wei Shyy. A Study of Aerodynamics of Low Reynolds Number Flexible Airfoils. In 37th AIAA Fluid Dynamics Conference and Exhibit, Fluid Dynamics and Co-located Conferences. American Institute of Aeronautics and Astronautics, June 2007.

[86] A. Theuerkauf, M. Gerding, and F.-J. Lübken. LITOS – a new balloon-borne instrument for fine-scale turbulence soundings in the stratosphere. Atmospheric Measurement Techniques, 4(1):55–66, January 2011. Publisher: Copernicus GmbH.

[87] B. Thwaites and George Frederick James Temple. The aerodynamic theory of sails. I. Two-dimensional sails. Proceedings of the Royal Society of London. Series A. Mathematical and Physical Sciences, 261(1306):402–422, 1961. Publisher: Royal Society.

[88] NOAA US Department of Commerce. Radiosonde Observation. Publisher: NOAA's National Weather Service.

[89] Paul B. Voss, Emily E. Riddle, and Michael S. Smith. Altitude Control of Long-Duration Balloons. Journal of Aircraft, 42(2):478–482, March 2005.

[90] Rye M. Waldman and Kenneth S. Breuer. Camber and aerodynamic performance of compliant membrane wings. Journal of Fluids and Structures, 68:390–402, January 2017.

[91] Junhong Wang, Jianchun Bian, William O. Brown, Harold Cole, Vanda Grubišić, and Kate Young. Vertical Air Motion from T-REX Radiosonde and Dropsonde Data. Journal of Atmospheric and Oceanic Technology, 26(5):928–942, May 2009. Publisher: American Meteorological Society Section: Journal of Atmospheric and Oceanic Technology.

[92] Bong Wie and David Murphy. AOCS Performance and Stability Validation for a 160-m Solar Sail with Control-Structure Interactions. NTRS Author Affiliations: Arizona State Univ., ATK Space Systems NTRS Meeting Information: 41st AIAA Joint Propulsion Conference; 2005-07-10 to 2005-07-13; undefined NTRS Document ID: 20050207361 NTRS Research Center: Marshall Space Flight Center (MSFC), June 2005.

[93] W. Keats Wilkie, Jerry E. Warren, Daniel V. Guerrant, Dale A. Lawrence, S. Chad Gibbs, Earl H. Dowell, Andrew F. Heaton, Andrew F. Heaton, Jer-Nan Juang, Lucas G. Horta, Karen H. Lyle, Justin D. Littell, Robert G. Bryant, Mark W. Thomson, and Phillip E. Walkemeyer. Heliogyro Solar Sail Research at NASA. Glasgow, June 2013. NTRS Author Affiliations: NASA Langley Research Center, Colorado Univ., Duke Univ., NASA Marshall Space Flight Center, Jet Propulsion Lab., California Inst. of Tech. NTRS Report/Patent Number: NF1676L-16171 NTRS Document ID: 20130014933 NTRS Research Center: Langley Research Center (LaRC).

[94] William K. Wilkie. Overview of the NASA Advanced Composite Solar Sail System (ACS3) Technology Demonstration Project. In AIAA Scitech 2021 Forum, AIAA SciTech Forum. American Institute of Aeronautics and Astronautics, January 2021.

[95] William K. Wilkie, Jerry E. Warren, M. W. Thompson, P. D. Lisman, P. E. Walkemeyer, D. V. Guerrant, and D. A. Lawrence. The Heliogyro Reloaded. Huntsville, AL, December 2011. NTRS Author Affiliations: NASA Langley Research Center, Jet Propulsion Lab., California Inst. of Tech., Colorado Univ. NTRS Report/Patent Number: NF1676L-12976 NTRS Document ID: 20110023680 NTRS Research Center: Langley Research Center (LaRC).

[96] Justin Winslow, Hikaru Otsuka, Bharath Govindarajan, and Inderjit Chopra. Basic Understanding of Airfoil Characteristics at Low Reynolds Numbers (104–105). Journal of Aircraft, 55(3):1050–1061, 2018. Publisher: American Institute of Aeronautics and Astronautics _eprint: https://doi.org/10.2514/1.C034415.

[97] N. Yajima, N. Izutsu, and H. Honda. Structure variations of pumpkin balloon. Advances in Space Research, 33(10):1694–1699, January 2004.

Appendix A

V5 Test Rig User Manual

While initially starting as a simple ceiling fan, the gossamer propeller test rig has grown in complexity greatly over the five major revisions and countless minor upgrades undertaken since the beginning. This appendix will serve as a "User Manual" for the current version of the rig for continued testing. Figure (A.1) labels major parts of the "flight side" of the test rig. This can be installed like any other ceiling fan, and as of August 2023, the ASPEN Lab already has a mount on the ceiling near the middle of the room.

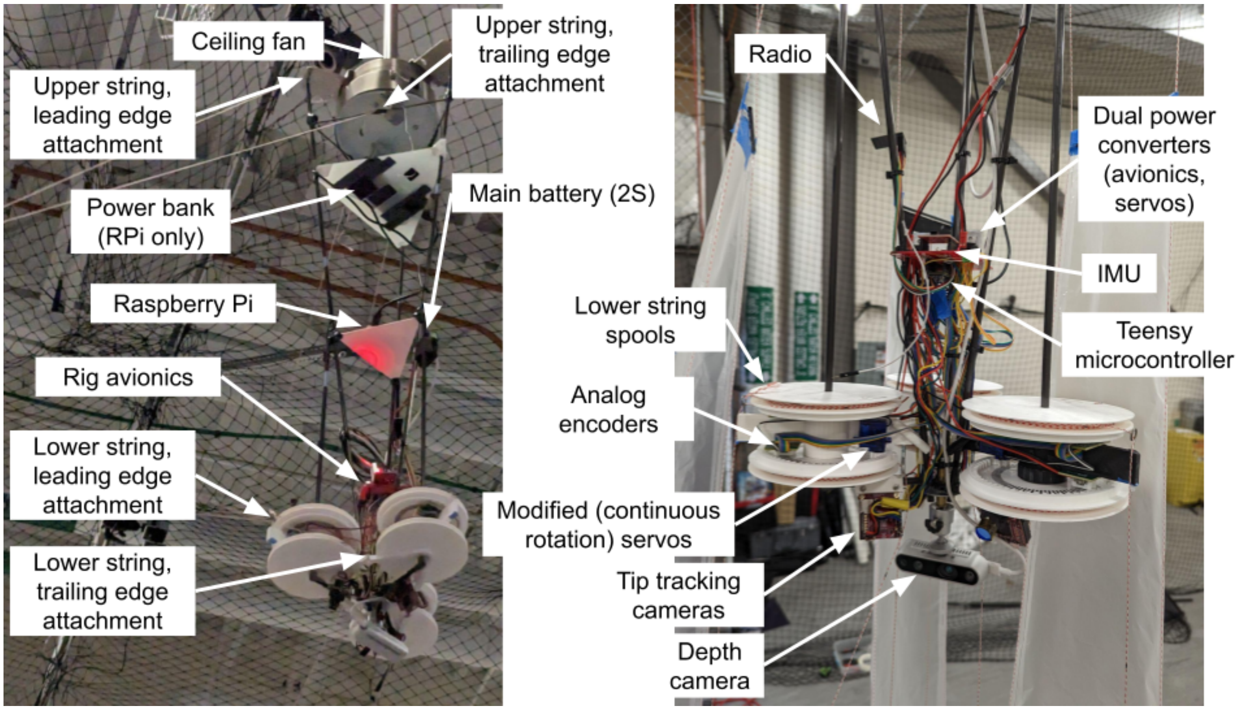

Figure A.1: Overview of the V5 test rig with major parts labeled.

The ground station and supporting equipment play a major role in the operation of the test rig. Speed control of the fan is accomplished using a VariAC transformer, shown in Fig. (A.2). While the test rig communicates via radio to a ground station computer (with the ground station under interface written using MATLAB), the radios need a SPI interface. A supporting Arduino Uno is used to provide this interface on the ground (with the Teensy on board the test rig being used directly for the flight radio). This is also shown in Fig. A.2.

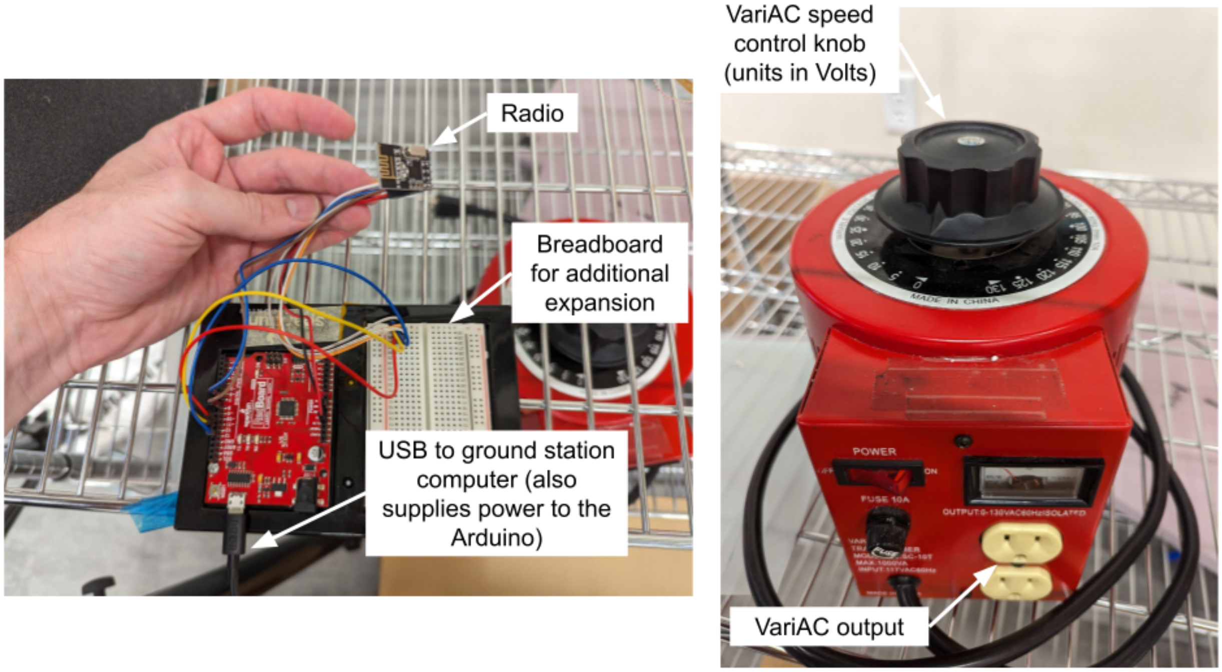

Figure A.2: Ground station Arduino with radio and VariAC used to control the rotation speed of the fan.

The ground station interface is written as a MATLAB App, and the major parts are described in Fig. (A.3).

To connect to the test rig, first ensure the power converters on the rig have been turned on and that the ground station Arduino is plugged in. Select the correct COMM port from the MATLAB App. If the proper port is not present, select Refresh and click 'Connect' to refresh available ports. The default (19200) baud rate should not need to be configured unless you have modified the ground station Arduino code.

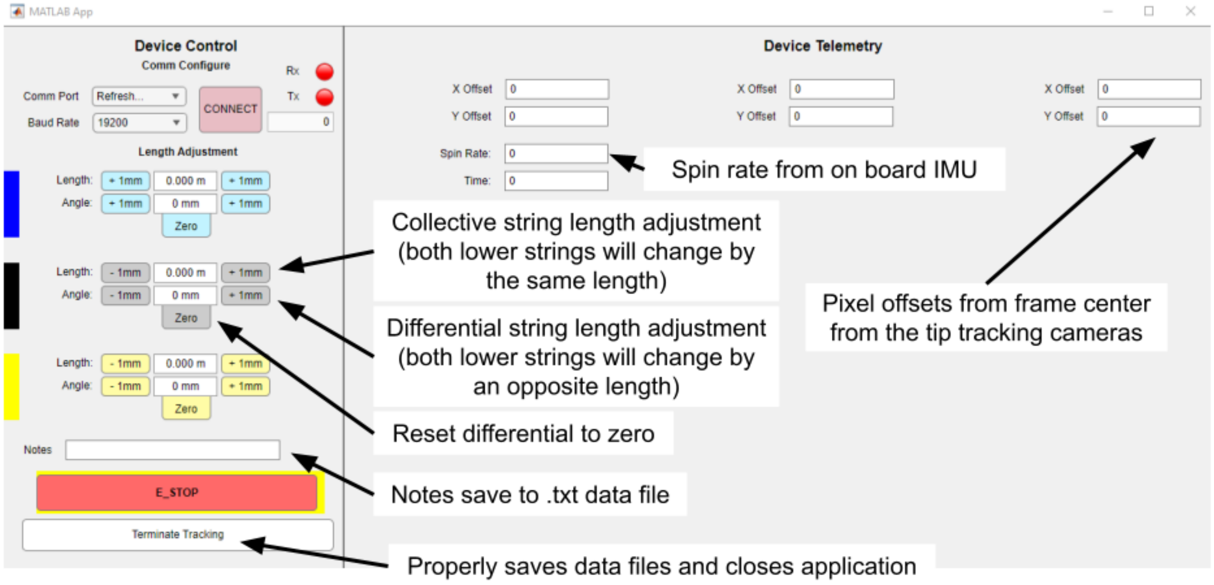

Spin rate from on board IMU

Collective string length adjustment (both lower strings will change by the same length)

Differential string length adjustment (both lower strings will change by an opposite length)

Reset differential to zero

Notes save to .txt data file

Properly saves data files and closes application

Pixel offsets from frame center from the tip tracking cameras

Figure A.3: MATLAB App which serves as the ground station interface.

Data should begin streaming, and the TX/RX lamps should flicker to indicate packets are being sent and received. Every 3 ms, the ground station will send length commands for each blade, sequencing through all blades (all blades will have received updated commands after 3 loops, 9 ms). Sending commands one blade at a time in this manner keeps communications short and allows the test rig to only need to receive and parse short packets. Every 250 ms, a data packet is received and parsed by the ground station, and written to a raw .bin file and a .txt file for further processing. Whatever content is in the "Notes" field is also written to the .txt file, making this a useful place to add test notes as commands are sent or new behavior is observed. Such notes will be linked in time to the test, providing additional context for future analysis.

The depth camera is currently operated independently of the MATLAB ground station interface, though future work could look to integrate the depth camera into the Teensy architecture and with the MATLAB GUI (there is C and MATLAB support in the RealSense SDK). In order to capture a depth recording, the user must SSH into the Raspberry Pi, navigate to the RealSense examples folders, and execute the rs-record example. This will save a recording as a ROS .bag file, which can then be transferred from the Raspberry Pi for processing.

By default, the recorder example is located in *˜/librealsense/tools/recorder.* To begin a recording, type *rs-record -f <directory and filename> -t <duration to record>* and press Enter. For example, to record a 10 second period called "10sRecord" to the current directory, you would execute *rs-record -f ./10sRecord.bag -t 10.* Note that ROS .bag recordings are quite large, with a 10 second recording taking approximately 500 MB. Additionally, the first ˜0.5 seconds of the recording is used for auto exposure and focus, and is therefore mostly unusable. During the testing conducted in this research, 5 second recordings were used.

The depth capture system, which includes the Intel RealSense 435i camera, the Raspberry Pi 4, and the external power bank to power the RPi, were borrowed for use in this research and have since been returned. To get full functionality with depth recording, those items will need to be reintegrated. If detailed depth measurements are not required for future testing, the tip tracking cameras can still be used.

Appendix B

Code Overview

Below is a top level description of all of the various codes developed throughout this research.

B.1 Standalone Scripts

B.1.1 bladeLiftTrends.m

Blade element theory model which outputs normalized lift distributions across the span of a blade as specified at the start of the script. Blade designs within 22% of a catenary distribution, the approximate blade geometry which was used for testing, and a sample full scale blade are provided and documented as comments.

B.1.2 muri_rotorSystemAnalysis_v2.m

The primary model for predicting the geometry of the 4-bar link system of strings when a blade section is producing lift and drag. Calculated string tensions with and without aerodynamic forces, and created a billowed blade section according to the specifications defined at the start of the script. Primarily used for performance predictions and analysis independent of test data, the output files unfortunately define many of the initial and test conditions for data processing and plotting.

B.1.3 rotorRequirements.m

In addition to modeling the form drag of the balloon, this script also implements an outdated version of the BET model that produces first order estimates of power and torque, but does not vary the blade's angle of attack to minimize these quantities. As such, the values reported from this analysis script with regard to torque and power are overestimates.

B.1.4 rotorTradeStudy.m

This script generated all of the scalability plots seen in Ch. 5. It takes a multitude of input parameters to define the balloon and rotor system, as well as environmental conditions via the *atmos* and *atmosMars* functions. The blade angle of attack is varied to only meet lift requirements.

Hardcoded baseline data plots are also included which plot values of coning angle, torque, power, and balloon spin rate across the full operational altitude range for the baseline design at three different ascent speeds.

B.2 V5 Test Rig

B.2.1 gossamerTestRig.ino

This is the C code to operate the test rig, which should be loaded onto the Teensy 4.1. Teensyduino was used in order to allow the use of the Arduino IDE with the Teensy microcontroller.

The program first defines a number of global variables as is standard in embedded programming and debug flags can be set to enable or disable serial print outputs. After configuring the various peripherals, the mainline loop roughly follows this flow:

(1) Check if a new command is available from the radio buffer, and if so, parse it and update the setpoint for the commanded servo motors

(2) Read onboard IMU data

(3) For each servo motor:

   (a) Sample the analog encoders to determine each motor's current rotation
   (b) If the error in servo position to setpoint is within than the software-defined deadband, disable the PID controller by setting the gains to zero.
   (c) Update PID controller and execute the motor command

(4) Get data from one of the tip tracking cameras (the "active camera" will cycle each loop, so each camera is sampled once every three loops)

(5) Send a telemetry packet to the ground station if at least 0.25 seconds has elapsed since the last transmission (restricts data downlink to 4 Hz).

The main loop runs with a constant loop time, currently defined to be 100 Hz.

B.2.2 cam_spiBlobDetect.py

This software should be flashed onto the openMV tip tracking cameras and implements a blob tracking algorithm in micropython (which runs on the camera hardware directly). The tracking thresholds are roughly tuned for the ASPEN Lab with optical filters attached.

The code extracts the blob location in pixels and passes it over SPI when requested to the gondola microcontroller (in prior testing, a Teensy 4.1).

B.2.3 UnoGroundStation.ino

This is the embedded software meant to run on an Arduino Uno which serves as an interface between the MATLAB ground station GUI and the telemetry radio. The main loop takes serial inputs from the MATLAB ground station and forwards the commands over the radio, and takes telemetry from the test rig via radio and forwards them to MATLAB over serial.

B.2.4 ControlGroundStation.mlapp

This MATLAB app serves as the ground station interface for the user during tests. Further operational details are provided in Appendix A, but functionally, the ground station opens a serial port for communication to the Arduino Uno ground station radio interface. It sends and receives serial commands and telemetry, writing data to a .bin and .txt file for post-processing.

B.2.5 muri_billowCatenaryFitter_v1.m

Script for processing point cloud data exported from Intel RealSense Viewer. Note that the ROS .bag file from the depth camera must first be read into RealSense Viewer to create a .ply file before running this MATLAB script. See directions in Fig. (B.1).

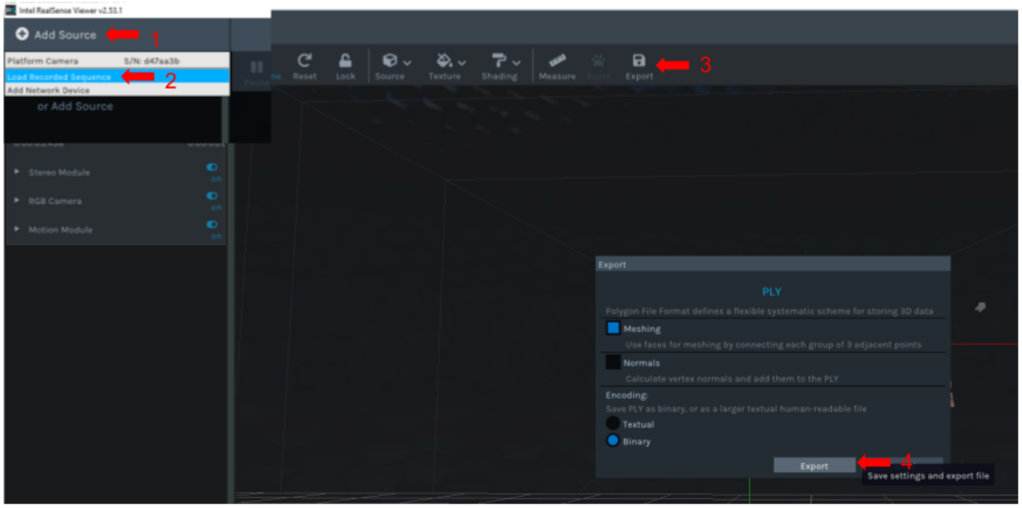

PLY

Polygon File Format defines a flexible systematic scheme for storing 3D data

☑ Meshing

Use faces for meshing by connecting each group of 3 adjacent points

☐ Normals

Calculate vertex normals and add them to the PLY

Encoding:

Save PLY as binary, or as a larger textual human-readable file

○ Textual

● Binary

Figure B.1: Procedure for loading a ROS .bag file into RealSense Viewer and exporting a .ply pointcloud for further MATLAB processing.

The script allows the user to select an analysis line along which to fit a catenary curve. The discrete pointcloud points are interpolated to the analysis line for curve fitting. These are then translated so that the start of the analysis line data begins at the origin, and rotated so that the depth data at the start of the analysis line is parallel to the x-axis.

Two catenaries are fit, one with a positive curvature and one with a negative (in order to be able to handle negative billowed blades, which were not studied in this research). The one with the best RMSE is selected and the other candidate is discarded.

The script generated the pointcloud and catenary line plots seen throughout the thesis and also saves a .mat file with the parameters of the best catenary fit.

B.2.6 muri_gossamerDataProcessing.m

This is the primary analysis script for gossamer blade test rig data. The user may be prompted to select 4 saved .mat files with processed data from other scripts (in order: the raw .txt file from the ground station, the catenary fit parameters from *muri_billowCatenaryFitter*, the predicted blade data from *muri_rotorSystemAnalysis*, and the camera tracking data from *muri_gossamerVideoProcessing*). Alternatively, the user can set the "Load Defaults" flag at the start of the script to load the default billowed test dataset (assuming the folder structure is the same as my local copy).

This script produces the majority of the results figures and data, including the coning and lag angles (from analysis of the tip tracking data), the lift and drag on the blade (from implementation of the force balance solutions described), and reconstructs the blade using the catenary fit data for visualization.

B.2.7 muri_gossamerVideoProcessing.m

Takes as an input a .mp4 video file of the RGB camera tracking footage and tracks the location of the tip marker LED using a rudimentary blob tracking algorithm. The red color channel is clamped to only include pixels with values greater than 250, and the mean location of the remaining pixels is saved. This procedure is conducted for each frame, and limited to just the top half of the image (since the depth camera is upside-down on the test rig, the upper half of the image contains the blade tip with the lower half only contributing noise sources).

B.2.8 importBladeData.m

Helper function for loading .txt telemetry files from the test rig.

B.3 General Helper-Functions

B.3.1 atmosMars.m

Provides temperature, pressure, atmospheric density, and kinematic viscosity of the martian atmosphere using data from NASA[1] .

B.3.2 plotRig.m

Takes rig geometry inputs and creates a base figure for plotting string and blades onto.

B.3.3 reorient.m

A function which implements a number of coordinate transformations needed for rotating the wing due to influences from drag.

B.3.4 tensionCalculator.m

Implements the force balance described in Ch. 4 for string tension without the influence of aerodynamic forces.

B.3.5 tensionCalculatorAero.m

Implements the force balance described in Ch. 4 for string tension with the added influence of aerodynamic forces.

---

[1] https://www.grc.nasa.gov/www/k-12/rocket/atmosmrm.html